

# **Microstructure of particles produced by fluidized bed agglomeration of soft materials**

**Dissertation**

zur Erlangung des akademischen Grades

**Doktoringenieur  
(Dr.-Ing.)**

von **M.Sc. Reihaneh Pashminehazar**

geb. am 06.08.1986 in Tabriz, Iran

genehmigt durch die Fakultät für Verfahrens- und Systemtechnik  
der Otto-von-Guericke-Universität Magdeburg

Promotionskommission:

Prof. Dr.-Ing. Eckehard Specht (Vorsitz)

Prof. Dr.-Ing. habil. Evangelos Tsotsas (Gutachter)

Prof. Dr.-Ing. habil. Stefan Heinrich (Gutachter)

Dr.-Ing. Michael Jacob (Gutachter)

eingereicht am:

11.12.2018

Promotionskolloquium am:

04.07.2019



# Declaration of Authorship

I hereby declare that I prepared the dissertation with the title:

“Microstructure of particles produced by fluidized bed agglomeration of soft materials”

without inadmissible assistance and without the use of any aids other than those indicated. Facts or ideas taken from other sources, either directly or indirectly, have been marked as such. In particular, I did not use the services of a commercial graduation consultation. Further I have not made payments to third parties either directly or indirectly for any work connected with the contents of the submitted dissertation.

The work has not so far been submitted either in Germany or abroad in same or similar form as a dissertation and has also not yet been published as a whole.

Magdeburg, November 30, 2018

M.Sc. Reihaneh Pashminehazar



## Acknowledgements

First and foremost I would like to express my sincere gratitude to my primary supervisor, Prof. Dr.-Ing. Evangelos Tsotsas, who gave me the opportunity to work at the Chair of Thermal Process Engineering. His guidance, useful critiques and challenging discussions have inspired me through the highs and lows of this thesis. It was my privilege to work at his chair and I benefited a lot from his vast knowledge.

I wish to deeply acknowledge my immediate supervisor, Dr.-Ing. Abdolreza Kharaghani, who leads the research team on pore network modeling and drying at the Chair of Thermal Process Engineering. I was his first PhD student whose project topic was not on the pore network modeling but his critical scientific knowledge paved the way for me to get into my project topic. My three high quality peer-reviewed journal publications would not have been possible without his tremendous feedback and revision. Also, his consultation and advice in my both academic and non-academic life was invaluable. Besides my advisor, I would like to thank the rest of my dissertation committee members, Prof. Dr.-Ing. habil. Stefan Heinrich and Dr. Michael Jacob for accepting to review this thesis.

This work would not have been possible without the financial support from the graduate school 'Micro-Macro-Interactions in Structured Media and Particle Systems'(GK1554), funded by the Deutsche Forschungsgemeinschaft (DFG). Moreover, I appreciate the scholarship provided by "Gender Equality Office" at OVGU for completing the writing of my thesis. I am also thankful to all my colleagues and fellow PhD students at the chair of Thermal Process Engineering for their help whenever I needed.

I would like to thank my parents, whose love, encouragement and best wishes are with me in whatever I pursue. Most importantly, I want to thank my mother for her tolerance during these years of being far from me. I owe thanks to a very special person, my husband, for his continued and unfailing love, support and understanding during my pursuit of PhD degree that made the completion of thesis possible. I greatly value his contribution and deeply appreciate his belief in me. Also I don't know how to thank my little princess Helma for her patience during mommy's PhD studies. Although her coming to my life stopped my research career for a while, she has made me a stronger and more motivated person in different aspects of my life.



## Abstract

Food powders such as maltodextrin are often produced in agglomerate form in spray fluidized beds in order to enhance their user properties. These agglomerates mostly have complex structures and are composed of amorphous and irregular primary particles. The internal structure and morphology of food agglomerates has rarely been investigated at the microscopic scale. In this work, a nondestructive X-ray micro-computed tomography technique is used as an appropriate experimental method to overcome this lack of data by a thorough characterization of the three-dimensional internal structure of maltodextrin agglomerates. A sequence of image processing steps is applied to the X-ray images in order to obtain 3D views and to extract data for the morphological characterization. The internal porosity as well as the size and spatial distribution of the pores inside the agglomerates are evaluated. Open pores formed during the agglomeration process are also determined from the X-ray images. The agglomerate shape is investigated and compared by 3D and 2D image analyses. Maltodextrin primary particles with non-spherical shape have a broad size distribution, and they may deform and overlap as they go above the glass transition temperature during the agglomeration process. A comprehensive methodology is developed based on the preflooded watershed segmentation of X-ray images to distinguish the primary particles in maltodextrin agglomerates. Thus center coordinates and volume of each particle are extracted.

The morphology of agglomerates has first been investigated by approximating the constituent primary particles with equivalent spheres. However, this simplified spherical primary particle model (SPPM) is questionable for agglomerates made of irregularly shaped primary particles. Therefore, the SPPM is compared with a model that is based on complete data of the real structure (real structure model, RSM). After a series of image processing steps over the 3D X-ray images, the data has been used to derive various 3D morphological descriptors (such as coordination number, coordination angle, radial distribution of primary particles and open porosity) by both the SPPM and the RSM. The results of the two models delineate noticeable differences, indicating that the SPPM may not provide a precise characterization of maltodextrin agglomerates. Therefore, the RSM is the more appropriate method to study the morphology of agglomerates that consist of soft and deformable primary particles of varying size and irregular shape.

The spatial morphology of this kind of soft agglomerate, here maltodextrin, can be quantified by fractal dimension. Previous research in this regard was focused on simulated agglomerates or 2D projected images of real agglomerates. Based on the information on each separated particle in 3D X-ray images, the radius of gyration is here calculated and compared for either monodisperse or polydisperse primary particles. The primary particles comprising the maltodextrin agglomerates follow a broad size distribution, hence considering the polydispersity is highly recommended. Next, radii of primary particles are determined in order to calculate 3D fractal dimension and prefactor from power law equation. Due to the irregular shape of primary particles, two different ways of calculating primary particle radius are investigated. It is observed that differences in primary particle radius affect the partial overlapping of particles which mostly influences the prefactor value, while only slight changes are noticed in the fractal dimension. Further, the gyration radius and fractal dimension are obtained directly from voxel data. Though this method is more accurate, it requires more effort and time. Therefore, by considering some error, the separated polydisperse primary particle model is suggested as a proper option. Finally, fractal dimension is also calculated by the box-counting method. The proper implementation of this method for 3D structures is discussed and the results are compared with the classical power law function.

Maltodextrin agglomerates have been produced at different process condition by changing the inlet air temperature and spraying rate. The developed structural and morphological characterizations are applied on these agglomerates. In this way, the correlation between process parameters and morphology of the agglomerates is finally investigated.



## Zusammenfassung

Lebensmittelpulver wie Maltodextrin werden oft in agglomerierter Form in Sprühwurbelschichten hergestellt, um ihre Gebrauchseigenschaften zu verbessern. Diese Agglomerate weisen meist komplexe Strukturen auf und bestehen aus amorphen und unregelmäßigen Primärpartikeln. Die innere Struktur und Morphologie von Lebensmittelagglomeraten wurde selten im mikroskopischen Maßstab untersucht. In dieser Arbeit wird eine zerstörungsfreie Röntgen-Mikro-Computertomographietechnik als geeignete experimentelle Methode eingesetzt, um diesen Datenmangel durch eine gründliche Charakterisierung der dreidimensionalen inneren Struktur von Maltodextrinagglomeraten zu überwinden. Auf die Röntgenbilder wird eine Reihe von Bildverarbeitungsschritten angewendet, um 3D-Ansichten zu erhalten und Daten für die morphologische Charakterisierung zu gewinnen. Die innere Porosität sowie die Größe und räumliche Verteilung der Poren innerhalb der Agglomerate werden bewertet. Aus den Röntgenbildern werden auch die während des Agglomerationsprozesses gebildeten offenen Poren bestimmt. Die Agglomeratform wird durch 3D- und 2D-Bildanalysen untersucht und verglichen. Primärpartikel aus Maltodextrin mit nicht-sphärischer Form haben eine breite Größenverteilung, und sie können sich verformen und überlappen, wenn sie während des Agglomerationsprozesses über die Glasübergangstemperatur hinausgehen. Basierend auf der vorflutenden Wasserscheidensegmentierung von Röntgenbildern zur Unterscheidung der Primärpartikel in Maltodextrinagglomeraten wird eine umfassende Methodik entwickelt. Dadurch werden die Mittenkoordinaten und das Volumen der einzelnen Partikel extrahiert.

Die Morphologie von Agglomeraten wurde zunächst untersucht, indem die konstituierenden Primärteilchen mit äquivalenten Kugeln approximiert wurden. Dieses vereinfachte sphärische Primärpartikelmodell (SPPM) ist jedoch für Agglomerate aus unregelmäßig geformten Primärpartikeln fraglich. Daher wird das SPPM mit einem Modell verglichen, das auf vollständigen Daten der realen Struktur basiert (Realstrukturmodell, RSM). Nach einer Reihe von Bildverarbeitungsschritten über die 3D-Röntgenbilder wurden aus den Daten verschiedene morphologische 3D-Deskriptoren (wie Koordinationszahl, Koordinationswinkel, radiale Verteilung der Primärteilchen und offene Porosität) sowohl vom SPPM als auch vom RSM abgeleitet. Die Ergebnisse der beiden Modelle zeigen deutliche Unterschiede auf, die darauf hindeuten, dass das SPPM möglicherweise keine genaue Charakterisierung von Maltodextrin-Agglomeraten liefert. Daher ist das RSM die geeignetere Methode, um die Morphologie von Agglomeraten zu untersuchen, die aus weichen und deformierbaren Primärpartikeln unterschiedlicher Größe und Form bestehen.

Die räumliche Morphologie dieser Art von weichem Agglomerat, hier Maltodextrin, kann durch die fraktale Dimension quantifiziert werden. Frühere Forschungen in diesem Zusammenhang konzentrierten sich auf simulierte Agglomerate oder 2D projizierte Bilder von realen Agglomeraten. Basierend auf den Informationen über jedes einzelne Partikel in 3D-Röntgenbildern wird hier der Trägheitsradius berechnet und verglichen, entweder für monodisperse oder polydisperse Primärpartikel. Die Primärpartikel, die die Maltodextrin-Agglomerate umfassen, folgen einer breiten Größenverteilung, so dass die Berücksichtigung der Polydispersität sehr empfehlenswert ist. Als nächstes werden die Radien der Primärteilchen bestimmt, um die 3D fraktale Dimension und den Vorfaktor aus der Potenzgleichung zu berechnen. Aufgrund der unregelmäßigen Form der Primärteilchen werden zwei verschiedene Methoden zur Berechnung des Primärteilchenradius untersucht. Es wird beobachtet, dass Unterschiede im Primärpartikelradius die partielle Überlappung von Partikeln beeinflussen, die meist den Vorfaktorwert beeinflusst, während in der fraktalen Dimension nur geringe Veränderungen festgestellt werden. Weiterhin werden der Kreisradius und die fraktale Dimension direkt aus den Voxeldaten gewonnen. Obwohl diese Methode genauer ist, erfordert sie mehr Aufwand und Zeit. Daher wird unter Berücksichtigung eines Fehlers das getrennte polydisperse Primärpartikelmodell als geeignete Option vorgeschlagen. Schließlich wird auch die fraktale Dimension nach dem Boxcounting-Verfahren berechnet. Die korrekte Implementierung dieser Methode für 3D-Strukturen wird diskutiert und die Ergebnisse mit der klassischen Potenzgesetz-Funktion verglichen.

Maltodextrin-Agglomerate wurden unter verschiedenen Prozessbedingungen hergestellt, indem die Einlasslufttemperatur und die Sprühdrate geändert wurden. Die entwickelten strukturellen und morphologischen Charakterisierungen werden auf diese Agglomerate angewendet. Auf diese Weise wird der Zusammenhang zwischen Prozessparametern und Morphologie der Agglomerate schließlich untersucht.

# Contents

<b>Acknowledgements</b>	<b>v</b>
<b>Abstract</b>	<b>vii</b>
<b>Zusammenfassung</b>	<b>ix</b>
<b>1 Introduction</b>	<b>1</b>
1.1 Agglomeration . . . . .	1
1.2 Spray fluidized bed agglomeration . . . . .	3
1.2.1 Key parameters of spray fluidized bed agglomeration . . . . .	5
1.2.2 Material properties in the agglomeration process . . . . .	7
Effect of increasing the temperature . . . . .	8
Effect of humidity . . . . .	8
1.3 Adhesion mechanisms between water soluble particles . . . . .	9
1.4 Problem and motivation . . . . .	11
1.5 Outline of contents . . . . .	13
<b>2 Materials and methods</b>	<b>15</b>
2.1 Maltodextrin . . . . .	15
2.2 Agglomerate production . . . . .	17
2.3 Computed tomography . . . . .	20
2.3.1 Physics of X-radiation . . . . .	21

2.3.2	Principle of X-ray computed tomography scanning . . . . .	23
2.3.3	Removing artifacts . . . . .	25
2.4	Image processing . . . . .	26
<b>3</b>	<b>Morphological and structural characterization of agglomerates</b>	<b>29</b>
3.1	Introduction . . . . .	29
3.2	Separation of primary particles in the agglomerate . . . . .	30
3.3	Moment of inertia and radius of gyration . . . . .	32
3.4	Porosity . . . . .	34
3.4.1	Porosity of closed pores (Internal porosity) . . . . .	35
3.4.2	Spatial and size distribution of internal pores . . . . .	37
3.4.3	Porosity of open pores . . . . .	37
	Porosity from the radius of gyration . . . . .	37
	Porosity by dilation . . . . .	38
	Porosity by convex hull . . . . .	39
3.4.4	Bulk porosity . . . . .	39
3.5	Circularity and sphericity . . . . .	40
3.6	Fractal dimension . . . . .	41
3.7	Results and discussion . . . . .	41
3.7.1	Primary particle separation and gyration radius . . . . .	41
3.7.2	Internal porosity (closed pores) . . . . .	44
3.7.3	Open pore porosity . . . . .	47
3.7.4	Bulk porosity . . . . .	49
3.7.5	Circularity and sphericity . . . . .	50
3.7.6	Fractal dimension . . . . .	53
3.8	Influence of $\mu$ -CT parameters on structural characterization . . . . .	54

3.9	General discussion . . . . .	57
<b>4</b>	<b>Spatial morphology of agglomerates: Real structure evaluation vs. spherical primary particle model</b>	<b>61</b>
4.1	Introduction . . . . .	61
4.2	Study models . . . . .	62
4.2.1	Real structure model (RSM) . . . . .	63
4.2.2	Spherical primary particle model (SPPM) . . . . .	63
4.3	Methodology and evaluation of 3D morphological descriptors . . . . .	63
4.3.1	Coordination number . . . . .	63
	Coordination number for SPPM . . . . .	64
	Coordination number for RSM . . . . .	64
4.3.2	Coordination angle for SPPM and RSM . . . . .	66
4.3.3	Radial distribution of primary particles . . . . .	67
	Cumulative radial distribution of particles . . . . .	67
	Particle density function . . . . .	68
4.3.4	Open pore porosity for SPPM and RSM . . . . .	69
	Porosity by convex hull . . . . .	69
	Porosity by radius of gyration . . . . .	70
4.4	Results and discussion . . . . .	71
4.4.1	Coordination number of primary particles . . . . .	71
4.4.2	Distribution of coordination angle . . . . .	75
4.4.3	Radial distribution of primary particle centers . . . . .	77
	Cumulative radial distribution of primary particles . . . . .	77
	Particle density function . . . . .	79
4.4.4	Porosity of open pores . . . . .	79

<b>5</b>	<b>Fractal dimension and prefactor of agglomerates with irregular structure</b>	<b>83</b>
5.1	Introduction . . . . .	83
5.2	Radius of gyration . . . . .	85
5.2.1	Radius of gyration based on separated primary particles . . . . .	85
5.2.2	Radius of gyration based on voxel information . . . . .	86
5.3	Fractal dimension . . . . .	86
5.3.1	Scaling law (Power law equation) . . . . .	87
5.3.2	Box-counting method . . . . .	88
5.4	Results and discussion . . . . .	89
5.4.1	Radius of gyration . . . . .	89
5.4.2	Fractal dimension (Scaling law) . . . . .	91
5.4.3	Fractal dimension (Box-counting) . . . . .	95
<b>6</b>	<b>Influence of process parameters on morphological characterization</b>	<b>97</b>
6.1	Introduction . . . . .	97
6.2	Influence of spraying rate . . . . .	98
6.2.1	Size distribution analysis . . . . .	99
6.2.2	Porosity . . . . .	101
6.2.3	Circularity and sphericity . . . . .	103
6.2.4	Fractal dimension . . . . .	103
6.3	Influence of process temperature . . . . .	105
6.3.1	Size distribution analysis . . . . .	105
6.3.2	Porosity . . . . .	107
6.3.3	Sphericity . . . . .	107
6.3.4	Fractal dimension . . . . .	109

<b>7 Conclusion and outlook</b>	<b>111</b>
7.1 Conclusion . . . . .	111
7.2 Outlook . . . . .	114
<b>Bibliography</b>	<b>115</b>
<b>A Evaluated morphological descriptors</b>	<b>123</b>
<b>Scientific contributions</b>	<b>133</b>
Journal publications . . . . .	133
Conference proceedings . . . . .	134
Conference presentations . . . . .	134
<b>Curriculum Vitae</b>	<b>136</b>





# Nomenclature

## Roman symbols

$A$	area	[m <sup>2</sup> ]
$a_w$	water activity	[-]
$C$	circularity	[-]
$D_{50}$	median diameter	
$D_f$	fractal dimension	[-]
$D_{FeMin}$	minimum Feret diameter of agglomerate	[m]
$d_A$	equivalent projected area diameter of primary particle	[m]
$d_{FeMin}$	minimum Feret diameter of primary particle	[m]
$d_V$	equivalent volume diameter of primary particle	[m]
$I$	moment of inertia	[kg m <sup>2</sup> ]
$I_0$	incident radiation intensity	[W m <sup>-2</sup> ]
$K_f$	fractal prefactor	[-]
$M$	total mass of agglomerate	[kg]
$M_W$	molecular weight	[kg mol <sup>-1</sup> ]
$m$	mass	[kg]
$N$	number	[-]
$P$	perimeter	[m]
$R$	radius	[m]
$R_e$	equivalent radius	[m]
$r$	position vector	[m]
$S$	surface area	[m <sup>2</sup> ]

$S_d$	standard deviation	[-]
$S_k$	skewness	[-]
$T_g$	glass transition temperature	[K]
$T_{g\infty}$	maximum glass transition temperature	[K]
$V$	volume	[m <sup>3</sup> ]
$x$	distance to center of mass	[m]
$Z$	atomic number	[-]

### Greek symbols

$\varepsilon$	porosity	[-]
$\epsilon$	box size	[m]
$\theta$	angle	[°]
$\mu$	linear attenuation coefficient	[m <sup>-1</sup> ]
$\rho$	density	[kg m <sup>-3</sup> ]
$\Phi_S$	sphericity	[-]

### Subscripts and superscripts

$agg$	agglomerate
$b$	bulk
$cp$	closed pores
$G$	center of gravity
$i$	primary particle or structural element index
$j$	primary particle or structural element neighbor index
$op$	open pores
$P$	primary particle
$s$	compact solid phase in agglomerate
$s, cp$	solid phase including internal pores in agglomerate

### Abbreviations

$\mu$ -CT	micro-computed tomography
-----------	---------------------------

<i>BCCA</i>	ballistic cluster–cluster agglomeration
<i>BPCA</i>	ballistic particle-cluster agglomeration
<i>CN</i>	coordination number
<i>CRD</i>	cumulative radial distribution
<i>DE</i>	dextrose equivalent
<i>DLCCA</i>	diffusion-limited cluster–cluster agglomeration
<i>DLPCA</i>	diffusion-limited particle-cluster agglomeration
<i>MCN</i>	mean coordination number
<i>PDF</i>	particle density function
<i>PMMA</i>	polymethyl methacrylate
<i>RSM</i>	real structure model
<i>SE – Ball3</i>	structuring element; shape: approximate ball, size: 3
<i>SE – Ball5</i>	structuring element; shape: approximate ball, size: 5
<i>SE – Cube3</i>	structuring element; shape: cube, size: 3
<i>SE – Cube5</i>	structuring element; shape: cube, size: 5
<i>SEM</i>	scanning electron microscope
<i>SPPM</i>	spherical primary particle model
<i>TEM</i>	transmission electron microscope



# Chapter 1

## Introduction

### 1.1 Agglomeration

Agglomeration is a natural phenomenon in which solid particles stick to each other. For powders and bulk solids, agglomeration can be unwanted, resulting in uncontrolled particle buildup, caking, bridging, or lumping. But it is also an important particle-size enlargement process widely used in various industries to improve the characteristics of a material; giving benefits to the end user in the form of improved quality and function of the final product .

For instance, fine powders are produced in agglomerated form in order to enhance their flowability, avoid lumping during rehydration, encapsulate sensitive components or simply to improve the optical appearance of the product [Palzer, 2011]. Agglomeration can be defined as the process in which primary particles are fixed together to form larger, porous secondary particles. The features of original particles are still distinguished in the structure -often with completely unaltered shape and size- and are held together by binding mechanisms. The binding mechanisms of agglomeration were first defined and classified by Rumpf [1990] and his co-workers. They are divided into five major groups:

- i. **Solid bridges:** Solid bridges may develop by diffusion of molecules from one particle to another through partial melting at points of contact where high pressures develop, especially at elevated temperatures. Solid bridges can also be built up by chemical reaction, crystallization of dissolved substance, hardening of binders, and solidification of melted component.
- ii. **Adhesion and cohesion forces:** These forces are caused by immobile liquid films which act like binder bridges. The availability of sufficient moisture to produce a thin, immobile adsorption layer can contribute to the bonding of fine particles by effectively decreasing the distance between particles and increasing the interparticle contact area. This mechanism accounts for the cohesion of slightly moist powders.

Thin, immobile layers may also be formed by highly viscous solutions of adhesives, and so the bond strength will be greater than that produced by mobile films.

- iii. **Surface tension and capillary pressure:** One of the most common binding mechanisms of wet agglomeration are liquid bridges at the coordination points between the particles forming the agglomerate. Liquid bridges can develop from free water or by capillary condensation. They are often the precondition for the formation of solid bridges.
- iv. **Attraction forces between solid particles:** These forces are often the cause for unwanted agglomeration. The most important binding mechanisms in this category are molecular, electric, and magnetic forces. At extremely small distances between neighbor particles, these forces can be very high, however they diminish quickly with increasing distance at the coordination points.
- v. **Interlocking bonds:** Normally, interlocking bonds occur if the particulate solids have the shape of fibers or weave which bend about each other or entangle during agglomeration. Although mechanical interlocking of particles influences agglomerate strength, its contribution is generally considered to be small in comparison with other mechanisms.

This classification of bonding mechanisms has become widely accepted in literature [Parikh, 2005]. It should be noted that in practice usually more than one bonding mechanisms are acting simultaneously in any particular system.

Considering the nature of materials and end-product applications, many techniques are available for agglomeration [Bück and Tsotsas, 2016]. The most common types of agglomeration can be broken down into three general categories: agglomeration by agitation (sometimes referred to as wet agglomeration or tumble/growth agglomeration; pressure (compaction) agglomeration, and agglomeration using heat (sintering).

In tumble/growth agglomeration, as the name implies, primary particles adhere to each other after colliding during their irregular, stochastic motion in a particle bed and form a new entity that is held together by binding forces. The adhesion of particles to one another is controlled by the competition between volume-related separation and surface-related adhesion forces. To cause permanent adhesion, the sum of all separation forces in the system (e.g., gravity, inertia, drag, etc.) must be smaller than the attraction forces between the adhering partners. If solids are in the micron, submicron, or nano range (starting at approximately  $10\ \mu\text{m}$ ), adhesion occurs naturally even when the primary particles are dry. In the case of larger particles, adhesion forces must be generated by adding binding agent (mostly water or other liquids). Moreover, the probability of particle collisions must be increased by providing a high concentration of particulate solids. Such conditions are obtained in

inclined disks (pans), rotating drums, powder mixers, and fluidized beds or during spray drying or chilling [Pietsch, 2002].

In pressure agglomeration, enlarged entities are formed by applying external forces to essentially dry particulate solids in more or less closed dies that define the shape of the agglomerated product. By increasing the force pressing the particles together, it is possible to agglomerate powders without addition of binder and significant plasticization of particles [Palzer, 2011]. Since the level of force applied is the most distinguishing factor, there are low, medium, and high pressure techniques. Extrusion, tableting and roller compaction are examples for such pressure agglomeration processes applied in the food industry. In extrusion of wet powder masses, a low pressure is applied to form agglomerates. During roller compaction or tableting, the particles are subject to high pressure leading to dense and mechanically stable agglomerates [Palzer, 2007].

In agglomeration using heat (sintering), atoms and molecules begin to migrate across the interface where particles touch each other. This happens at a certain elevated temperature, which is different for various materials. While still in solid state, diffused matter forms a bridge similar to the structures between surfaces that solidify upon cooling.

## **1.2 Spray fluidized bed agglomeration**

Spray fluidized bed agglomeration is widely used by the chemical, food and pharmaceutical industry as a method to improve the instant properties and the followability of various powder products [Fries et al., 2014]. Food powders such as dairy powders, culinary powders for vending machines, fine chemicals such as vitamin mixes, detergent powders and pharmaceutical excipients are agglomerated by fluidized bed process. The main aim of agglomerating the food powder is to enhance instant properties like dispersing and dissolution in liquids. Agglomeration of powdery chemicals can also help to control the particle size distribution and reduce potentially hazardous aspects of solids processing, such as dust during transportation and handling. Pharmaceutical powder blends are agglomerated in fluidized beds before tableting in order to improve dosing accuracy during tableting and to avoid demixing during transport processes.

The process of spray fluidized bed agglomeration comprises of spraying liquid (binder aqueous solution or water) on a bed of primary particles which are kept in fluidized state by hot air. Droplets of the sprayed liquid settle on the fluidizing particles and form adhesive surfaces because of the local wetting of the particle surface (water soluble particles) or the deposition of binder solution on the particle surface (non soluble particles) [Avilés-Avilés, Dumoulin, and Turchiuli, 2015]. Collision of wet particles leads to the formation of liquid bridges or viscous bridges between them and their coalescence. Drying of particles with

hot air converts these bridges to solid bridges. All these steps (fluidization, wetting, coalescence, drying) happen simultaneously in the same equipment. Agglomerates produced in spray fluidized bed may consist of primary particles bound together in a compact way or may have complex structures involving dendrites, depending on the properties of the primary particles and the way of creation. Homogeneous distribution of the spray liquid in the fluidized bed is a prerequisite for uniform growth, whereas local over-wetting leads to the formation of particle clusters. The moisture distribution in the apparatus is a key parameter affecting both particle size and structure of the product [Fries et al., 2011]. Fluidized bed granulators or agglomerators can be categorized in five different configurations, which are schematically shown in Fig. 1.1:

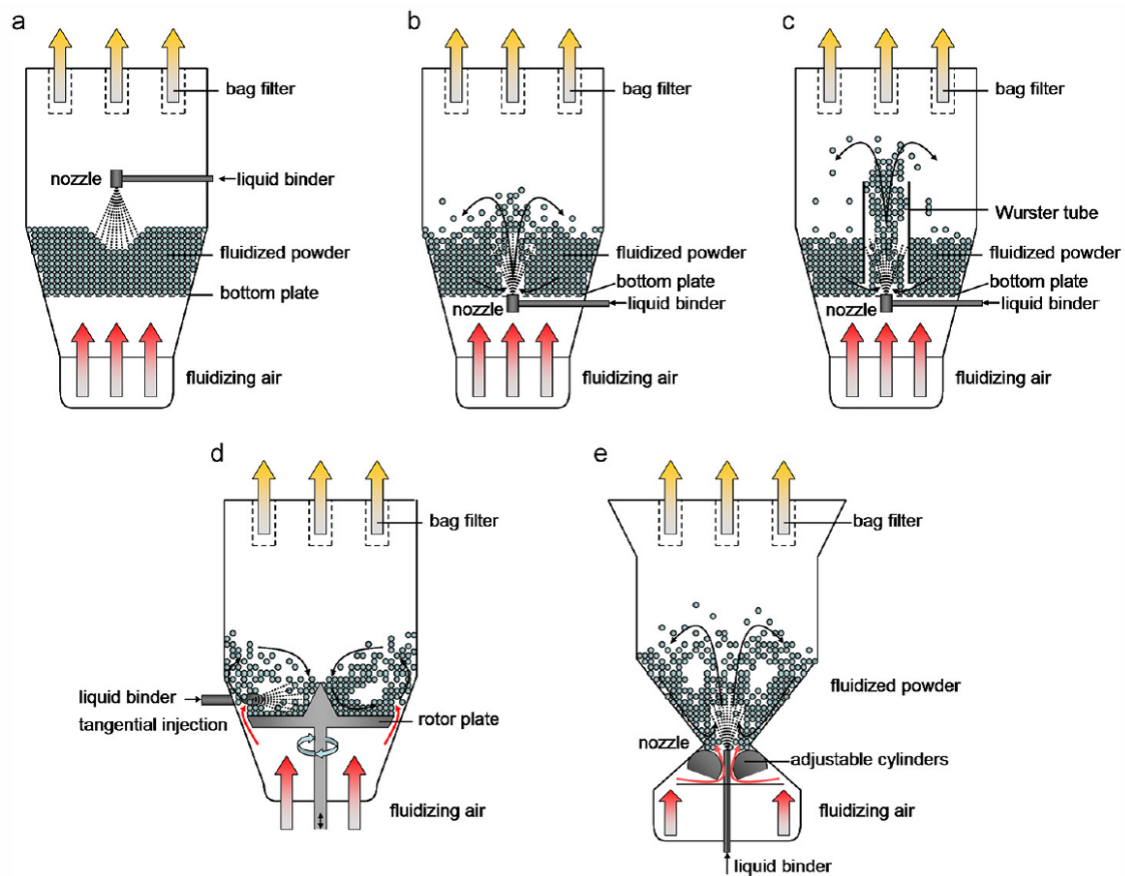


**Figure 1.1:** Schemes of different fluidized bed spray granulator configurations: (a)top spray granulator, (b)bottom spray granulator, (c)Wurster-coater, (d)rotor granulator and (e)spouted bed granulator [Fries et al., 2011].

#### a. Top spray fluidized bed

In this conventional technique, the nozzle is installed at the top and above the moving particles, spraying liquid in downward direction. Fluidizing air flows through a porous plate from the bottom of the chamber. This type of granulator is generally employed in the food industry for size enlargement of various powders and food ingredients.



b. Bottom spray fluidized bed

In a bottom spray fluidized bed the nozzle is situated at the bottom and in the center of the chamber, inside the bulk powder. In this method the direction of the spray is upwards. This arrangement is common in dairy powder agglomeration processes.

c. Wurster-coater fluidized bed

It is a bottom spray granulator which is equipped with a draft tube (Wurster) to impose a circulating flow during fluidization. It is used in the pharmaceutical industry for coating tablets and smaller particles in the range of 20–1000  $\mu\text{m}$ .

d. Rotating fluidized bed

This technique uses a rotor installed at the bottom of the bed, whereas fluidizing air enters through an opening gap between the rotor and the wall. Binder is sprayed with a tangential nozzle injector on the fluidizing particles.

e. Spouted bed

The air for fluidization is introduced in the conical bottom of such equipment without distributor, but sometimes with adjustable cylinders. The particles are entrained by a spout in the center of the chamber. Liquid is sprayed by nozzles mounted in the bottom. Such equipment is frequently used for the production of detergent, pharmaceutical, food and fertilizer granules or agglomerates [Fries et al., 2011; Fries et al., 2013].

### 1.2.1 Key parameters of spray fluidized bed agglomeration

Fluidized bed agglomeration is a complicated process where several parameters have impact on the growth, structure and properties of the agglomerates. Some are linked to the product (composition, size, size distribution) while others are related to the equipment geometry and the operation conditions like the spraying rate, droplet size, air temperature and humidity of the fluidizing gas and the primary particle load [Barkouti et al., 2013]. For instance, an excess amount of binder or a low fluidization temperature can lead to the collapse of the fluidized bed and the formation of big clumps of agglomerates. This collapse phenomenon also occurs when fluidization is not homogeneous. On the other hand, a small quantity of binder or high temperature of blowing air can cause insufficient agglomeration. Moreover, although the higher rate of fluidization can prevent bed collapsing, it may cause the breakage and rupture of produced agglomerates. Therefore, the desired product properties cannot be achieved by optimizing individual variables separately and it is necessary to control the agglomeration process to avoid such problems. It is well known that fluidized bed granulation is a complex and a multidimensional process [Ziyani and Fatah, 2014; Avilés-Avilés, Dumoulin, and Turchiuli, 2015]. Table 1.1 shows different parameters that can have influence on the agglomerates produced by spray fluidized bed granulator.

**Table 1.1:** Main parameters of fluidized bed agglomeration (adopted from Avilés-Avilés, Dumoulin, and Turchiuli [2015])

Geometry of the equipment	Chamber	Size
		Shape
	Nozzle	Type
		Position
Operating parameters	Particle load (holdup)	
	Fluidizing air	Flow rate
		Temperature
	Spraying	Feed rate
		Drop size
	Material parameters	Particles
Size, size distribution, density		
Surface properties		
Sprayed liquid		Composition/Concentration
		Temperature

However, the complexity of the hydrodynamics of fluidized bed combined with the phenomena of agglomeration, breakage and drying kinetics makes the process relatively difficult to describe. The mathematical description of a system of particles during agglomeration is traditionally done by population balances. With population balance equation (PBE) it is possible to track the evolution of particle size distribution in agglomeration process. Analytical solution of PBE is possible only for extremely simplified cases; generally solutions have to be obtained numerically. Consequently, many numerical methods have been proposed in the literature for the solution of the PBE [Kumar et al., 2008]. Solving the population balance equation is a complicated task due to the integro-differential nature of the equations which require discretization in both, space and time; this task becomes more difficult for multivariate systems.

Furthermore, one of the most challenging issues for using population balance equation is to model the kinetics of the process. For an agglomeration process the kinetics are usually described by aggregation kernels. Usually, these rate laws are unknown so that the inverse method must be applied to extract values and solve the classical PBE. Experimental data can be used as an input but it is limited only for the certain apparatus under specific process conditions. For estimating the agglomeration kinetics most of the researches focus on fitting the parameters rather than modeling because it is difficult to consider the effect of process parameters and material properties in such kernels. For the first time Hussain et al. [2013] and Hussain, Kumar, and Tsotsas [2015] modeled the effect of process conditions and material properties in the aggregation kernel with the aim of predicting the particle size distribution by means of the population balance equation approach on a large scale without the necessity of extensive fitting of the kernel. In their model, the effects of micro-processes

such as particle collision, droplet deposition and droplet drying are incorporated in the aggregation kernel by taking into account the probabilities of wet collision and adhesion.

The difficulties of solving complicated multivariate PBE can be solved by stochastic algorithms, namely the Monte Carlo (MC) method. Monte Carlo method seems to be highly appropriate due to the discrete nature of the process. Instead of considering agglomeration to be continuous, macroscopic, and deterministic, the process is considered as a sequence of random events. Terrazas-Velarde, Peglow, and Tsotsas [2009] and Terrazas-Velarde, Peglow, and Tsotsas [2011a] used the MC method to model the agglomerate formation in fluidized bed. Their model overcomes the problems of discretization, does not require the application of the inverse method and can be compared directly to experimental data. The single micro-level interactions among the main entities within the fluidized bed, namely primary particles and droplets, which generate discrete events, were considered in their model. This simplifies the programming effort compared to deterministic methods and allows the inclusion of multiple mechanisms (agglomeration, breakage, drying, etc.) in a straightforward manner. Their modelling was only valid for spherical and rigid primary particles which agglomerated by spraying binder in spray fluidized beds. The effect of primary particle porosity during the formation of agglomerates was also studied by Terrazas-Velarde, Peglow, and Tsotsas [2011b]. Furthermore, Dervede, Peglow, and Tsotsas [2011] and Dervede, Peglow, and Tsotsas [2012] upgraded this approach and developed direct simulation via Monte Carlo, focusing on particle structure and the extension of internal coordinates. They introduced a novel 3-dimensional structure algorithm that takes into account the unrestricted spatial development of agglomerates. Moreover, Rieck et al. [2018] used Monte Carlo method for modelling the binderless agglomeration in which, due to the amorphous structure of the primary particles, the agglomeration occurs only by spraying water.

### **1.2.2 Material properties in the agglomeration process**

The behavior of the agglomeration process highly depends on the polarity and supra-molecular structure of the primary particles building agglomerates. The polarity of the substance determines the interaction of the material with solvents and plasticisers. Most carbohydrates, organic and inorganic acids and their salts, and various mineral salts are polar substances that can interact with polar liquids such as water and dissolve in aqueous solutions. In contrast, apolar molecules cannot dissolve with water and only they interact primarily with apolar liquids.

Polar water-soluble solids can have different supra-molecular structure. Supra-molecular structure also has noticeable influence on characteristic properties of solids. The solid material can be distinguished based on the two basic supra-molecular structures: Crystalline solids have regular ordered arrays of components held together by uniform

intermolecular forces, whereas in the amorphous system the molecules are randomly distributed and not arranged in regular arrays. Because of the different molecular mobility in these structures, water-soluble solids react differently when they are exposed to increasing humidity, temperature or stress.

### Effect of increasing the temperature

The free volume available for the motion of the molecules within crystalline or amorphous structures can be expressed as a molecular mobility. The molecular mobility and the free volume within amorphous and crystalline structures increases differently with increasing temperature. During the heating of a crystalline system, the molecules are vibrating around their position in the lattice, and at a specific temperature which is called melting point, the crystalline structure breaks down. In contrast, for amorphous systems no melting point exists. While heating an amorphous solid the free volume increases steadily. However, above a certain temperature the gradient with which the free volume increases changes significantly. Molecule clusters are set free and start to rotate and slip over each other. The lower border (onset) or the mean (midset) of this temperature interval is defined as glass transition temperature  $T_g$  [Palzer, 2010]. Fig. 1.2 illustrates schematically these changes for crystalline and amorphous structure.

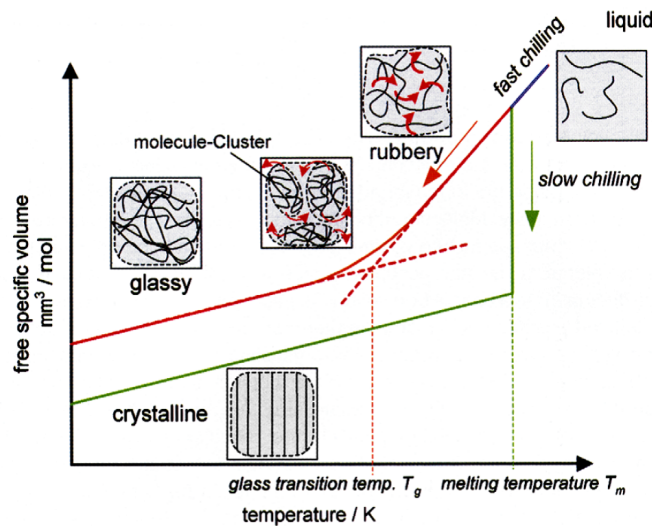


**Figure 1.2:** Free specific volume in crystalline and amorphous structures depending on changes in temperature [Palzer, 2010].

### Effect of humidity

Due to a larger free volume within the molecular matrix, the water uptake capacity of amorphous substances is larger than that of crystalline materials. Crystalline substances preserve their mechanical properties with increasing humidity until they dissolve at specific critical

relative humidity of the surrounding air. Amorphous water-soluble substances behave differently when they are exposed to an increasing relative humidity. They absorb increasing amounts of water with increasing relative humidity. In contrast to crystalline materials a critical humidity, at which particles might dissolve, cannot be defined. Absorption of certain liquids by amorphous solids often changes the mechanical properties of the particles. Such liquids, called plasticisers, have a similar polarity as the solid and thus can penetrate into the amorphous matrix. Water stored in the amorphous matrix has a plastifying effect on the amorphous structure. The viscosity and elasticity of the material decrease with increasing water content. In parallel, the glass transition temperature decreases due to absorption of water [Palzer, 2009; Palzer, 2010].

### 1.3 Adhesion mechanisms between water soluble particles

Increasing adhesion forces between particles are essential for agglomeration. Adhesion is strongly depending on the physico-chemical material properties discussed in the previous subsections. Most of the particles in food and pharmaceutical industries which are produced in agglomerated form are water soluble. Therefore, in this section specifically the agglomeration of this kind of particles with spraying water is discussed. The following adhesion mechanisms relevant for food agglomeration (water soluble particles) are classified by Dopfer et al. [2013]:

- a. Van der Waals forces increasing due to plastic or visco-elastic deformation of particles
- b. Capillary forces generated by liquid bridges between particles
- c. Viscous forces in visco-elastic sinter- or binder-bridges between particles
- d. Tensile strength of solid bridges generated by drying/solidification of binder

In a different fluidized bed agglomeration process, binder liquid is sprayed over the particle in order to generate liquid bridges between randomly colliding particles. The capillary forces are the main adhesion mechanism in this case. For the agglomeration of water insoluble or crystalline particles in which the liquid cannot migrate into the structure, the spraying of an aqueous solution containing a binder (e.g. amorphous component) is needed to improve the strength of the liquid bridges by forming a viscous thin film on the particle surface and making it sticky. A significant increase in adhesion forces can only be achieved by successful drying of liquid bridges to solid bridges.

When particles are soluble in water and contain amorphous components, it is usually sufficient to spray pure water as a binder. The glass transition temperature is specifically a

property of an amorphous material and plays an important role in the agglomeration process. At this temperature an amorphous system changes from a glassy to a rubbery state in a second order phase transition. As the temperature increases above  $T_g$ , many of the physical properties of the material suddenly change; among them, the most important are an increase in the free molecular volume, the heat capacity, the thermal expansion coefficient and dielectric coefficient and changes in viscoelastic properties [Bhandari and Howes, 1999].  $T_g$  is mainly a function of water content, molecular weight ( $M_W$ ) and the nature of dry matter compounds in a given substance. As water has a very low glass transition temperature, it is the major component responsible for depressing the  $T_g$  of food materials significantly. Thus, water is considered as a strong plasticiser in a food system. This decrease in the glass transition temperature can be described using the Gordon and Taylor [1952] equation,

$$T_g = \frac{(1-w)T_{g,dry} + wkT_{g,w}}{(1-w) + wk} \quad (1.1)$$

$T_{g,dry}$  is the glass transition temperature of the dry solid,  $T_{g,w}$  represents the glass transition temperature of pure water commonly considered equal to  $-135^\circ\text{C}$ .  $k$  is mostly used as a fitting parameter after  $T_g$  measurement. The  $k$  values of different materials can also be found in literature. Moreover, the  $T_g$  of polymers increases with increasing  $M_W$  up to a maximum value. Low molecular weight polymers (e.g. sucrose) and monomers (e.g. fructose, glucose) in their pure form have a low glass transition temperature whereas longer chain molecules have higher values. The Fox and Flory [1950] relationship is usually used in literature to determine the effect of molecular weight of a food polymer on  $T_g$  [Bhandari and Howes, 1999]:

$$T_g = T_{g\infty} - \frac{K_g}{M_W} \quad (1.2)$$

where  $T_{g\infty}$  is the maximum glass transition temperature that can be achieved at a theoretical infinite molecular weight and  $K_g$  is an empirical parameter which is related to the free volume present in the polymer sample.

Therefore, during the agglomeration of the amorphous material, the sprayed water can migrate into material matrix and can cause both some partial dissolution and plastification. Due to the absorbed water, the glass transition temperature of the amorphous substance strongly decreases. Furthermore the material viscosity decreases when the amorphous matrix undergoes glass transition. When the viscosity at the particle surface decreases locally below  $10^6$  Pa·s, the particle surface becomes sticky. If the collision of particles takes place in this step, the establishment of a material bridge is governed by the viscosity. But if two particles collide rapidly after the liquid droplet has been placed on the solid surface of one

of the two particles, a liquid bridge is formed. Due to the low viscosity of the liquid in this stage, the liquid bridges are stabilized by capillary forces. With dissolving the amorphous substance in liquid bridges, the viscosity increases and thus the strength of the bridge increases. Therefore, liquid bridge is transformed into a stable viscous bridge. In addition, amorphous water-soluble materials can easily deform visco-elastically which leads to increasing van der Waals forces due to an increasing contact area between the particles and a decreasing distance between the particle surfaces [Palzer, 2009; Palzer, 2011]. For the first time, Rieck et al. [2018] have developed a model for the agglomeration of water-soluble particles and also validated their model by a series of experimental investigations. Their model was based on stochastic approach (Monte Carlo method) and took into account the deposition of droplets on the particle surface, droplet imbibition, glass transition, binary collisions between particles and drying of the droplets. Their experimental work included batch agglomeration experiments in a lab-scale fluidized bed with different maltodextrins and varying process conditions. The measured particle size distributions of the samples taken during the agglomeration experiments were compared to the simulation results.

## **1.4 Problem and motivation**

Macroscopic features of agglomerates are directly influenced by microscopic features like microstructure, size and shape. In order to enhance or control properties of agglomerate and be able to predict the structure of final products, it is essential to establish a link between the product properties and the operating conditions. In recent years, morphological study of agglomerate has gained significant importance to deeply understand the structural characteristics of agglomerates for the enhancement of end-use properties [Hafsa et al., 2014; Hafsa et al., 2015]. Our understanding of the physical phenomena that occur during spray fluidized bed agglomeration has been significantly enhanced by recently developed Monte Carlo simulations [Terrazas-Velarde, Peglow, and Tsotsas, 2009; Rieck et al., 2018] and population balance models [Hussain, Kumar, and Tsotsas, 2015]. Despite this progress, it still remains a challenge to characterize the structure of agglomerates (especially food agglomerates) produced in a spray fluidized bed. A successful characterization should allow a better understanding of process–structure or structure–property relationships. The quantification of the internal microstructure of agglomerates is also crucial for setting up processing maps and for describing agglomeration patterns and mechanisms.

Common analytical techniques applied to the study of agglomerate structure are mostly restricted to two-dimensions. For instance, the morphology of aerosols and flame aggregates is usually investigated by means of scanning electron microscopy (SEM), transition electron microscopy (TEM) and light scattering [Köylü, Xing, and Rosner, 1995; Ibaseta and Biscans, 2010; Lapuerta, Ballesteros, and Martos, 2006; Chakrabarty et al., 2008]. Hafsa et al. [2014] investigated and compared the external structure of agglomerated cereal powders

produced with different technologies by means of SEM scanning. The advantage of these techniques is that they provide rather inexpensive, rapid quantitative analysis and provide good overview about the external structure of the particles. The drawback is that the sample preparation for such techniques is often destructive and the techniques do not provide direct information in the third dimension. Also, no more information can be obtained about interior structure. Therefore, such 2D data may not fully represent the true 3D structures [Baker et al., 2012].

Some other researches on the morphology were conducted on simulated agglomerates, which lack measured experimental data and the involvement of physical properties of primary particles. Most of the simulated agglomerate studies refer to aerosol aggregates in which the morphology is characterized in the terms of fractal dimension [Brasil et al., 2001; Eggersdorfer and Pratsinis, 2012; Lapuerta, Expósito, and Martos, 2015]. The main problem with simulated agglomerates is the commonly assumed spherical shape of the primary particles, which is not applicable for most of the food powders with irregular structure.

X-ray micro-computed tomography ( $\mu$ -CT) has been proven to be a powerful tool for the analysis of the 3D structure of material. This is a nondestructive 3D imaging technique which uses a set of two-dimensional shadow X-ray images of an object to reconstruct its three-dimensional structure using a mathematical algorithm [Farber, Tardos, and Michaels, 2003]. This method can be used to overcome the problems of the traditional structural evaluation and simulation methods. X-ray ( $\mu$ -CT) does not provide the required resolution to scanning the structure of nanoparticle aggregates, but it is very well applicable to agglomerates and porous materials that consist of larger primary particles in order to get information about the internal structure and perform three dimensional quantitative analysis.

Despite its adequacy, the use of X-ray ( $\mu$ -CT) to investigate the internal microstructure of agglomerates produced by wet agglomeration has still been limited to few studies [Farber, Tardos, and Michaels, 2003; Rajniak et al., 2007; Dadkhah, Peglow, and Tsotsas, 2012] and more particularly for food applications. Most of the available studies were performed with non-soluble particles and only a few of them investigated the microstructure of particles undergoing glass transition [Hafsa et al., 2014; Hafsa et al., 2015]. The first systematic studies on various morphological descriptors for fluidized bed agglomerates were published by Dadkhah, Peglow, and Tsotsas [2012] by means of X-ray  $\mu$ -CT. The research was focused on hard, non-porous or porous, spherical primary particles such as glass beads and  $\gamma$ - $Al_2O_3$ , respectively. Such primary particles are insoluble in the binder, in contrast to food powders which are mostly amorphous materials that can absorb water and deform during agglomeration. The methodology and image processing sequences developed by Dadkhah, Peglow, and Tsotsas [2012] are merely effective for agglomerates made of primary particles which do not deviate too much from the spherical shape.



The purpose of the present work is thus to investigate the internal structure and morphology of agglomerates consisting of water soluble primary particles. Due to the complex structure of this kind of agglomerates, it not possible to analyze them with common 2D image analysis devices or only by simulation, unless with a huge loss of data and deviation from reality. Therefore, in this study a comprehensive 3D microstructural and morphological characterization is done by means of X-ray  $\mu$ -CT technique for maltodextrin agglomerates as representatives for many amorphous and water soluble agglomerates. This kind of characterization of agglomerates will be helpful in future for producing the desired end-user properties with low cost and less effort. Moreover, three dimensional data extracted from images can be used as input data and basis for microstructure design or any other research or simulation dealing with the structural evaluation of food agglomerates.

## 1.5 Outline of contents

The thesis is organized as follows:

In Chapter 1, after a general introduction in the agglomeration process and the most common types of it, spray fluidized bed agglomeration and key parameters in this method have been highlighted. Moreover, material properties and the effect of temperature and humidity during agglomeration have been discussed.

Chapter 2 details the experimental and evaluation procedure. First a short introduction about maltodextrin and its glass transition temperature is given. An overview of the experimental spray fluidized bed set-up and the specific process used to produce agglomerates is presented. Moreover, computed tomography method and physics of X-radiation are outlined. Subsequently, the principles of X-ray  $\mu$ -CT volume image acquisition, visualization and data extraction by image processing are discussed. Different trials for removing artifacts from the acquired volume images are also discussed.

Chapter 3 is dedicated to the description of the developed structural and morphological analysis based on the 3D data obtained by  $\mu$ -CT. In this regard, a comprehensive methodology for separating the primary particles of agglomerates in 3D images is described. Different methods of morphological characterization are developed and the required algorithms and image processing procedures for each of them are explained in details. At the end, the effect of  $\mu$ -CT scanning parameters on the structural characterization of maltodextrin agglomerates is discussed and optimal values for precise characterization in minimum possible time are defined.

Chapter 4 is mainly focused on the irregularity of the maltodextrin primary particles in agglomerates. Therefore, based on the data of the 3D volume image, the methodology for defining the real structure model (which considers the irregularity) and the simplified

spherical model are described in detail. After explaining the definition of various new 3D morphological descriptors, the concept and algorithms for implementing them for the two models are illustrated. Finally, by applying the descriptors for a series of agglomerates, the results obtained from two models are discussed and compared.

The motivation behind chapter 5 is to gain insights into the morphology of maltodextrin agglomerates by means of fractal dimension and prefactor based on different methodologies and assumptions. The scaling law method for calculating fractal dimension and prefactor is presented for monodisperse and polydisperse separated primary particles. In addition and for comparison, the same quantities are also illustrated for the real structure of the agglomerate from the voxel coordinates and voxel values in 3D X-ray images. At the end, the box counting method as another option for calculating fractal dimension is introduced and proper implementation of this method over 3D images is discussed.

Chapter 6 is about the investigation of the influence of process parameters on the morphology of agglomerates. Agglomerates produced at different process conditions are scanned by  $\mu$ -CT and, based on the obtained 3D data, some of the morphological descriptors mentioned in the previous chapters are obtained and discussed. The aim of this chapter is to demonstrate the effect of the process parameters on the structure of the agglomerates.

## Chapter 2

# Materials and methods

### 2.1 Maltodextrin

Maltodextrin is an additive utilized mainly in food and pharmaceutical industries. It serves as ingredient in confectionary, meat products, sauces, baby foods, dry soups and sports drinks. Maltodextrin has many functionalities including usage as a dispersing aid, flavor carrier, bulking agent, viscosifier or fat replacer, and it exhibits only a slightly sweet taste [Descamps et al., 2013].

Maltodextrin is basically a polysaccharide with molecular formula  $(C_6H_{10}O_5).nH_2O$ . It is mostly available as a white hygroscopic dry powder produced from the starch of corn, potato, rice etc. Maltodextrin is categorized by *DE* (dextrose equivalent) and ranges from 3 to 20. *DE* value is defined as measure of reducing power of starch polysaccharides compared with D-glucose. Starch can be hydrolyzed into simpler carbohydrates by acids, various enzymes, or a combination of the two. The extent of conversion is typically quantified by the dextrose equivalent (*DE*), which is roughly the fraction of the glycosidic bonds in starch that have been broken. It is the percentage of the total solids that have been converted to reducing sugars: the higher the *DE*, the more sugars and less dextrans are present [Kearsly and Dziedzic, 1995]. So, the *DE* value describes the degree of conversion of starch to dextrose (glucose) and can be categorized as following:

- Starch is close to 0
- Dextrans vary between 1 and 3
- Maltodextrans vary between 3 and 20
- Glucose syrups contain a minimum of 20 % reducing sugars, i.e.  $DE > 20$
- Glucose/dextrose has  $DE = 100$

In this work, agglomeration experiments were performed by maltodextrin particles with dextrose equivalent 12 (DE 12 Glucidex, supplied by Roquette, France). It was produced by controlled enzymatic hydrolysis, purification and spray-drying of a food maize starch. The main properties of this powder are listed in Table 2.1.

**Table 2.1:** Maltodextrin properties according to producer data sheet.

Maltodextrin DE 12	
DE	11-14
Bulk density	~400 g/l
Solubility in water	~600 g/l at 20 °C
$T_g$ dry powder	180 °C

Variations in *DE* value result in maltodextrins with varying physicochemical properties. Hygroscopicity, solubility, osmolality, and their effectiveness to reduce the freezing point rise with increasing *DE*; while viscosity, cohesiveness, glass transition temperature and coarse crystal prevention increase as *DE* declines. However, *DE* variation among maltodextrin polysaccharides does not necessarily mean that they differ only in dextrose content. Moreover, maltodextrins with the same *DE* value can have very different properties that reflect the composition of the components resulting from the hydrolysis reactions. The type of starch (corn, oats, rice, tapioca, potato, etc.) is also an important factor determining the molecular segments of maltodextrins. The ratio of linear amylose chain molecules to branched amylopectin varies according to the source of starch [Kearsly and Dziedzic, 1995; Chronakis, 1998].

One of the important properties of maltodextrin in agglomeration process is the glass transition temperature. The glass transition temperatures of principal sugars and other carbohydrate materials like maltodextrin with different *DE* used in food industry were summarized and presented by Bhandari and Howes [1999]. Based on their report glass transition temperature for starch is high (243 °C) whereas common sugars like fructose and glucose have very low glass transition temperature of 5 and 31 °C, respectively. The  $T_g$  value of 188 °C is reported for maltodextrin with *DE* 5 and this values decreases to 100 °C for maltodextrin with *DE* 36. The glass transition temperature for dry maltodextrin with the value of *DE* 12 is not available in their report but the  $T_g$  of 160 °C is mentioned for maltodextrin *DE* 10. Based on the data sheet provided by the producer, the  $T_g$  value of 180 °C mentioned for maltodextrin *DE* 12 is used in this study

Sorption isotherms and evolution of glass transition temperature with water activity ( $a_w$ ) and moisture content are given for two types of maltodextrin powders in Fig. 2.1. As shown in this figure,  $T_g$  decreases noticeably with increasing water content. Water plasticizes the amorphous matrix leading to an increase of molecular mobility and thus to a decrease of the glass transition temperature.

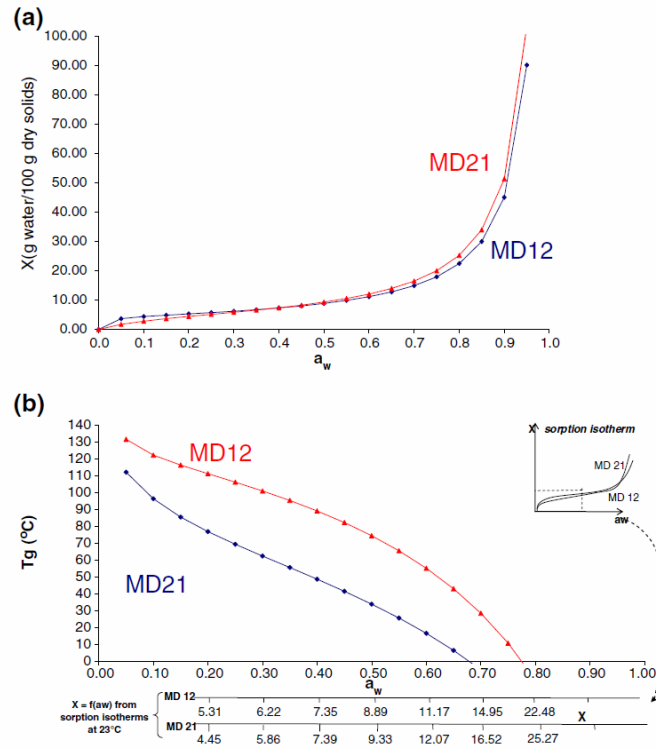


**Figure 2.1:** Sorption isotherms at 23°C (a) and evolution of glass transition temperature  $T_g$  as a function of water activity and water content (b) for maltodextrin DE12 and DE21 [Avilés-Avilés, Dumoulin, and Turchiuli, 2015].

## 2.2 Agglomerate production

As mentioned before, fluidized bed agglomeration is a complex process with many interdependent factors that influence end-product quality. All steps of fluidization, wetting of particles by spraying, coalescence and drying happen simultaneously in the same equipment. Therefore, controlling the process and producing the desired product are challenging issues. Most of the food, pharmaceutical and chemical agglomerated powders are water soluble. Maltodextrin may serve as a reference model substance for many amorphous water soluble food powders. Agglomeration of amorphous material like maltodextrin with low glass transition temperature can be fast due to the strong adhesion forces between moist amorphous particles. On the other hand, this can lead to a rather broad particle size distribution and the formation of a crust on the equipment surface and around the spraying nozzle [Palzer, 2011].

In this study, preliminary trials with different process parameters have been conducted before proceeding with the production of maltodextrin agglomerates (Fig. 2.2) for morphological analysis. In any case, in order to obtain a narrow size distribution of the primary particles used in the agglomeration process, maltodextrin powder was sieved in the range of 300 to 500  $\mu\text{m}$  (see Fig. 3.9). The agglomeration was performed in a lab-scale batch fluidized bed granulator (GPCG 1.1 LabSystem) with a transparent, cylindrical fluidization

chamber made of Plexiglas with 152 mm inner diameter and 450 mm height (Glatt GmbH, Germany). The experimental set up and its schematic diagram are illustrated in Fig. 2.3. For amorphous polar (water-soluble) powders, it is mostly sufficient to atomize water on the fluidized particles. Therefore, pure water was sprayed as a binder (plasticizing agent) with a two-fluid nozzle (model 940) provided by Düsen-Schlick GmbH (Untersiemau, Germany). The nozzle was placed on top of the chamber at a height of 150 mm from the distributor plate and operated with 0.5 bar relative air pressure. For each experiment, 50 g of powder were fluidized using a constant fluidization air flow rate of 70 kg/h, taken from the compressed air supply of the building and heated by an electrical heater before it enters into the chamber. The sinter metal air distributor with a pore size of 0.1 mm created uniform fluidization of the particle bed. The temperature sensor that controlled the air heater was located below the distributor plate. Equipment and the maltodextrin powder were pre-heated before spraying the water. With a piston pump, the water of ambient temperature was sprayed at a constant rate.



Figure 2.2: (a) Maltodextrin primary particles and (b) agglomerates produced in spray fluidized bed.

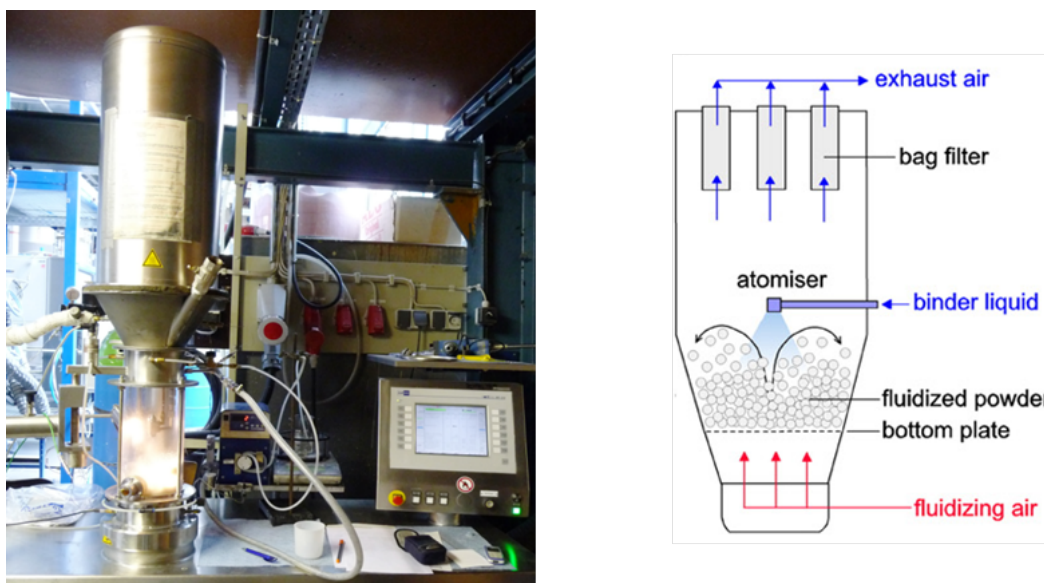


Figure 2.3: Experimental set up for lab-scale fluidized bed.

In order to study the influence of process parameters, different experiments were carried out, as summarized in Table 2.2. Most of the process conditions were kept constant in

all trials, only the values of inlet air temperature and spraying rate were varied. Trial D was the reference experiment, so that process parameter variations were conducted with respect to it. The first varied parameter was the spraying rate, set at 1.25, 1.75 and 2.25 g/min. At lower spraying rate than 1.25 g/min almost no agglomerates were produced, whereas the bed collapsed soon after the start of the experiment at spraying rates higher than 2.25 g/min. Secondly, the effect of inlet air temperature was studied in the range of 40 to 70°C. Outside of this range agglomerates were not produced properly. At higher temperature, due to the fast drying of droplets, agglomeration did not take place. Contrary, lower fluidization temperature resulted in the formation of big clumps of agglomerates and, finally, in collapsing of the bed due to the excessive amount of humidity inside the bed and the sticky nature of the maltodextrin powder.

The total agglomeration time was about 5 min and after that a sample was taken using a sampling tube which was located in the lower part of the bed. Particle size distribution and circularity of the primary particles and agglomerates were measured simultaneously by a Camsizer that uses the principle of dynamic digital image analysis (Camsizer P4, Retsch Technologies GmbH, Germany). For each measurement, the projected particle shadows were recorded at a rate of more than 60 images per second. In this way, every single particle of the sample was recorded and evaluated in a short time. With the used device, it is possible to measure for a wide range of particle sizes (30  $\mu\text{m}$ -30 mm) with a resolution capacity in the micrometer range.

**Table 2.2:** Process parameters for producing the maltodextrin agglomerates in spray fluidized bed.

Trial	Material load (g)	Air flow rate (kg/h)	Inlet air temperature (°C)	Spraying	
				Rate (g/min)	Mass (g)
A	50	70	40	1.25	6.2
B	50	70	50	1.25	6.3
C	50	70	45	1.75	8.6
D	50	70	50	1.75	8.5
E	50	70	55	1.75	8.7
F	50	70	50	2.25	11.2
G	50	70	70	2.25	11.2

The different bonding mechanisms between the maltodextrin agglomerates made of amorphous water soluble particles and glass bead agglomerates which are insoluble in water can be seen from scanning electron microscope (SEM) images (Phenom Pro G2, LOT-QuantumDesign GmbH, Germany). As shown in Fig. 2.4, water stored in the amorphous matrix has a plastifying effect on the maltodextrin structure. Also due to partial dissolution, collision of particles can lead to formation of sinter bridges. In contrast, the primary particles preserve their own structure in glass bead agglomerates; no overlapping and no

deformation of the particle surface can be observed. Water cannot migrate in the structure of glass beads and dissolution of particles also does not take place. Therefore, during the agglomeration of glass beads, a solution of binder must be sprayed on the fluidized bed. Due to capillary forces, collisions between these wetted particles create liquid bridges which turn into solidified binder by drying.

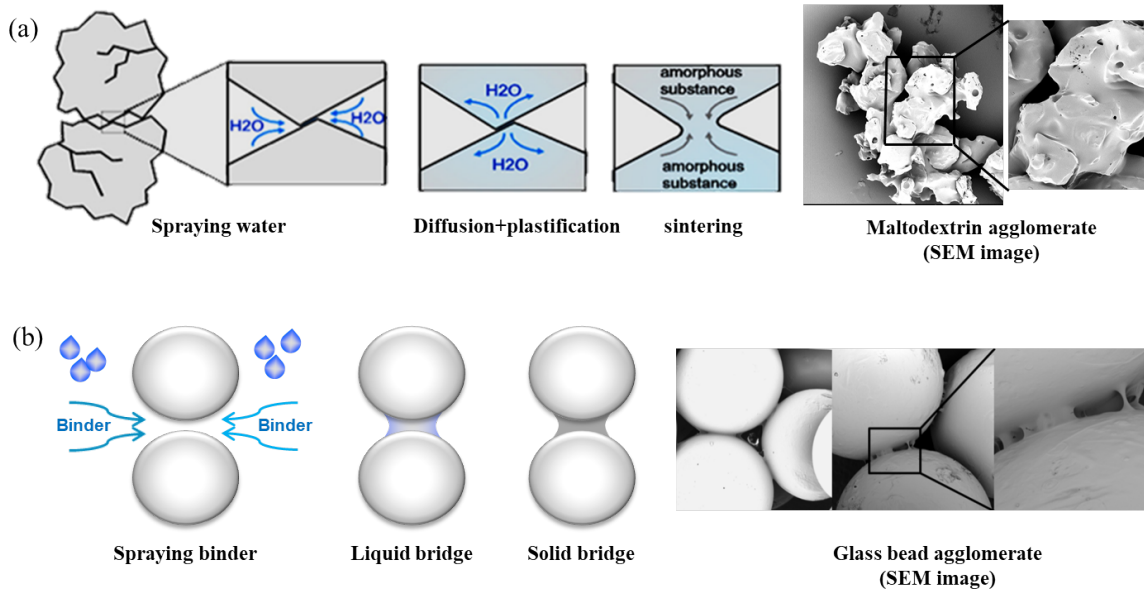


**Figure 2.4:** Bonding mechanisms and SEM images of agglomerates produced from (a) amorphous water soluble particles (Schematic view was illustrated by Dopfer et al. [2013]) and (b) water-insoluble particle (SEM image of the glass bead agglomerate was provided by Dadkhah [2014]).

### 2.3 Computed tomography

Computed tomography is a powerful tool for providing information about the 3D structure of materials or the human body. There is no doubt that 3D analysis is a valuable complementary method to all other techniques which provide only 2D information. The theoretical basis of Computed Tomography (CT) goes back to the year 1917, when the Austrian mathematician Johann Radon proved that an  $n$ -dimensional object can be reconstructed from its  $(n-1)$ -dimensional projections. However, it took nearly fifty further years for the mathematical basis of the actual CT image reconstruction to be presented by Cormack [1964]. The first CT scanner was invented in 1972 by Godfrey N. Hounsfield in England. It took several hours to acquire the raw data for a slice and days to reconstruct a single image from this raw data. It was installed in Atkinson Morley Hospital in Wimbledon, and the scanning of the first patient brain was done in 1972. By 1975 Hounsfield constructed the first full-body CT scanner. The invention was of such importance that Cormack and Hounsfield were awarded with the Nobel Prize in Physiology or Medicine in 1979 [Cierniak, 2011].



Although the most early applications of computerized tomography (CT) were for clinical imaging, the benefits and capability of three-dimensional internal characterization caused the rapid adoption of this technique in other fields, including materials science. In the early 1980s, the application of the CT technology was extended from the clinics to the research field. Since in this case the patient's safety is not a limitation, CT with higher resolution and exposure time can be used. The first X-ray micro tomography system was conceived and built by Jim Elliott in the early 1980s. The first published X-ray micro tomographic images were reconstructed slices of a small tropical snail, with pixel size about  $50 \mu\text{m}$  [Elliott and Dover, 1982]. Nowadays, micro-CT scanners having variable resolutions are offered by many manufacturers to fit a range of applications in industry and science.

### 2.3.1 Physics of X-radiation

X-radiation is part of the electromagnetic spectrum with a wavelength ranging from 0.01 to 10 nm, corresponding to frequencies in the range 30 petahertz to 30 exahertz ( $3 \times 10^{16}$  Hz to  $3 \times 10^{19}$  Hz) and energies in the range 100 eV to 100 keV. Furthermore, it is a form of ionizing radiation, i.e. it is capable of ionizing matter, which may be harmful, particularly to living tissue. X-ray wavelength is between ultraviolet light and gamma rays. Gamma radiation is also a form of electromagnetic radiation and equivalent to X-radiation at the same energies. The distinction between X-rays and gamma rays may be based on wavelength or on the radiation source. Sometimes X-radiation is considered to be radiation emitted by electrons, while gamma radiation is emitted by the atomic nuclei [Schörner, 2012].

Although X-ray radiation is known to have strong capability of penetrating matter, it still gets attenuated during scanning. When the X-ray photons pass through the material, radiation intensity decreases exponentially. This is due to the fact that some of the photons interact with the atoms within this material, either by the process of absorption or by the process of scattering (Fig. 2.5).

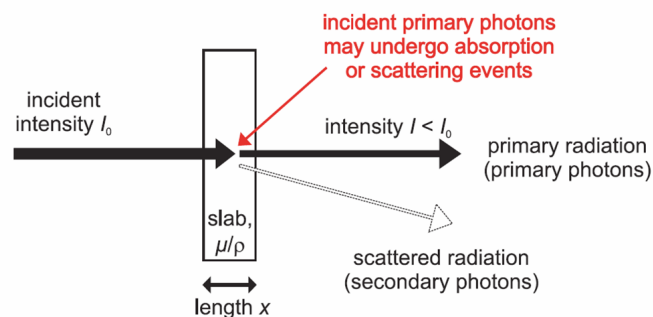


**Figure 2.5:** Schematic illustration of attenuation of incident radiation intensity  $I_0$  through a thin slab of homogeneous material with the mass attenuation coefficient  $\mu/\rho$  [Schörner, 2012].

The X-ray beam can be considered as a stream of particles, namely photons. While passing through the material, each individual photon might interact with the material by one of the following interaction phenomena [Schörner, 2012]:

- **Photoelectric Effect:** During this interaction, a photon uses up to all of its energy to eject an electron from an atom; while the electron will move around and ionize neighbouring atoms, there are no scatter photons and the photon is completely absorbed. Photoelectron absorption is the dominant process for materials with high atomic numbers.
- **Rayleigh Scattering:** This process, also known as coherent or classical scattering, occurs when the X-ray photon interacts with the whole atom so that the photon is scattered with no change in internal energy. Energies of the incident and scattered X-ray photon are the same in coherent scattering. However, they have different directions of propagation, which is expressed through a scattering angle (energy level remains the same, only angle changes)
- **Compton Scattering:** It occurs when the incident X-ray photon is deflected from its original path by interaction with the outer electron of an atom. The electron gains energy and is ejected from its orbital position, but the photon does not use all its energy. Therefore, the X-ray photon continues to travel in a different direction with less energy due to the interaction (both energy and traveling angle change).

Each of the interaction processes fundamentally alters the photon state, e.g. by changing its energy and/or momentum or by completely eliminating the photon. Because of this interaction between photons and matter, when a beam of X-rays is passed through the matter, some of the photons will either be absorbed or scattered; therefore, the intensity of the initial X-ray beams decreases the further it penetrates into matter. The attenuation of intensity of X-ray beam is described by the exponential Beer-Lambert law:

$$I(x) = I_0 e^{(-\frac{\mu}{\rho})\rho x}. \quad (2.1)$$

Here,  $I_0$  is the incident X-ray intensity,  $I(x)$  the intensity of the X-ray beam after having passed a penetration length  $x$  within the material, and  $\mu/\rho$  is mass attenuation coefficient which depends on the photon energy and material properties.

### 2.3.2 Principle of X-ray computed tomography scanning

X-ray computed tomography is a technique which allows reconstructing the 3D structure of objects non-destructively without any prior preparation, by acquiring radiographic projections from many different viewing angles from 0 to 360 degrees. The projections are the measured values of the overall attenuation that X-rays undergo when they pass through the object. X-rays passing through the material are absorbed according to a linear attenuation coefficient that has some spatial variation depending on the average atomic number, density and thickness of the material. At the end, with the help of a mathematical algorithm, a three-dimensional structure of the object can be reconstructed from these series of two-dimensional X-ray images. Generally, reconstruction algorithms can be classified as back-projection method, algebraic and Fourier-based reconstruction. In particular, the filtered back-projection is most commonly used for three-dimensional cone beam reconstruction. More details about this procedure are available in the textbook by Kak and Slaney [1988]. The reconstructed CT 3D-data essentially consist 3D of single cuboid volume elements, called voxels, representing the local attenuation coefficients. The resulting 3D images are typically displayed as a series of 2D slices.

The  $\mu$ -CT equipment used in the present investigation was a customized device manufactured by ProCon X-ray GmbH, Garbsen, Germany, denoted by CT Procon alpha 2000. This system is equipped with a micro-focus cone beam X-ray source, from which X-rays are emitted divergently. A 2D panel detector with the size of  $2304 \times 2304$  pixels is used to detect the X-ray intensities and translate them into local gray values at each pixel. The basic principle of X-ray scanning is depicted in Fig. 2.6. It is necessary to calibrate the detector to decrease the noise before scanning. This is done by bright/dark images correction, which takes the bright images without attenuation of the X-ray beam. The sample should be kept out of the equipment during this calibration.

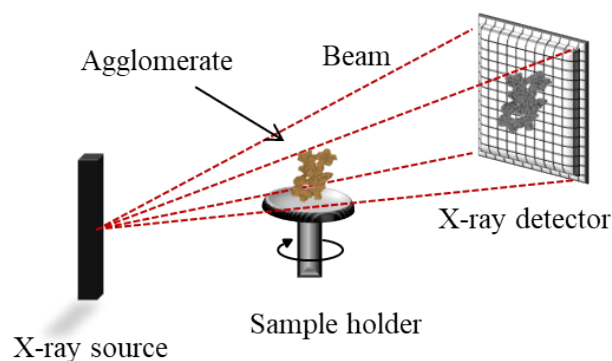


**Figure 2.6:** Principle of X-ray computed tomography scanning.

There are many factors influencing the precision and accuracy of the final volume X-ray image. Image quality depends on real density variation within the object and to the surrounding air. The energy of the X-rays has to be chosen in a way that the differences

in resulting linear attenuation coefficients between the main and surrounding material increase the contrast more than they increase the image noise. Control parameters such as X-ray tube potential, current and exposure time all affect the final image quality.

In order to obtain images with sufficient contrast and resolution from which the structural constituents can easily be separated, the X-ray source parameters were set at 50 kV and 110  $\mu A$ . The distance between detector and X-ray beam source was 380 mm, and the sample was located between them as close as possible to the source, at around 8 mm from the X-ray tube. This parameter setting led to a voxel resolution of 2.2  $\mu m$ . The voxel size determines the spatial resolution of the final image. Smaller voxel size results in images with high resolution and obviously provides more detailed information about the internal structure of the agglomerate. The closer a sample is adjusted to X-ray tube, the smaller is the voxel size that can be achieved. However, the constrain should be taken in to consideration that during the rotation of the sample by 360° (or at least by 180°) the projection image should not exceed the right or left border of the detector. After setting the exact position of detector and sample holder, and before starting the scanning, the center of rotation of the sample must be defined. The rotation center axis must be projected onto the detector center in order to ensure a correct reconstruction. This is done by adjusting a straight thin wire instead of the sample in the defined position.

Positioning an agglomerate on the sample holder is a challenging task since the maltodextrin agglomerates are very fragile and may break easily with even small pressure. On the other hand they should stick so firmly as to prevent any movement during scanning. Any slight movement during rotation steps leads to a blurred volume image. The agglomerate is fixed to the sample holder by double-sided tape in black color. The matt black color is used to minimize the sample holder effect in the final volume image and make it easier to extract it from the agglomerate in the respective image processing step.

All the CT scanning parameters should be checked precisely because they affect final image quality. To obtain a proper result, finding the right setting for a sample is critical. Here, each agglomerate was scanned individually within the entire range of 0-360° with a rotation step of 0.3°, so that the number of projections is 1200. Three images were taken per angular position, with an exposure time of 1500 ms. With this setting, the scanning required a long time of around 2 hours. The scanning time mainly depends on the number of projections images and exposure time. Due to the highly irregular structure of the maltodextrin agglomerates, taking less projections results in larger steps between the subsequent projections, consequently losing the smoothness and some information in the final volume image. In order to reduce scanning time, in the case of small agglomerates, two or three agglomerates were put together on the sample holder and scanned at the same time. When positioning more than one agglomerates on the sample holder, any contact point between them should be avoided in order to preserve the ability of separating them by image processing.

From these series of 2D projections, the 3D volume image of each agglomerate was reconstructed using Volex software (developed by Fraunhofer Institute for Integrated Circuits, IIS, Erlangen, Germany).

### 2.3.3 Removing artifacts

When the material has low density or atomic number and possesses a highly porous structure, it is difficult to be visualized properly, because it is not able to absorb enough energy during scanning. However, with the setting mentioned in the previous section (Trial 1 in Table 2.3), captured images for maltodextrin agglomerates with low density and high porosity have good intensity and contrast. But the images suffer from artifacts, specifically by a shadow around the agglomerate which is probably caused by scattering of the X-ray beam during the scanning (Fig. 2.7).

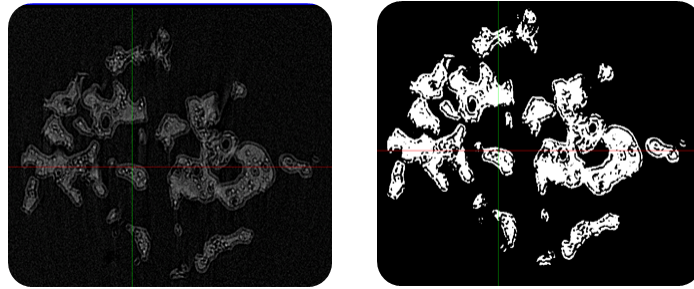


**Figure 2.7:** Scatter artifact shown as a shadow around the agglomerate for a 2D slice of: (a) gray value image and (b) binary image.

The effects of X-ray scattering are highly dependent on the specimen and X-ray energies used, becoming more prominent at higher energies [Davis and Elliott, 2006]. When the primary X-ray radiation interacts with the sample, it is attenuated either by complete photoelectric absorption of primary photons or by coherent and/or Compton scattering. Part of the incident X-ray photons are usually scattered in industrial CT. After interaction, the beam still exists (as scattered photons) but exhibits a different travel direction and possibly different energy than before. Scattered photons that reach the detector plane give rise to secondary signals usually at locations that are not correlated with the attenuation of the straight primary X-rays beam. Subsequently, scatter artifacts occur in the CT volume [Schörner, 2012]. For low energy X-rays, attenuation is primarily due to the photoelectric effect, and is proportional to  $Z^3/E^3$ , where  $Z$  is the atomic number, and  $E$  is the energy. At high energies, attenuation is primarily due to Compton scatter, and is proportional to  $1/E$  [Boas and Fleischmann, 2012].

The scattered radiation can be reduced by decreasing the energy of the photons which can be obtained by lower voltage of the X-ray source. Another solution to decrease scattered radiation is to use a wide shield, covering the entire front of the X-ray source. In order to eliminate scatter artifacts in our images, different experiments were done which

are summarized in Table 2.3. In this investigation, first it was tried to decrease the energy of the X-rays beam, but this resulted in losing the contrast of the image without any changes in the shadow around the agglomerate. In trial 2 and trial 3, the energy of the X-ray source was decreased by changing the voltage and current of the X-ray tube. Further decrease in energy was not acceptable because it was necessary to preserve the needed contrast in order to distinguish the solid and surrounding air phase. Using the shield as a filter was tried in the next step in order to diminish the scatter artifacts. In trial 4, all the other scanning parameters were set as in trial 1 but an aluminium foil was installed in front of the X-ray tube. Removing the shadow around the agglomerate was not achieved with this kind of filter. Finally in trial 5, it was observed that by using a plastic filter made of polymethyl methacrylate (PMMA) in front of the X-ray tube, the shadow around the object was removed. The filter reduces the beam intensity by eliminating X-rays which are not producing a useful signal.

**Table 2.3:** Different scanning settings of  $\mu$ -CT for removing the scatter artifact.

	Trial 1	Trial 2	Trial 3	Trial 4	Trial 5
Exposure time (ms)	1500	1500	2000	1500	1500
Voltage (kv)	50	45	35	50	50
Current ( $\mu$ A)	110	110	100	110	110
Energy (W)	5	3.4	2.5	5	5
No. of projection	1200	1200	1200	1200	1200
Voxel size ( $\mu$ m)	2.2	2.2	2.2	2.2	2.2
Type of filter	-	-	-	Aluminium foil	PMMA plastic
Scattering artifact	Yes	Yes	Yes	Yes	No

## 2.4 Image processing

In order to obtain the data required for morphological and microstructural analysis, different steps of image processing need to be performed on the X-ray images. The conducted image processing steps were as follows. At first, the volume of interest was extracted. This volume was considered as the part of the image containing the agglomerate on which the image analysis was performed. Then, segmentation (binarization) was performed for separating the pixels of the gray-scale images into background and foreground. Based on Otsu's thresholding method [Otsu, 1979] a binary image was created: the value 1 (white) was assigned to all the pixels with intensity higher than the given gray tone value (threshold), while the value 0 (black) was assigned to the other pixels, i.e. pores and background. Based on our experience, image segmentation is the most crucial step affecting subsequent quantitative analysis, especially the porosity of internal pores and the specific surface area. Before

further analysis, all images were smoothed with a median filter to eliminate noise. Sample holder effects were removed by the labeling and object filtering method. Finally, the volume image of the internal microstructure of the agglomerate was visualized. The qualitative and quantitative analyses were performed on these binary volume images. For basic image processing steps, the MAVI software developed by Fraunhofer Institute for Technical and Industrial Mathematics in Kaiserslautern, Germany, was used. For further analysis (i.e. separating primary particles, calculating porosity and sphericity, visualization of particles and pores) additional image processing operations conducted with the Matlab (version R2012b) code and its Image Processing Toolbox are necessary.





## Chapter 3

# Morphological and structural characterization of agglomerates

*This chapter is a modified version of the paper "Three dimensional characterization of morphology and internal structure of soft material agglomerates produced in spray fluidized bed by X-ray tomography, Powder Technology (2016)".*

### 3.1 Introduction

The physical properties of a material are strongly influenced by its internal microstructure, which is created during processing. Despite the amount of research on maltodextrin agglomeration, the internal microstructure and morphology of this kind of agglomerates have rarely been investigated, especially in three dimensions. Here, for two-dimensional analyses, the size and shape of the primary particles and of the agglomerates were studied with a Camsizer. The results are presented in terms of the evolution of the median diameter, particle size distribution and circularity. The 3D microstructure of individual agglomerates (obtained by X-ray micro tomography) is visualized down to details that contain valuable information such as the actual morphology and spatial distribution of primary particles and pores, which cannot be assessed by other techniques. By further processing of the X-ray image sequences, the micro-scale morphology of soft agglomerates made of maltodextrin particles is studied and the results are evaluated quantitatively. The internal porosity and the pore size distribution of the primary particles as well as of the agglomerates are obtained and evaluated. The open pores of the agglomerates, which comprise relatively large cavities and channels, are also determined from the X-ray images. The open porosity of agglomerates is calculated by three different methods, i.e. convex hull, dilation and radius of gyration, and the results are compared. The bulk porosity is also measured for maltodextrin particles before and after agglomeration. The shape of the agglomerates is analyzed in terms of sphericity and compared with two-dimensional values. Moreover, a comprehensive methodology is developed based on the segmentation method using preflooded

watershed transform to distinguish and separate the primary particles in maltodextrin agglomerates. The gyration radius and fractal dimension of agglomerates are also calculated based on the separated primary particles. All the mentioned characterization is applied to agglomerates produced by Trial D (Table 2.2).

## 3.2 Separation of primary particles in the agglomerate

Separation and distinction of the primary particles comprised in an agglomerate is an important and challenging issue for analyzing the morphology of the agglomerate. When the primary particles are spheres or have some other well-defined shape, it is much easier to distinguish them in the agglomerate structure. Amorphous materials such as maltodextrin have an unknown a priori shape and structure. Moreover, the structure deforms during the agglomeration process because of water absorption, mostly at the contact points between the primary particles.

In this study, the separation of primary particles in the agglomerate is done by segmentation of X-ray images using the pre-flooded watershed method. Applying the watershed method without considering limitations that can be checked by separate measurement may not, though, yield reasonable results.

The process of separating objects from the image background, as well as from each other is called segmentation. There are many different ways to perform image segmentation. Segmentation methods for identifying and separating foreground regions include labeling and the watershed transformation. The input data for labeling is a binarized image, whereas the watershed transformation requires a gray-level image. After labeling, the output image contains discrete label values for each pixel, identifying connected regions. Therefore, the labeling method is not applicable for separating the primary particles of an agglomerate, as these are connected objects.

The watershed transformation is a more complex and powerful morphological technique for image segmentation [Bleau and Leon, 2000; Tahmasebi and Sahimi, 2015]. The basis of watershed is topographic representation of a gray-level image, which includes three basic notions: minima, catchment basins and watershed lines. Imagine the bright areas to have "high" altitudes and the dark areas to have "low" altitudes. Suppose that there is a hole in each local minimum through which water can flow out with a constant flux and that when two basins merge, a dam is built: the set of all dams defines the so-called watershed lines. Such lines represent the watershed boundaries that are good indicators for feature partitioning. During this process, watershed lines get the label 0, whereas each basin is assigned a specific label different from 0. Usually, the standard morphological watershed transformation applied to gray-value images results in strongly over-segmented images.

Over-segmentation occurs because every regional minimum, even if small and insignificant, forms its own catchment basin. It can be somewhat improved by filtering, but this does not solve the problem completely. To decrease the over-segmentation of watershed-based techniques, several approaches have been proposed in the literature [Bleau and Leon, 2000; Belaid and Mourou, 2009]. General strategies to avoid over-segmentation are pre-processing, modification and post-processing of the image.

A modification with straightforward interpretation to overcome over-segmentation is the volume preflooded watershed algorithm, in which basins with a volume below a specified value are merged with neighboring basins during the watershed process [Ohser and Schladitz, 2009]. The algorithm is altered in the following way: During the flooding of the image, at each step the pixels of the created basins are counted. If their number is larger than a specified minimum, a new basin is created with a watershed line. If the number of pixels is below the value, however, then the basin is discarded and thus prevented from creating watersheds. In this case, it will be integrated into a bigger basin.

The maltodextrin agglomerates produced in this work are highly porous and also the differences in gray value between air and substance are not very large, due to the low density of maltodextrin. Therefore, the gray-level images exhibit some noise in pores and in the air surrounding the agglomerate. Although by the volume preflooded watershed method the over-segmentation is reduced, some unwanted segmentation still appears in the surrounding area. Since only a separation of the primary particles in the agglomerates is required, an additional step is used to eliminate the segmentation of the air phase.

In order to eliminate the noise and to smoothen the image properly, it is binarized first by thresholding segmentation. In this case only the solid material gets the label 1 (foreground) and the surrounding area gets the label 0 (background). As mentioned before, gray-value images are required for the watershed transformation in order to find the minimal values. In this regard, a Euclidean distance transform is applied to the binarized X-ray images. This transformation computes the absolute or squared Euclidean distance of each background pixel to the closest foreground pixel. It produces a gray-value image of the same size as the original image. Then, by using the preflooded watershed transformation on this image the segmentation and partitioning of the system occur only for the agglomerate. Therefore, when combined with the Euclidean distance transformation, the preflooded watershed can be used for the separation of connected primary particles of an agglomerate. It should be noted that the minimal number of pixels in preflooded watershed should be defined properly in order to have a reasonable separation procedure.

Using the data extracted from the volume images after segmentation, the primary particles can be labeled and counted, providing the number  $N_p$  of primary particles in each agglomerate. The center coordinates, volume and surface area of each primary particle can

also be identified. Each separated primary particle of the agglomerate can also be considered as a sphere with the volume and center coordinates of the actual primary particle. By considering each primary particle as a sphere with same volume and center coordinate, the spherical representation model for an agglomerate can be depicted (Fig. 3.1).

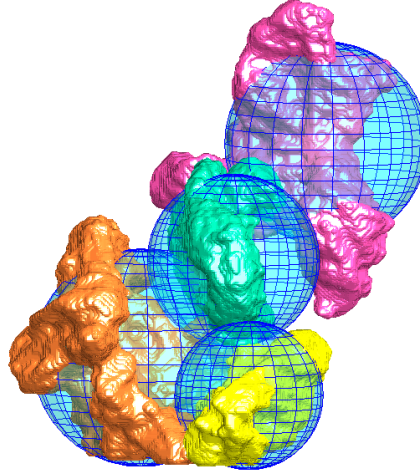


**Figure 3.1:** Spherical representation model for an agglomerate with separated primary particles.

### 3.3 Moment of inertia and radius of gyration

Mass moment of inertia is a measure of an object's resistance to changes in rotation direction, which depends on the distribution of mass in the body with respect to the axis of rotation. The moment of inertia for an agglomerate with respect to its center of gravity,  $I_G$ , is an extension of the concept of moment of inertia with respect to an axis, and it is equivalent to half of the sum of the moments of inertia with respect to three orthogonal axes intersecting at the center of gravity of the agglomerate [Lapuerta, Martos, and Martín-González, 2010]. It can be calculated as the sum of the contributions of all the solid elements composing the agglomerate:

$$I_G = \lim_{\Delta m \rightarrow 0} \sum x_i^2 \Delta m_i = \int x^2 dm, \quad (3.1)$$

where  $x$  is the distance between any point belonging to the agglomerate and the center of gravity and  $m$  is the mass of each element.

Gyration radius,  $R_g$ , is one of the basic properties to characterize an agglomerate. The moment of inertia ( $I_G$ ) of a body is often defined in terms of its radius of gyration, which is the distance from the center of gravity of the agglomerate to a point where the entire mass

of the agglomerate ( $M$ ) has to be concentrated to have same moment of inertia as the real body (Fig. 3.2). Therefore, the radius of gyration is obtained as:

$$I_G = \int x^2 dm = R_g^2 \int dm = R_g^2 M \rightarrow R_g = \sqrt{\frac{I_G}{M}}. \quad (3.2)$$

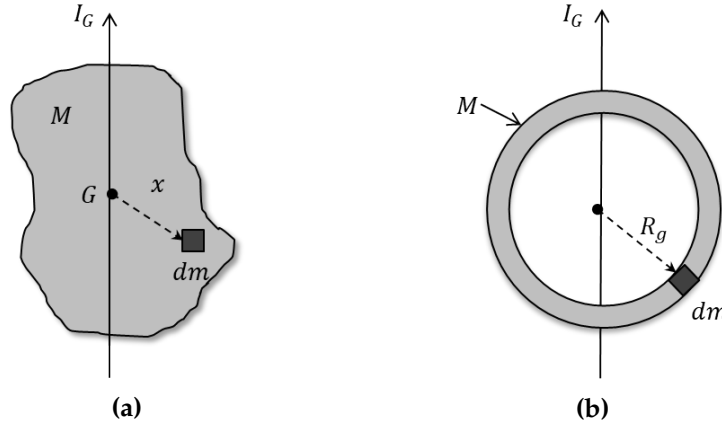


**Figure 3.2:** The graphical principle of estimating moment of inertia (a) and radius of gyration (b).

The radius of gyration is a geometric measure of the spatial mass distribution around the agglomerate center of mass. Therefore, it describes not only the size of an object, but also shows how the mass is distributed around the gravity center. Two objects with the same mass or volume can have different radii of gyration, in which lower value indicates that the mass of the object is distributed more uniformly around the gravity center. As shown in Fig. 3.3, two maltodextrin agglomerates with same solid phase volume ( $0.186 \text{ mm}^3$ ) have different values of radius of gyration. The agglomerate of Fig. 3.3a in which the mass is distributed more uniformly, has lower value of  $R_g$  in comparison to the agglomerate of Fig. 3.3b.

For an object with polydisperse separated elements or particles the radius of gyration is calculated as:

$$R_g^2 = \frac{\sum_{i=1}^{N_p} x_i^2 m_i}{\sum_{i=1}^{N_p} m_i} = \frac{\sum_{i=1}^{N_p} x_i^2 \rho_i V_i}{\sum_{i=1}^{N_p} \rho_i V_i} = \frac{\sum_{i=1}^{N_p} x_i^2 V_i}{\sum_{i=1}^{N_p} V_i}, \quad (3.3)$$

where  $N_p$  is the number of particles,  $m_i$  the mass and  $x_i$  the distance of particle  $i$  to the agglomerate center of mass.  $\rho_i$  and  $V_i$  are the density and volume of each primary particle, respectively. Since the density is constant for all particles, the radius of gyration can be reported based on the volume of particles.

If the particles are monodisperse, i.e. of same size and volume, Eq. 3.3 can be transformed to

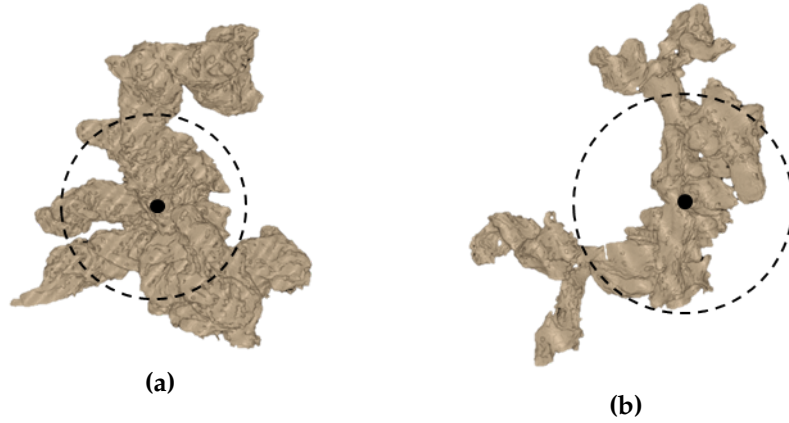


**Figure 3.3:** Different radii of gyration for two agglomerates with identical solid phase volume ( $0.186 \text{ mm}^3$ ): (a) 0.48 mm, (b) 0.57 mm.

$$R_g^2 = \frac{1}{N_p} \sum_{i=1}^{N_p} x_i^2 = \frac{1}{N_p} \sum_{i=1}^{N_p} (r_i - r_G)^2, \quad (3.4)$$

where  $r_i$  is the position vector of each primary particle and  $r_G$  is the position vector for the center of mass of the object. In Eq. 3.4, the gyration radius is the root mean squared distance of all particles from the center of mass of the agglomerate. It can also be described as the root mean squared distance between each two primary particles. Thus, Eq. 4 can be written as [Teraoka, 2002]:

$$R_g^2 = \frac{1}{2N_p^2} \sum_{i=1}^{N_p} \sum_{j=1}^{N_p} (r_i - r_j)^2, \quad (3.5)$$

where  $r_i$  and  $r_j$  are the position vectors of the  $i^{\text{th}}$  and  $j^{\text{th}}$  constituent particles, respectively. This formula indicates that one can use the mean square distances between all pairs of primary particles to obtain  $R_g$ , instead of first calculating  $r_G$  and then the mean square distance between  $r_G$  and each primary particle. As we have the center coordinates of each primary particle, the radius of gyration can be calculated for different agglomerates. Without having 3D data, the determination of the radius of gyration is practically impossible.

### 3.4 Porosity

The porosity can be defined based on the size and gray value of the pixels comprised in a volume image obtained from the X-ray  $\mu$ -CT method. Mathematical morphology is a powerful tool for geometrical analysis and description, which contains a broad set of operations that process images based on shapes. All morphological operators take two pieces of data as their input. One is the input image, which may be either binary or gray scale for most

of the operators. The other is the structuring element, which determines the precise details of the effect of the operator on the image. Morphological operations apply a structuring element to an input image, creating an output image of the same size. In a morphological operation, the value of each pixel in the output image is based on a comparison of the corresponding pixel in the input image with its neighbors. By choosing the size and shape of the neighborhood by structuring elements, a suitable morphological operation that is sensitive to specific shapes in the input image can be constructed. Different types of porosity are used in food process design and for food product characterization [Ratti, 2009]. These are discussed in the following sections.

### 3.4.1 Porosity of closed pores (Internal porosity)

The closed porosity is defined as the ratio of the inner pore volume inside the compact solid material,  $V_{cp}$ , to the volume of solid phase, including internal pores in the agglomerate,  $V_{s,cp}$ . This porosity is mostly attributed to the primary particle structure and is defined as:

$$\varepsilon_{cp} = \frac{V_{cp}}{V_{s,cp}} = 1 - \frac{V_s}{V_{s,cp}}. \quad (3.6)$$

The volume of the compact solid phase in the agglomerate,  $V_s$ , can be obtained directly from a binary image, however further image processing is required in order to obtain  $V_{s,cp}$ . An example of this procedure is shown in Fig. 3.4.

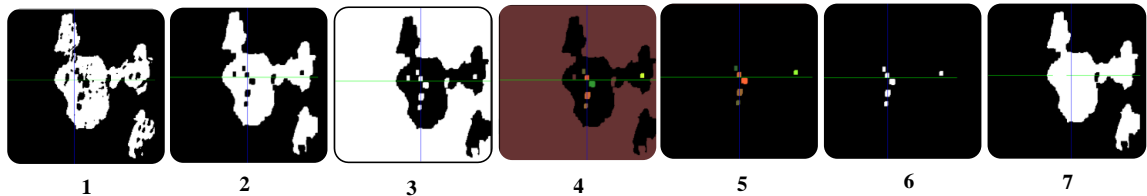


**Figure 3.4:** Image processing sequences applied for filling the internal pores and for calculating the volume of the solid phase including internal pores in the aggregate,  $V_{s,cp}$ : (1) binary image, (2) closing morphology (filling small pores), (3) complement (inversion of the images), (4) segmentation-labeling (identification of big pores and surrounding air), (5) object filter (filtering out the surrounding air), (6) binarization, (7) combination of images 2 and 6 (filling of all internal pores). In the first and last image, white pixels belong to the solid phase and black pixels to the air.

To calculate the total volume of the solid phase, including internal pores in the agglomerate, the internal pores should be filled. For this purpose, the mathematical morphology operation of closing can be performed on the volume images obtained by  $\mu$ -CT. Closing is an operator that enlarges the boundaries of foreground regions in an image and shrinks the background, such that small holes within the image are filled (closed). Morphological

closing of an image consists of a dilation followed by an erosion operation with the same structuring element. Therefore, it is less destructive than other morphological operations and it preserves the original size, shape and convexity of the analyzed structure. The closing operation requires definition of a structuring element (SE). This structuring element determines the precise effect of the closing operation on the input volume image.

The size and shape of the structuring element should be defined in a way to avoid any remaining unfilled pores within the volume image. Special care should be also taken to control and preserve the exterior surface of the agglomerate. Having performed several tests with different structuring elements, it was observed that the closing method results in an undesired deformation of the exterior surface of the agglomerate, when applied to fill some of the larger internal pores. Therefore, in this work only the small pores were filled with the closing method. This step was used to fill in particular the small pores which were near the exterior surface of the agglomerate and were connected to the surrounding air. After inverting the image in the next step, the air was labeled. In this way, the surrounding air and the larger pores are assigned different labels. After filtering out the surrounding air and after binarizing the images, the larger internal pores of the agglomerate can be filled by adding the corresponding binarized image to that of filled (closed) small pores.

Fig. 3.4 illustrates the procedure on a two-dimensional slice of the volume image. 3D views of the agglomerate before and after filling its internal pores as well as the internal pore space are shown in Fig. 3.5. The compact and the total solid phase volume of this agglomerate are  $V_s = 5.25 \times 10^{-2} \text{ mm}^3$  and  $V_{s,cp} = 6.63 \times 10^{-2} \text{ mm}^3$ , respectively. By subtracting Fig. 3.5a from Fig. 3.5b, the morphology of the internal pore space becomes accessible (Fig. 3.5c). After filtering the noise of this volumetric image of pores, the size and spatial distribution of internal pores are obtained.

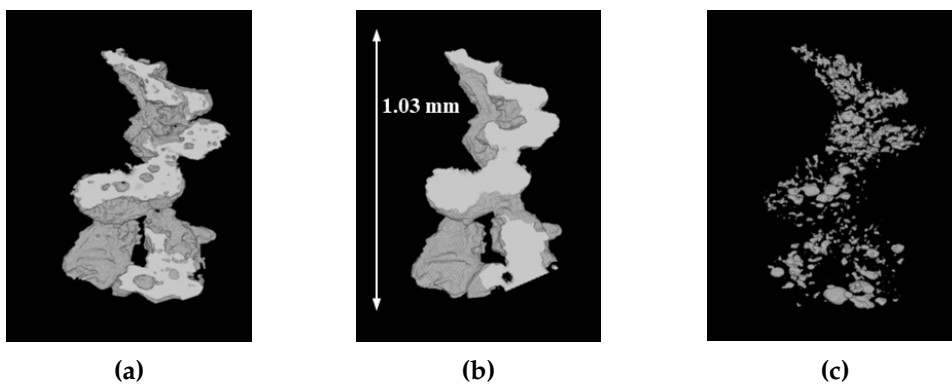


**Figure 3.5:** Cross-sectional 3D volume view of agglomerate: (a) before and (b) after filling the internal pores, and (c) internal pore space.



### 3.4.2 Spatial and size distribution of internal pores

In order to visualize properly the spatial distribution of pores inside the solid phase of the agglomerate, the 3D data matrix of the agglomerate and of its pores is generated individually. In order to achieve this, the original volume image of the agglomerate and its pores (generated by MAVI) is sliced in one spatial direction into a series of 2D binarized images. Then, by using an additionally developed Matlab code, for each slice the spatial coordinates and values of pixels are stored in a 2D matrix. Finally, by combining these 2D matrices the overall 3D matrix is generated. The size distribution of internal pores is evaluated by the spherical granulometry function. In mathematical morphology, granulometry is an approach to compute the size distribution of grains in binary images, using a series of morphological opening operations. The spherical granulometry assigns to each set of topologically connected pixels the diameter of the largest ball completely contained in the foreground and covering this set of pixels. The granulometric analysis is applied to the 3D  $\mu$ -CT images of the internal pores and yields a volume weighted generalized pore size distribution.

### 3.4.3 Porosity of open pores

An open pore is a cavity or channel that is connected to the exterior surface of the agglomerate. The porosity of an open pore is defined as:

$$\varepsilon_{op} = 1 - \frac{V_{s,cp}}{V_{agg}}. \quad (3.7)$$

For calculating the open porosity, defining the total volume of the agglomerate,  $V_{agg}$ , is a challenging issue. In this study, three different methods were applied and compared: convex hull, dilation and radius of gyration. The three procedures are illustrated for one small agglomerate in Fig. 3.6. The gray regions in Fig. 3.6 are considered as open pore space.

#### Porosity from the radius of gyration

The central moment of inertia of a spherical agglomerate with an equivalent radius  $R_e$  can be calculated as:

$$I_G = \int_0^{R_e} R^2 dM = \int_0^{R_e} R^2 \rho dV = \int_0^{R_e} 4\pi R^4 \rho dR = \frac{4\pi}{5} R_e^5 \rho, \quad (3.8)$$

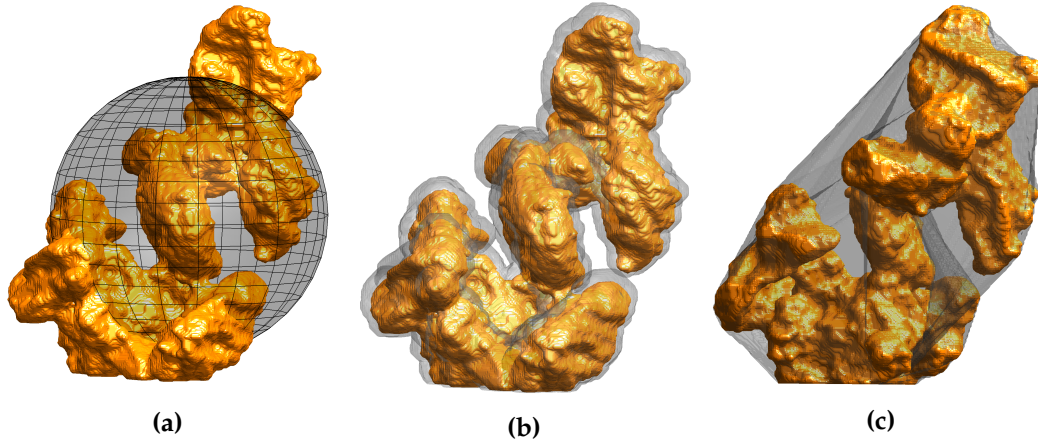


**Figure 3.6:** 3D volume views of the same maltodextrin agglomerate for which the total volume is calculated based on three methods: (a) equivalent radius from the radius of gyration, (b) dilation, and (c) convex hull.

where  $\rho$  is the apparent density of the agglomerate. At the same time, the mass of the equivalent sphere can be expressed by:

$$M = \frac{4\pi}{3} R_e^3 \rho. \quad (3.9)$$

Substituting Eqs. 3.8 and 3.9 into the definition of the radius of gyration, Eq. 3.2, the radius of the equivalent sphere,  $R_e$ , can be expressed as a function of the radius of gyration of the agglomerate,  $R_g$ :

$$R_e = \sqrt{\frac{5}{3}} R_g. \quad (3.10)$$

With known radius of gyration,  $R_g$ , the equivalent radius,  $R_e$ , and then the total volume of the agglomerate,  $V_{agg}$ , can be calculated. Inserting  $V_{agg}$  in Eq. 3.7, the agglomerate porosity is obtained. In order to simplify the calculation process, the radius of gyration is obtained based on Eq. 3.4.

### Porosity by dilation

The most basic morphological operations are dilation and erosion. Dilation adds pixels to the boundaries of objects in an image, while erosion removes pixels at object boundaries. The number of pixels added or removed from the objects in an image depends on the size and shape of the structuring element used to process the image. In the morphological dilation and erosion operations, the state of any given pixel in the output image is determined by applying a rule to the corresponding pixel and its neighbors in the input image. In the

dilation method, the gray value of any output pixel is the maximum gray value of all the pixels in the neighborhood of the corresponding input pixel. In a binary image, if any of the pixels is set to value 1, the output pixels for all defined neighbors are also set to 1. In this work, the structuring element with a shape of an approximate ball with a size of 3 pixels was applied to the binary images of individual agglomerates. Setting the volume of the dilated agglomerate equal to the total volume,  $V_{agg}$ , Eq. 3.7 can again be used to compute the porosity of open pores.

### Porosity by convex hull

The convex hull of a set is defined as the smallest convex polygon or polyhedron located in a multidimensional data space which contains all set points (vertices of an object). In the present work the convex hull volume for the 3D image of each agglomerate is calculated by the MAVI software, in which the convex hull is formed by planes perpendicular to the 13 normal directions. By inserting the convex hull volume in Eq. 3.7, the open pore porosity is obtained. For visualization, the minimal convex hull that envelops the agglomerate is computed for each cross sectional binary image with the `bwconvhull` function from Matlab. The three-dimensional reconstruction of the convex hull is done by creating a 3D matrix from all the 2D cross sectional convex hulls with an additionally developed Matlab code.

#### 3.4.4 Bulk porosity

The bulk porosity is the volume fraction of voids outside the boundary of individual particles when packed or stacked [Ratti, 2009]. In this study, the agglomerates and primary particles are filled in a cylindrical tube separately. The method of preparing the packed bed is loose random packing; material is dropped into the bed without any pressure or vibration. Each filled bed is scanned individually by X-ray tomography. Then, a certain volume,  $V_b$ , at the center of the packed bed is analyzed and its void space ratio is determined by image processing (Fig. 3.7).

Since the definition of bulk porosity corresponds to extra void space in a bed, it is calculated as the ratio:

$$\varepsilon_b = 1 - \frac{V_{s,cp}}{V_b}. \quad (3.11)$$

With this definition the internal pores which belong to the primary particle structure are not considered in the bulk porosity. The resulting porosity is called the true bulk porosity in [Börjesson et al., 2014]. The compact solid phase volume  $V_s$  can be used, instead of the porous solid phase volume  $V_{s,cp}$  in Eq. 3.11, to calculate bulk porosity. In this case, the

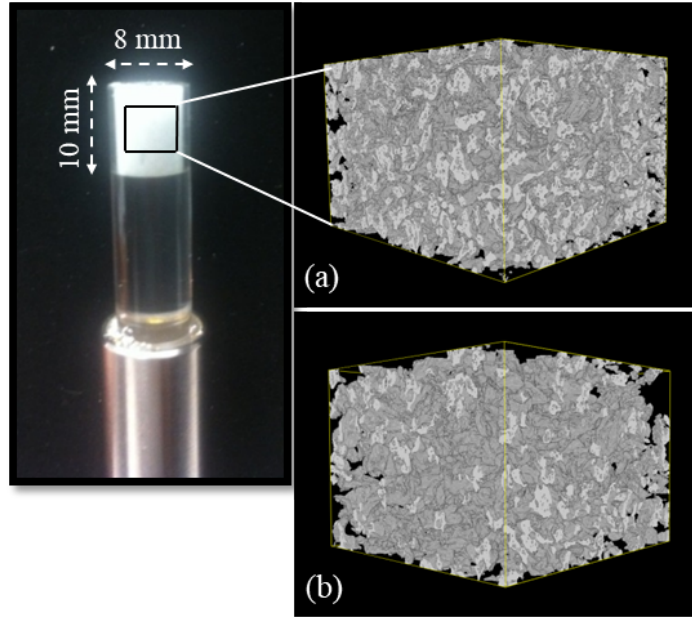


**Figure 3.7:** 3D view of a maltodextrin packed bed filled with (a) primary particles and (b) agglomerates.

resulting porosity includes all pores in the bed, even internal porosity. In this work, as a reference and comparison, the bulk porosity using the compact solid volume has also been calculated. The compact solid volume is evaluated based on the number and size of pixels. For finding the total volume of the porous solid phase of all agglomerates,  $V_{s,cp}$ , first all the internal pores are filled and then the volume is calculated as in the procedure for calculating the internal porosity (Sec. 3.4.1).

### 3.5 Circularity and sphericity

The circularity is commonly used in 2D shape analysis. It is defined as the degree to which the particle is similar to a circle and it is a function of the perimeter  $P$  and the cross sectional area  $A$  of the agglomerate [Bagheri et al., 2014]:

$$C = \frac{4\pi A}{P^2}. \quad (3.12)$$

The required data for evaluation of circularity is obtained from measurements by the Camsizer equipment.

In three-dimensional shape analysis, the sphericity describes how closely the particle resembles a sphere. It is defined as the surface area of a sphere with the same total solid phase volume of agglomerate  $V_{s,cp}$ , divided by the surface area  $S$  of the real 3D object [Hafsa et al., 2014]:

$$\Phi_S = 6\sqrt{\pi} \frac{V_{s,cp}}{\sqrt{S^3}}. \quad (3.13)$$

The precision and accuracy of the volume and surface area determination are important for sphericity analysis. These quantities can be obtained from X-ray images. For spherical particles,  $\Phi_S$  equals unity, while for other particles it is below 1.

### 3.6 Fractal dimension

Maltodextrin agglomerates produced in a spray fluidized bed are composed of primary particles which form irregular structures. A common way to quantify this irregularity is by using the fractal dimension, which is very useful for describing shapes and the way an object fills the space, being a good measure for the structural compactness of the object. The value of fractal dimension ranges from unity for strings to three for regular three-dimensional objects, and it can have a non-integer value. If the value is about three, it means that the object has a compact structure and fills the space like a rigid sphere or cube. Agglomerates grown by particle collisions exhibit a power law scaling between the number of primary particles and radius of gyration [Eggersdorfer and Pratsinis, 2012]:

$$N_p = K_f \left( \frac{R_g}{R_p} \right)^{D_f}, \quad (3.14)$$

where the exponent  $D_f$  is the fractal dimension,  $R_p$  is the mean radius of primary particles in each agglomerate, and  $K_f$  is the fractal prefactor. The parameters  $K_f$  and  $D_f$  can be determined from a logarithmic plot of the number of primary particles ( $N_p$ ) versus the ratio  $\left( \frac{R_g}{R_p} \right)$  by linear regression. This statistical scaling law can still be used to characterize agglomerates which are not strictly fractal [Köylü, Xing, and Rosner, 1995; Melas et al., 2014].

## 3.7 Results and discussion

### 3.7.1 Primary particle separation and gyration radius

In the separation of primary particles with the preflooded watershed transformation (Sec. 3.2), the minimal pixel number has a great influence on the number of separated objects. For several values of the minimal pixel number the number of separated primary particles was determined for a series of maltodextrin agglomerates. A rough estimate for the number of primary particles is also calculated based on the volume of the porous solid phase

in the agglomerate obtained from the associated X-ray images and on the median volume of the primary particles used in the agglomeration process. By comparing these two ways of determination, it can be concluded that a reasonable number of primary particles is obtained for a minimal pixel number in the range of 10000-15000. Table 3.1 shows a typical evaluation of the effect of the minimal pixel number on the number of separated primary particles in one agglomerate. Note that before the segmentation process the internal pores of the primary particles were filled because of two reasons: First, to prevent the segmentation of primary particles due to the existence of internal porosity. Second, to maintain the consistency with the rough estimation in which the total volume of primary particles, including internal porosity, is considered. The method used for the filling of the internal pores has been discussed in Sec. 3.4.1.

**Table 3.1:** The effect of minimal pixel number in the preflooded watershed transform on the number of separated primary particles for one exemplary agglomerate.

Minima pixel number	10	50	500	5000	10000	12000	20000
Number of primary particles	42	22	14	9	5	5	4

Since the primary particles are not spherical, their radii are reported in 13 discrete directions of the cuboidal lattice (3 coordinate directions, 6 face diagonals, 4 space diagonals). This data is stored in matrices for further evaluation. By approximating each primary particle by a sphere with equal volume the corresponding sphere diameter is calculated.

A 3D view of an agglomerate with primary particles separated by using different minimal pixel numbers for the segmentation is shown in Fig. 3.8a. Also, from the center coordinates and diameter of each primary particle, the spherical model of the agglomerate can be constructed (Fig. 3.8b). The polydispersity of the primary particles comprising the agglomerate is recognizable in this figure. The dispersity is overestimated for a small minimal pixel number but it decreases noticeably at higher minimal pixel number.

The watershed transform with minimal pixel number of 12000 was used in combination with the Euclidean distance transform to separate the connected primary particles for more than 60 maltodextrin agglomerates. In order to assess the accuracy of the primary particle sizes obtained from the segmentation of the  $\mu$ -CT volume images, they have been compared with the particle size distribution before agglomeration (Fig. 3.9). In this comparison, the size of the separated primary particles from the X-ray images is considered as the equivalent diameter  $d_V$  of spheres with equal volume. The size distribution of the primary particles before agglomeration was investigated based on their projected images by the Camsizer. Since the primary particles of maltodextrin are not spherical, their size can be represented in several ways. As the Camsizer image is not three-dimensional, for comparison with X-ray images, the size of primary particle with equal projected area,  $d_A$ ,

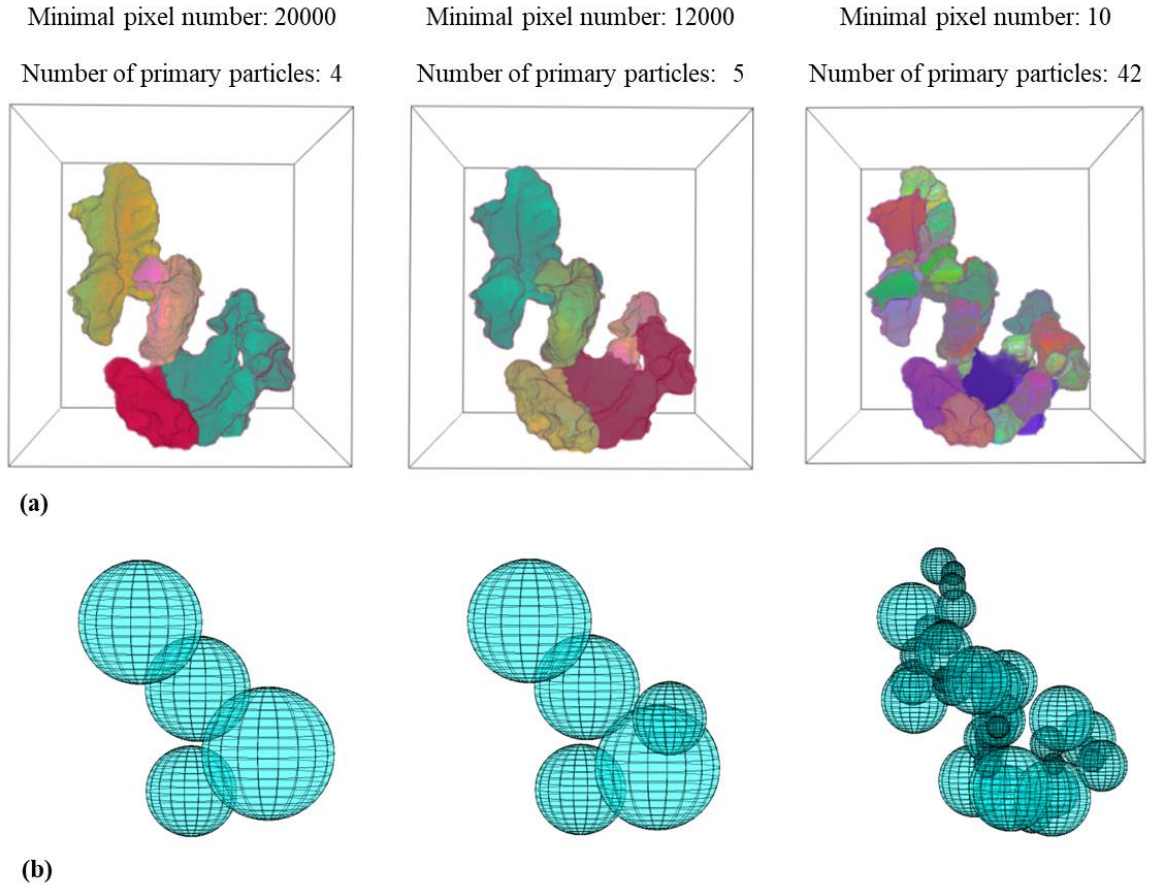


**Figure 3.8:** Primary particle separation of an agglomerate for different values of the minimal pixel number: (a) real structure of primary particles, (b) approximation of each primary particle by a sphere with equal volume.

can be obtained first ( $d_A$  is the diameter of a disk with the same area as the particle's projection). As shown in Fig. 3.9, there is a difference between the numbers obtained by these two methods. The particle size  $d_A$  is about 13% larger than  $d_V$  which is calculated from the 3D X-ray images. In principle,  $d_A$  may be smaller or larger than  $d_V$ , depending on the particle shape and projection. However the equivalent diameter of a disk with equal area is often larger than the other equivalent diameters: Elongated particles show significantly larger values for  $d_A$  than for  $d_V$  [Merkus, 2009]. Therefore, a larger value of  $d_A$  compared to  $d_V$  is acceptable for maltodextrin primary particles, which have an irregular shape. Another diameter used to represent the particle size in 2D is the Feret diameter. In general, it can be defined as the distance between the two parallel planes restricting the object perpendicular to a given direction in space. Minimum and maximum Feret diameters are obtained by using many such directions. According to Califice et al. [2013], the diameter from 2D image analysis that best matches the true 3D size of particles is the minimum Feret diameter ( $d_{FeMin}$ ). As shown in Fig. 3.9, the size distribution based on  $d_{FeMin}$  is in a good agreement with the  $d_V$  distribution. This comparison shows that the size of the separated primary particles obtained by the segmentation method matches quite well the primary particle size distribution which was measured before the agglomeration process. It should be noted that

more than a million primary particles were measured in the Camsizer, but only around 500 primary particles were separated and measured by the  $\mu$ -CT device in this study.

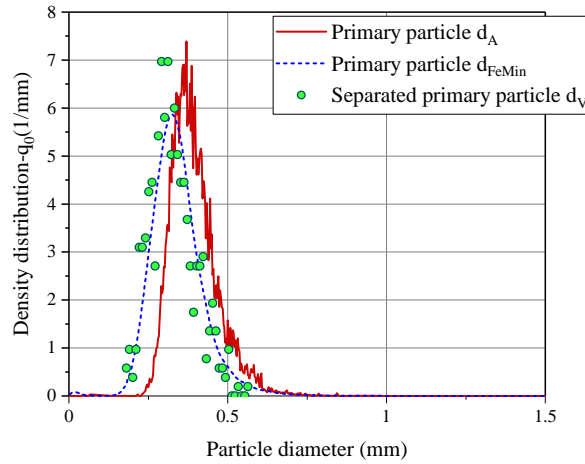


**Figure 3.9:** Size distributions of primary particles obtained from  $\mu$ -CT images using the segmentation method ( $d_V$ ) and from the Camsizer ( $d_A, d_{FeMin}$ ).

Number ( $q_0$ ) and volume ( $q_3$ ) size distributions of agglomerates obtained from the Camsizer as well as the gyration diameters ( $2R_g$ ) calculated from the  $\mu$ -CT images are shown in Fig. 3.10. The gyration diameters of 22 agglomerates lie in five classes with size range from 0.51 to 1.24 mm and a mean value of 0.8 mm. The median value of the minimum Feret diameter ( $D_{FeMin}$ ) of agglomerates from the  $q_3$  distribution is 0.642 mm. The difference between Camsizer size distributions and the radius of gyration is expected as the latter one describes not only the agglomerate size, but also how the mass is distributed around its center of gravity (see Sec. 3.2). It should also be noted that the samples analyzed by the Camsizer contained some agglomerated primary particles and some very fine particles which could not be separated from the original feed. The last two groups of particles result in the left-hand side branches of the Camsizer distributions in Fig. 3.10, but they are missing in the distribution of gyration diameter, because only agglomerates with different sizes were picked up for  $\mu$ -CT analysis.

### 3.7.2 Internal porosity (closed pores)

Three different structuring elements (SE) were tested for filling the small closed pores in the interior of the primary particles in the agglomerate: an approximate ball with size 3 (SE-Ball 3), a cube with size 3 (SE-Cube 3) and a cube with size 5 (SE-Cube 5). After using these three types of structuring elements for each agglomerate and after filling the larger closed pores by means of the complementing and labeling method (Sec. 3.3.1), the entire internal structure of the agglomerate was mapped in order to verify that all the internal closed pores were filled. In Fig. 3.11, the effect of the shape and size of the structuring element on



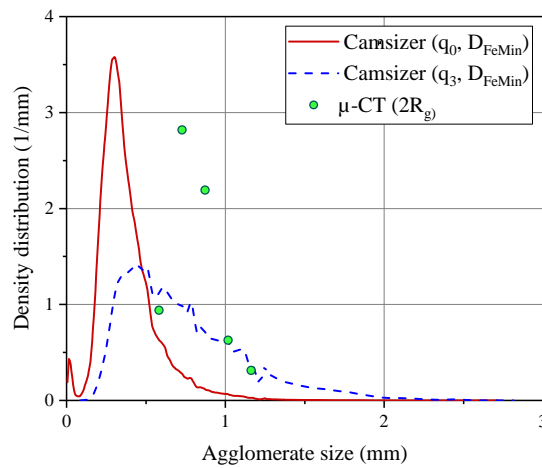


**Figure 3.10:** Size distributions of agglomerates obtained from the Camsizer and distribution of gyration diameter obtained from the  $\mu$ -CT images.

the cumulative pore size distribution is illustrated. The porosity values obtained with SE-Cube 3, SE-Cube 5 and SE-Ball 3 are 8.7%, 13% and 18%, respectively. The differences in these values show the importance of choosing a suitable structuring element. After these structuring elements were applied to several different agglomerates, it was concluded that the SE-Ball 3 is the most suitable one. By this element, all the pores inside primary particles of the agglomerate are filled while the outer surface structure remains unchanged.

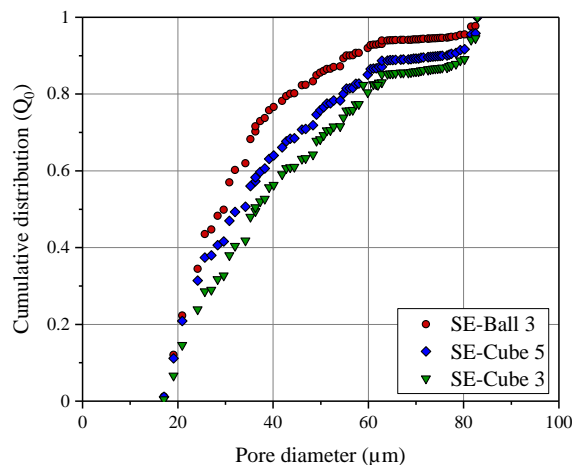


**Figure 3.11:** Cumulative size distribution of closed pores in an agglomerate, obtained by the closing operator with different structuring elements as well as by the complementing and labeling methods.

The average fraction of internal agglomerate pores which are not connected to the surface was found to be around 18.8%. Similar values (0.121–0.206) were reported for the internal porosity of cereal powder agglomerates by Hafsa et al. [2014]. No significant difference in closed porosity values was found between the individually investigated maltodextrin

agglomerates. This is because the internal porosity of agglomerates is mostly determined by the structure of the primary particles. The internal porosity of primary particles before agglomeration was found to be around 25%. This result shows that the porosity of primary particles is decreased by about 6% during agglomeration. This is because some of the internal pores are clogged by the maltodextrin substance that is dissolved in water. Moreover, in the course of the spray fluidized bed agglomeration process, the amorphous structure of maltodextrin absorbs a significant amount of water. Thus, the glass transition temperature of maltodextrin decreases strongly and the amorphous matrix undergoes a transition from the glassy to the rubbery state of relatively poor dimensional stability. Consequently, this may lead to collapse of some internal pores.

The 3D view of the spatial distribution of internal pores (Fig. 3.12) illustrates the true internal morphology of the agglomerate. Marked with blue color are smaller pores which were defined by the closing mathematical morphology operators, while larger pores which were distinguished with the complementing and labeling method are marked in orange. The size distribution of internal pores (Fig. 3.13) displays pore sizes ranging between 16 and 90  $\mu\text{m}$ . Moreover, in Fig. 3.12, the differences of pore size distributions after and before filling larger pores with the complementing and labeling methods are also shown. It should be noted that the resolution of the  $\mu\text{-CT}$  images was 2.2  $\mu\text{m}$ , therefore it was not feasible to detect pores smaller than 16  $\mu\text{m}$ . With the closing operator (SE-Ball 3) only pores below 50  $\mu\text{m}$  are identified, but after implementing the complementing and labeling methods larger pores are also distinguished. Fig. 3.13 is for one agglomerate with a large total number of pores and also sufficient number of pores in every size class. The same analysis was carried out for many other agglomerates with the same image analysis procedure. The results were very similar with several local minima and maxima, which are most probably related to the definition and evaluation of pores in the granulometry method. In order to reduce the analysis time, our methodology for evaluation the internal pores was also applied to packed beds of material. By this technique a significantly larger number of agglomerates or primary particles can be analyzed simultaneously. The internal porosity and the pore size range for different cases are compared in Table 3.2. The slightly higher values of the internal porosity obtained from the packed beds can be associated to the filling of some of the void space at the contact points during the procedure of filling the internal pores. Therefore, although with packed beds more particles are investigated in short time, the resulting porosity is by 4-5% more than the real value. One can also notice that the upper limit of the pore size range is higher in the packed bed than for single agglomerates or primary particles.

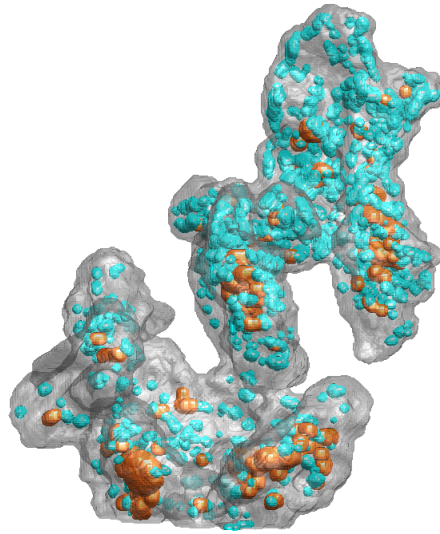


**Figure 3.12:** Spatial distribution of internal pores of an agglomerate.

**Table 3.2:** Calculated mean values of bulk and internal porosity of primary particles and agglomerates (single or in packed bed).

Object	Internal porosity (%)	Pores size ( $\mu\text{m}$ )	Pore median value ( $\mu\text{m}$ )	Bulk porosity, based on $V_{s,cp}$ (%)	Bulk porosity, based on $V_s$ (%)
Single agglomerates <sup>a</sup>	18.8 ( $\pm 1.5$ )	16-90	26.7 ( $\pm 2.9$ )	-	-
Single primary particles <sup>b</sup>	25 ( $\pm 1.2$ )	17-100	25.5	-	-
Packed bed of agglomerates <sup>c</sup>	24	17-115	25.4	78.9	82.7
Packed bed of primary particles <sup>c</sup>	29	17-143	24.5	67.6	75.5

<sup>a</sup>Presented values are from 5 agglomerates.

<sup>b</sup>Presented values are for 30 primary particles before agglomeration.

<sup>c</sup>Each packed bed contains at least 500 agglomerates and 3000 primary particles.

### 3.7.3 Open pore porosity

In addition to closed pores, open pores, which are connected to the surrounding air, are formed during the agglomeration process, when the primary particles stick together. Therefore, the process parameters used in the production of agglomerates are expected to have an effect on the open pore porosity.

The results for the open porosity obtained by the three different evaluation methods explained previously are plotted in Fig. 3.14. The comparison shows that open porosities obtained by the convex hull and the gyration radius methods are similar, whereas the open porosity obtained by the dilation method is much lower. For a complex structure with irregular shape, such as the maltodextrin agglomerate, the convex hull and the radius of gyration methods appear to be more suitable for determining the open porosity. In these

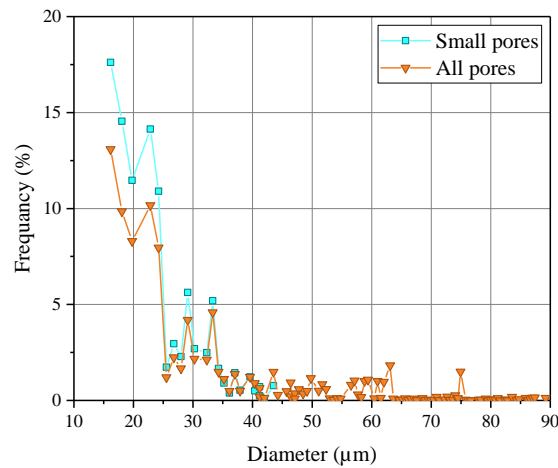


**Figure 3.13:** Frequency plot of the size of internal pores in an agglomerate obtained by applying only the closing operator (small pores) or the closing operator and, additionally, the complementing and labeling methods (all pores).

methods all the channels and open cavities can be considered in the total volume, whereas in the dilation method many open pores and channels may not be covered.

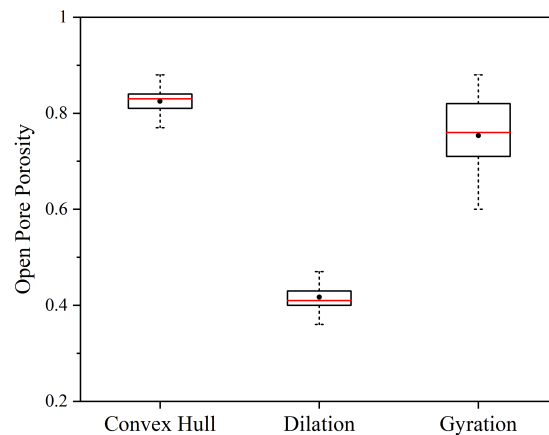


**Figure 3.14:** The open pore porosity of agglomerates, determined by three different methods.

The value of the open pore porosity for maltodextrin agglomerates calculated by the convex hull method is around 80%. This value is higher than the value obtained earlier for glass bead agglomerates (about 63%; Dadkhah, Peglow, and Tsotsas [2012]). This behavior is attributed to the properties of maltodextrin being an amorphous water-soluble substance. During agglomeration, the viscosity of the residual water increases due to the dissolved amorphous substance. Therefore, sticky and plasticized surfaces of maltodextrin particles lead to the creation of more irregularly shaped agglomerates with open structures in the spray fluidized bed (Fig. 3.15). Since glass beads are not soluble in water and experience no

glass transition during the process, the overall structure of glass bead agglomerates is more compact compared to maltodextrin agglomerates. Some agglomerates with instant properties investigated by Hoge Kamp and Pohl [2003] showed open porosity values between 0.7 and 0.8 at the upper end of the particle size range, i.e., for a particle diameter of around 1 mm. Therefore, our results for open porosity with the convex hull and the gyration radius methods agree well with the values reported in [Hoge Kamp and Pohl, 2003].

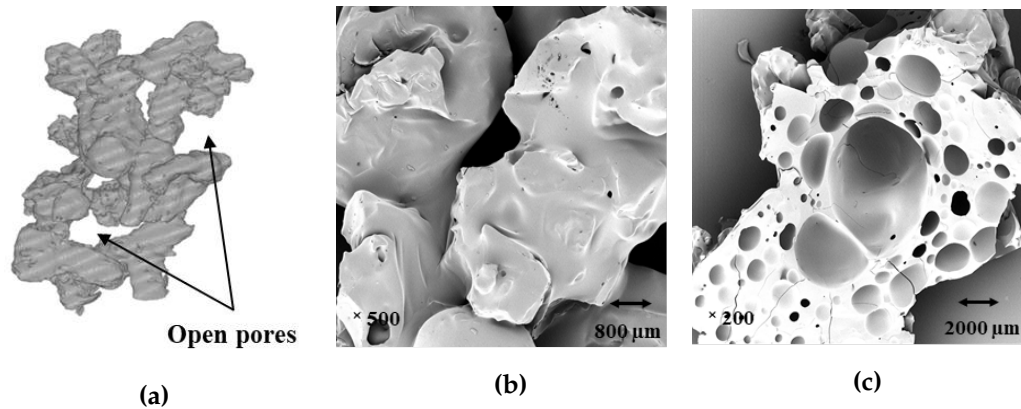


**Figure 3.15:** Maltodextrin agglomerate: (a) overall 3D view illustrating the irregular structure of the agglomerate with open pores (X-ray image), (b) plasticized surfaces after agglomeration (REM image), (c) cross sectional view showing the small and large internal pores (REM image).

#### 3.7.4 Bulk porosity

In Table 3.2, there is a difference between bulk porosity calculated by Eq. 3.11 and its counterpart, which is based on the same calculation but using the compact solid volume instead of the porous solid phase volume. The difference between these two bulk porosities is linked to the internal particle porosity.

The mean bulk porosity of the primary particles is 67.6% for a packed bed of primary particles whereas it increases to 78.9% for agglomerates. The morphology and size distribution of particles has a great influence on bulk porosity [Hoge Kamp and Pohl, 2003; Tsotsas, 2010]. Also, the mean value of sphericity of primary particles is larger than the agglomerate sphericity (see Table 3.3). Therefore, having a larger value of bulk porosity after agglomeration is reasonable. In another study by Zou and Yu [1996], the effect of particle/agglomerate shape on the bed packing has been investigated. The results therein show that the particle shape is crucial for the bed porosity, even if particles with similar sphericity are compared [Börjesson et al., 2014].

A lower bulk porosity (0.46-0.63) was reported in [Börjesson et al., 2014] for packed beds of agglomerated milk powder. It should be noted that in this work, the packing method was

different and the porosity was measured after 100 taps. The packed bed of particles was, thus, more compact and the porosity lower.

Due to the irregular structure of maltodextrin agglomerates, it is not easy to find a clear relationship between the agglomerate morphology and the bulk porosity. Similar to our agglomerates, most industrially available powders show a very complex morphology. Commonly they are agglomerated to a certain degree and thereby show a large polydispersity amongst the agglomerates. The shapes of the larger agglomerates also vary widely. This generates problems when linking the particle morphology to the bulk porosity for these types of complex samples [Börjesson et al., 2014]. Generally, compared to spheres, the larger, less spherical agglomerates are expected to yield beds with larger porosities due to disturbances in the close packing patterns.

### 3.7.5 Circularity and sphericity

The circularity of the agglomerates produced in the spray fluidized bed was measured by the Camsizer for more than 2000 agglomerates which lie in 25 size classes with a width of 0.08 mm each. This measurement was repeated for three different samples and the results are shown in Fig. 3.16. As can be seen, the circularity generally decreases with increasing particle size, and four main regions are recognizable. Region A refers to very small particles which could not be separated from the starting material of the process. These very fine particles seem to have very high values of circularity. However, such very high values may also be related to the image resolution since the perimeter acquisition is highly resolution-dependent for small particles [Zeidan, Jia, and Williams, 2007]. This would limit the ability to measure precisely the irregularity of the fine feed particles from the images acquired in the Camsizer and lead to an overestimation of the circularity according to Eq. 3.12. Once the size range of unagglomerated primary particles has been reached, a plateau in the graph is observed (region B) and the circularity remains rather constant until the size of small agglomerates (0.4 mm) has been attained. Then for intermediate agglomerates (region C), a clear trend of decreasing circularity with increasing agglomerate size is visible. In the agglomeration process, after a while these intermediate agglomerates stick together and secondary agglomeration occurs. Therefore, the circularity increases noticeably for agglomerates with a size of about 1 mm. After that, again by increasing the size of secondary agglomerates, the circularity decreases slightly (region D). Maltodextrin spray fluidized bed agglomeration in two stages is also reported in Avilés-Avilés, Dumoulin, and Turchiuli [2015].

The sphericity of the agglomerates was measured from the 3D reconstructed X-ray images (Fig. 3.17). The results are compared with the 2D Camsizer image results in Table 3.3. The mean sphericity value of agglomerates obtained from the X-ray images is 0.19. Similar values of sphericity (0.20–0.23) were reported by Hafsa et al. [2014] for laboratory grains

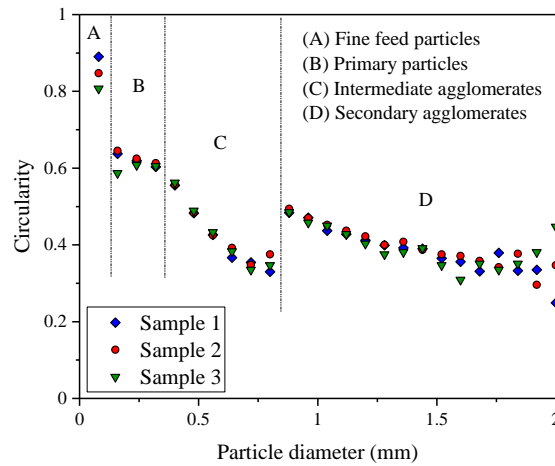


**Figure 3.16:** Circularity of particles after agglomeration measured by Cam-sizer.

produced under low shear conditions along with higher values (0.41-0.45) for industrial grains produced under high shear conditions. Moreover, even higher values of sphericity (0.78-0.87) were reported for granules produced in a twin screw extruder by Lee, Ingram, and Rowson [2013]. In the present work, the overall trend of agglomerate sphericity (Fig. 3.17) is similar to the trend of the circularity results (Fig. 3.16). The sphericity decreases with the agglomerate size, but remains significantly smaller than the circularity. The differences in these results may be due to image resolution. Circularity measurement in the Camsizer can probably not fully consider the surface irregularity of the agglomerates, so that the overall shape of the agglomerates appears to be more spherical than the real structure. Moreover, the analysis of single randomly-selected 2D projections clearly leads to incomplete results. It is not yet clear how many projections of an irregular agglomerate are needed in order to guarantee reliable characterization of its size and shape [Bagheri et al., 2014].

As illustrated in Fig. 3.17 and Table 3.3, an increase in sphericity is observed by applying the dilation morphological operator with a certain structuring element (SE-Ball 3) on the X-ray images. By implementing the dilation method, the small scale structural irregularity is diminished and the results become more compatible with the 2D Camsizer images. Increasing the size of the structuring element to SE-Ball 5 leads to a higher degree of filling of the pores and cavities, and to values closer to the circularity from the Camsizer. However, the 3D image analysis without manipulation may still be expected to more closely reflect the true physical shape of the agglomerates. Although the 2D image analysis yields a similar trend and requires less time and labor, the circularity values seem to be overestimated by about 50% compared to the sphericity values.

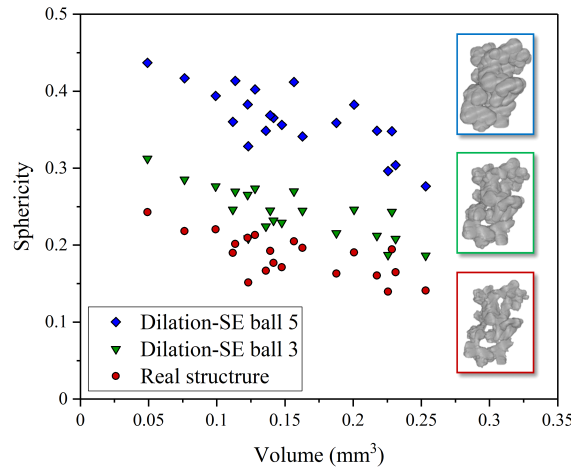


**Figure 3.17:** Sphericity of different agglomerates evaluated from 3D X-ray images with the real structure and with structures modified by the dilation method.

In general, 2D structural properties can be easily obtained from projected image analysis, however 3D parameters such as volume, surface area and sphericity need more sophisticated instruments (e.g. X-ray micro-computed tomography) that are more time consuming and in most cases cannot be applied to a large number of agglomerates. Many studies can be found in the literature that explore the possibility of obtaining 3D parameters from 1D and 2D variables [Asahina and Taylor, 2011; Blott and Pye, 2008; Taylor et al., 2006; Garboczi, Liu, and Taylor, 2012]. However, a comprehensive investigation on this subject is still missing, since most of the previous studies did not measure 3D parameters directly and/or their relationships with 1D and 2D properties were not analyzed in detail. It is also reported in [Bagheri et al., 2014] that out of all the correlations found for estimating 3D parameters from 1D and 2D variables, those related to sphericity have the highest average errors. It can be concluded that sphericity is a challenging parameter to be estimated from 2D variables.

**Table 3.3:** Values for sphericity and circularity of primary particles and agglomerates.

Particles/Method	Sphericity/Circularity
Primary particles/2D Camsizer images	0.60 ( $\pm 0.021$ )
Agglomerates/2D Camsizer images	0.37 ( $\pm 0.06$ )
Agglomerates/3D X-ray image <sup>a</sup>	0.19 ( $\pm 0.027$ )
Agglomerates/3D X-ray images + Dilation (SE-Ball 3) <sup>a</sup>	0.24 ( $\pm 0.033$ )
Agglomerates/3D X-ray images + Dilation (SE-Ball 5) <sup>a</sup>	0.36 ( $\pm 0.041$ )

<sup>a</sup>Presented values are means ( $\pm$ standard deviation) from 25 agglomerates.



### 3.7.6 Fractal dimension

The logarithmic representation of Eq. 3.14 for a series of agglomerates is depicted in Fig. 3.18. As can be seen, linearity is fulfilled with a good accuracy. Therefore, the maltodextrin agglomerates produced in fluidized bed can be considered as fractal-like, i.e., they satisfy Eq. 3.14 even though they are not self-similar over many length scales. The values of the fractal dimension and the prefactor are  $D_f = 1.81$  and  $K_g = 1.04$ , respectively. The low value obtained for the fractal dimension in this research illustrates the non-compact and fluffy structure of maltodextrin agglomerates. As reported by Eggersdorfer et al. [2012],  $D_f$  of around 1.8 or 1.9 corresponds to the open structure of aerosol fractal-like particles which were generated by diffusion-limited mechanism. During sintering, the value of  $D_f$  increases up to 3 when the particles become fully compacted. The same work illustrates the usefulness of fractal dimension in describing the change in structure for a process that starts with aggregates consisting of several hundreds of primary particles and ends up with just one large spherical object. The fractal dimension of glass bead agglomerates, which were produced in the same spray fluidized bed at similar process conditions, was reported to be in the range of 2.09-2.94 [Dadkhah and Tsotsas, 2014]. The smaller fractal dimension of maltodextrin agglomerates compared to the relatively compact glass bead agglomerates is an expected result. Also, in contrast to glass bead agglomerates, maltodextrin agglomerates consist of primary particles with different sizes, as shown in Fig. 3.8. It is pointed out in Eggersdorfer and Pratsinis [2012] and Eggersdorfer et al. [2012] that low fractal dimension of agglomerates can be attributed to primary particle polydispersity. Broadening the primary particle size distribution of the agglomerates decreases monotonically their  $D_f$ , and for a sufficiently broad distribution (standard deviation > 2.5) the  $D_f$  reaches about 1.5 regardless of the collision mechanism [Eggersdorfer and Pratsinis, 2012].

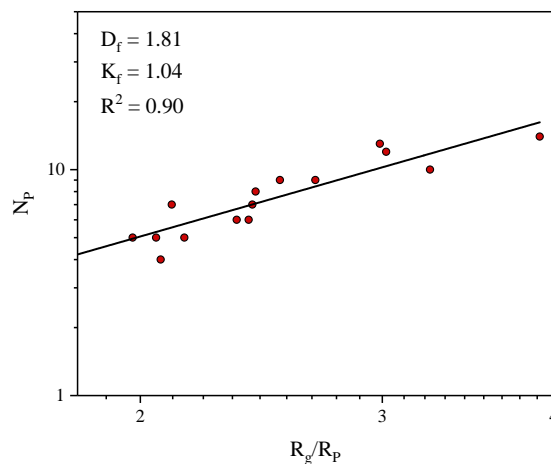


**Figure 3.18:** Number of primary particles per agglomerate vs. the normalized radius of gyration.

### 3.8 Influence of $\mu$ -CT parameters on structural characterization

In Sec. 2.3.2, the suitable scanning parameters were defined in order to have image with sufficient contrast. The most important factor in that section was voltage, current and exposure time. Here, the other scanning parameters were varied and their effect on the mentioned morphological characterizations was investigated. In this regard, for evaluating the quality of the 3D volume images, a few  $\mu$ -CT measurements were conducted on the same agglomerates changing image averaging, skipping values and rotational steps. The purpose of these measurements was to obtain optimal values of these parameters that provide precise characterization of the object in minimum possible time.

Image averaging identifies the number of individual images that are acquired per rotational angle. Higher value results in well reconstructed 3D images, however requires a lot of time. The skip parameter indicates how many individual images will be rejected before image reconstruction. The rotational step defines the number of projection angles during scanning and it is another important factor with significant influence on scanning time and image quality.

In this study, measurements T1 to T4 were carried out with averaging 3, skipping 1 and measurements R1 to R4 were performed with averaging 1 without image skipping. The rotational step was changed for each scanning while the other scanning parameters like voltage, current and exposure time were kept constant (as mentioned in Sec. 2.3.2). The scanning parameters and the average values of morphological characterization of agglomerates are summarized in Table 3.4. The volume, surface area and sphericity are not changed by varying the rotational step and the averaging number. Only at the largest rotational step  $0.9^\circ$ , due to the poor quality of images, the same value may not be obtained. Therefore, it can be concluded that surface area, volume and sphericity remained the same while measuring time decreased almost by half, with increasing rotation step from  $0.225^\circ$  to  $0.45^\circ$ .

Agglomerates placed on the sample holder remained at the same position and distance from the X-ray tube and detector for all measurements (as in Sec. 2.3.2). Consequently, voxel size during all measurements remained almost the same. The open pores porosity is reported based on the convex hull method. As shown in Table 3.4, the values of porosity are slightly changed by varying the scanning parameters. In general, the porosity is slightly higher with averaging number 3. This difference is due to the higher quality and contrast of the image with averaging 3 in which the pores and irregularity are acquired more precisely. The calculated value for porosity also decreases with increasing the rotation step. For scanning with averaging 3, a porosity value of 0.89 is obtained for the lowest rotational step of  $0.225^\circ$  (measurement T1) while this value for the maximum rotational step of  $0.9^\circ$  (measurement T4) is reported as 0.82. Almost similar trend is observed for scanning with averaging

**Table 3.4:** Results of morphological characterization at different scanning parameters.

Experiment	Averaging (-)	Skip (-)	Rotational step ( $^{\circ}$ )	Measurement time (hh:mm)	Surface area ( $m^2$ ) * $10^{-5}$	Volume ( $m^3$ ) * $10^{-10}$	Sphericity (-)	Open porosity CH (-)	$R_g$ ( $\mu m$ )	Internal porosity (-)
T1	3	1	0.225	2:50	1.2	3.5	0.11	0.89	620	0.30
T2	3	1	0.3	1:58	1.2	3.5	0.11	0.88	613	0.28
T3	3	1	0.45	1:10	1.2	3.6	0.12	0.86	601	0.23
T4	3	1	0.9	0:40	1.0	4.2	0.15	0.82	559	0.20
R1	1	0	0.225	1:30	1.2	3.5	0.11	0.87	610	0.27
R2	1	0	0.3	1:00	1.2	3.6	0.11	0.86	603	0.24
R3	1	0	0.45	0:40	1.2	3.6	0.11	0.84	590	0.21
R4	1	0	0.9	0:20	9.8	4.2	0.16	0.79	531	0.17

1 (measurements series R). When smaller rotational steps are applied, it means that higher number of projections is recorded for the object. Therefore, the final image is more rough and porous. On the other hand, with large rotational step the image is smoother and has less voids and irregularity for the same object. Consequently, higher values of the porosity are obtained from measurements with lower rotational step in comparison with the large rotational step. Fig. 3.19 shows the porosity and radius of gyration variations with changes in rotational steps and also with averaging 3 and 1.

For the same reason as in case of porosity changes, the radius of gyration decreases with increasing rotation step as well. By increasing the rotation step from  $0.225^{\circ}$  to  $0.9^{\circ}$ , the gyration radius decreases by almost 10% and 13% for measurements of series R and T, respectively. Among all the investigated parameters, the internal porosity is most sensitive regarding changes in the scanning parameters. This value decreases by almost 35% when the rotational step increases from  $0.225^{\circ}$  to  $0.9^{\circ}$ . Furthermore, the internal porosity decreases by around 12% when the number of averaged images changes from 3 to 1.

Fig. 3.20 represents the volume images of one agglomerate obtained at different rotational steps and averaging. It can be observed that the contrast of these images decreases from right to left; the images become more blurred with increasing rotational step and also with decreasing averaging number.

In general, it can be concluded that for the largest rotational step ( $0.9^{\circ}$ ) the 3D images are not good enough to provide precise characterization. For other variations and settings,

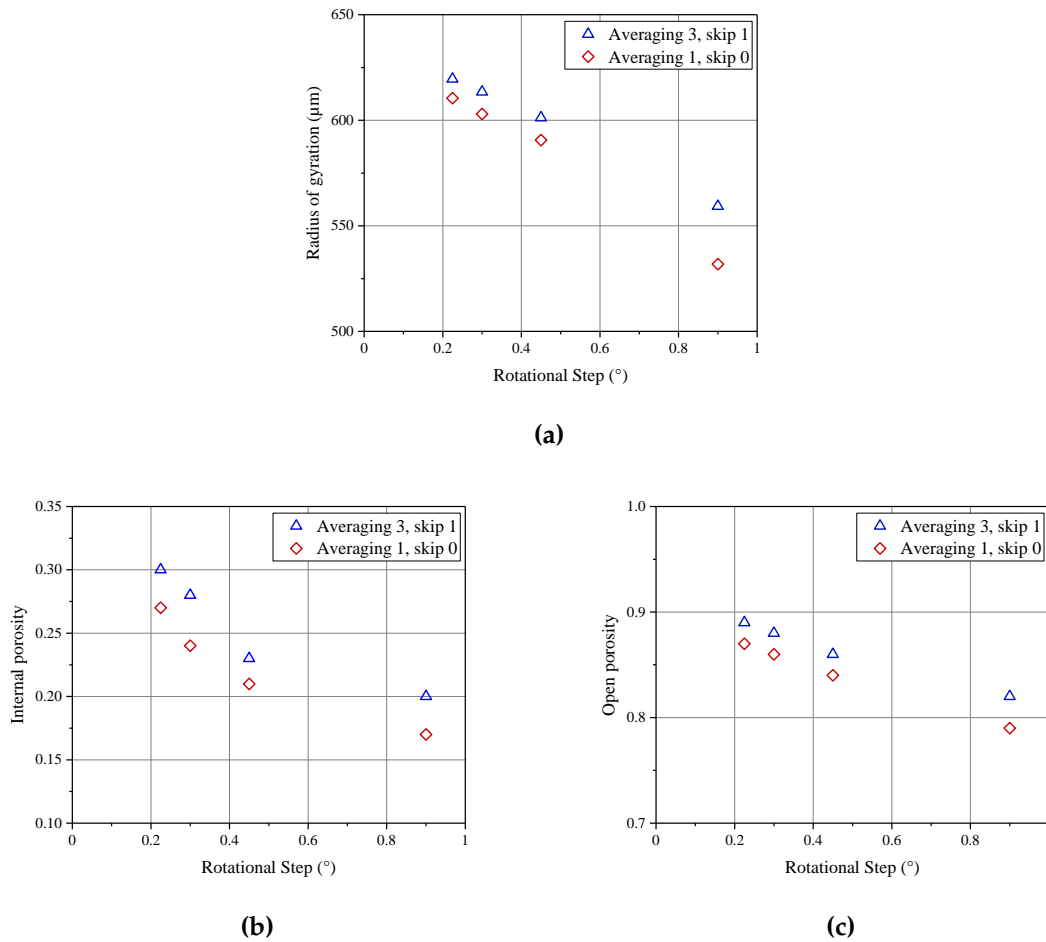


**Figure 3.19:** Impact of  $\mu$ -CT scanning parameters on radius of gyration (a), internal porosity (b) and open porosity (c) of agglomerates.

properties like surface area, volume and sphericity remain unchanged. The gyration radius and open pore porosity slightly decrease with increasing rotational step and decreasing averaging number. But for internal microstructural characterization, such as measurement of internal porosity, changing the rotational step or averaging number has noticeable influence on the result. Consequently, if more precise and accurate results relating to internal structure are required, averaging number 3 with low rotational steps like  $0.225^{\circ}$  or  $0.3^{\circ}$  are recommended. In this study, rotational step  $0.3^{\circ}$  was applied for scanning maltodextrin agglomerates (Exp. T2) due to the higher measurement time of rotational step  $0.225^{\circ}$ . If only properties like sphericity, volume and surface area are required, then rotational step of  $0.45^{\circ}$  with averaging number 1 can be a proper time-saving option.

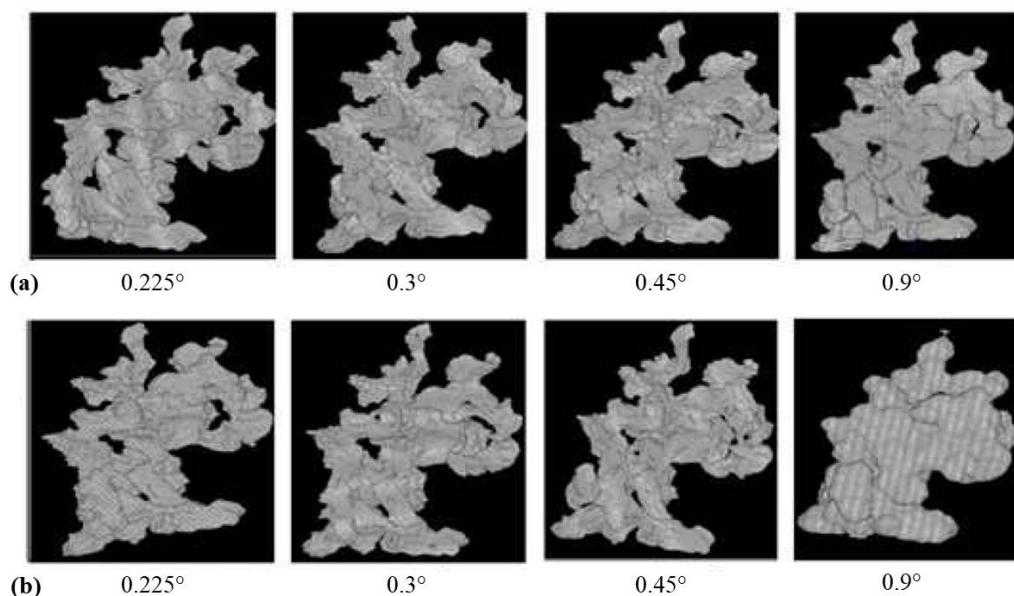


**Figure 3.20:** 3D volume images obtained at different rotational steps by X-ray  $\mu$ -CT: (a) averaging 3 and skip 1, (b) averaging 1 and skip 0.

### 3.9 General discussion

In this study, efforts have been undertaken to describe in detail the morphological features of maltodextrin agglomerates produced in a spray fluidized bed by X-ray 3D imaging. The question arises, which advantages this sophisticated characterization method would have in terms of its ability to provide morphological data that can be used for assessment, modeling or simulation of product properties when compared to conventional characterization techniques. This shall be briefly discussed in the present section, along with some remarks on structure–property relations and on merits and limitations of 3D imaging and conventional characterization methods.

An important application property of particulate products is their ability to withstand storage without loss of quality. During storage, hygroscopic products of biological origin that can undergo glass transition (such as maltodextrin) are in danger of sintering [Tsotsas and Mujumdar, 2011]. Moisture uptake from the atmosphere reduces significantly the glass transition temperature, so that the product may become rubbery at ambient conditions and sinter, which would completely destroy its whole user property profile. The most advanced models and scaling laws presently available for agglomerate sintering come from aerosol science and refer to flame produced nanoparticle aggregates [Eggersdorfer and Pratsinis, 2012; Eggersdorfer et al., 2012; Eggersdorfer et al., 2011]. The key morphological descriptor contained in them is, as already indicated, the fractal dimension of the agglomerates, which controls and expresses both, the rate of the sintering process and the change of morphology during this process. However, fractal dimension is not accessible by any conventional characterization method, so that 3D imaging and the method, which has been introduced in the

present work for identification of primary particles, are indispensable for future application of those models also to agglomerates made of bigger particles.

Apart from sintering and the activity of nanoparticles, the morphology of aerosol and colloidal agglomerates, expressed by fractal dimension and the radius of gyration, is known to affect their hydrodynamic properties, specifically their mobility diameter and, in consequence, scattering, suspension and precipitation behavior [Melas et al., 2014]. The precipitation behavior of agglomerates produced in a spray fluidized bed in water and their movement in the fluidizing air during the production process are expected to depend on morphology in a similar way. The former is essential for instant product properties (i.e. fast dissolution), the latter (via inter particle collision frequency) for the rate of the spray fluidized bed process. Since the key background morphological descriptors are not accessible by conventional methods, characterization by 3D imaging is, again, crucial for future exploration and better understanding of these effects.

Another important application property of agglomerated material is the mechanical strength of the agglomerates. Early simplistic models correlate strength with just the open porosity of agglomerates, stating that the mechanical strength increases with decreasing open pore porosity [Tsotsas and Mujumdar, 2011]. However, newer and better performing models make use of the number of primary particles in the agglomerate, the coordination number for the contacts of primary particles with each other, and the strength of contact bonds [Tsotsas and Mujumdar, 2011; Moreno-Atanasio and Ghadiri, 2006]. Alternatively, discrete simulation methods can be applied, namely the discrete element method (DEM) [Moreno-Atanasio and Ghadiri, 2006; Hassanpour, Antony, and Ghadiri, 2007]. It is very clear that neither advanced models for agglomerate strength nor DEM simulations can be conducted on the basis of conventional characterization methods, because such methods simply cannot provide the necessary information about morphology. In contrast, all necessary morphological data are provided by X-ray  $\mu$ -CT. To these belong the number of primary particles, grace to the method introduced for primary particle identification, and primary particle coordination number, which is easy to evaluate after the primary particles have been identified, though not explicitly discussed in this chapter. Moreover, X-ray  $\mu$ -CT provides full data for the morphology of individual agglomerates (including the bonds between primary particles), so that the DEM could be applied on real agglomerate structures (including respective statistics), instead of reconstructing numerically agglomerate structures from previously selected or identified morphological descriptors [Moreno-Atanasio and Ghadiri, 2006].

The list of structure dependent application properties can be arbitrarily expanded. For example, the bulk porosity of agglomerated powder is known to affect the stress and flow behavior in storage, handling and transportation equipment [Williams and Beck, 1995]. Properties such as rehydration, dissolution, and disintegration of agglomerates in water also depend on the presence and type of pores. For dry food agglomerates, the rehydration

ratio and moisture diffusivity increase with the bulk and open pore porosities as these pores allow for a quick penetration of water into the particle matrix and thus wetting phenomena occur faster [Farber, Tardos, and Michaels, 2003; Marabi and Saguy, 2004]. Good dispersion of agglomerated powder in the liquid is necessary in order to achieve an efficient reconstitution with limited lump formation, presupposing an efficient wetting of the porous bed, which relates to bed structure and void space [Marabi and Saguy, 2004; Schubert, 1993; Ortega-Rivas, 2009]. In all these cases the same arguments hold as previously discussed: Conventional characterization methods can give some hints about structure–property relationships, but they cannot provide the detailed information needed in order to apply or develop sophisticated and new methods for modeling or simulating such relationships.

To further point out the limitations of conventional characterization methods let us return to the example of agglomerate strength and assume that this can be unequivocally and uniquely correlated with porosity, as the earliest models for agglomerate strength imply. Even then, mercury porosimetry, i.e. the standard method for the determination of porosity and pore size distribution, would not provide reliable input data in case of instant agglomerates for two main reasons. Firstly, because of the shape and structure of maltodextrin (or similar) agglomerates, it is eventually impossible to determine the intrusion starting point [Farber, Tardos, and Michaels, 2003]. This is due to the fact that the pores and cavities are of similar size as the void space between agglomerate particles. Therefore, the results from mercury porosimetry are considered to be more representative of the bulk porosity, whereas  $\mu$ -CT can measure the porosity of any single agglomerate. Secondly, instant agglomerates are often docile and fragile, so that they can be compacted or damaged during mercury porosimetry. Moreover, mercury porosimetry cannot detect closed pores and uses a model in order to derive structural information from the primary measurement result, whereas X-ray  $\mu$ -CT relies directly on the distribution of different phases in space. The limitations of mercury porosimetry have been quantitatively pointed out in [Rahmanian et al., 2009].

Concerning the size of agglomerates (in its traditional definitions) conventional measuring techniques are well established. However, particle shape is also important for the properties of particulate products, for example bed porosity [Börjesson et al., 2014], and enormously variable in food powders and agglomerates, which range from extreme irregularity (grinded materials such as spices and sugar) to approximate sphericity (starch and dried yeast) or well-defined crystal shapes (granulated sugar and salt) [Barbosa-Cánovas et al., 2005]. 2D image analysis gives only partial information about the particle shape, whereas 3D image analysis allows for the measurement of true particle characteristics [Merkus, 2009]. Hence, 3D shape data can be used to discuss the accuracy of other methods. In this study, the shape (and also the size) of particles was investigated in both, two and three dimensions with the Camsizer and X-ray  $\mu$ -CT, respectively, and the results were compared. On these grounds, two lines of future development are seen in this field: To develop correlations between 3D shape results (which require time-consuming X-ray  $\mu$ -CT to be retrieved)

and 2D shape results (which are easier and faster to obtain); to better delineate the adequacy and applicability of 2D or 3D shape results for computation of application properties.

Despite its discussed known and potential advantages, X-ray  $\mu$ -CT can only be conducted on a limited number of agglomerates, a lot less than the thousands of particles analyzed by traditional size measurement techniques or the number of agglomerates usually analyzed by mercury porosimetry. However, it is not the number of investigated agglomerates that counts in terms of statistical significance in some cases, but the much higher number of other and smaller structural elements, for example the number of primary particles or closed pores for the respective size distributions (Figs. 3.9 and 3.13). In the case of internal porosity and sphericity of single agglomerates measured by the  $\mu$ -CT, small standard deviations were obtained, with values of  $\pm 1.5\%$  and  $\pm 0.027$ , respectively (see Tables 3.2 and 3.3). The internal porosity and circularity values obtained for the primary particles had standard deviations of merely  $\pm 1.2\%$  and  $\pm 0.021$ , respectively. These small standard deviations indicate that the amount of samples analyzed here represents the properties of the whole population of particles quite reliably. Concerning the reliability in the determination of fractal properties, Dadkhah and Tsotsas [2014] asked the question by how much the fractal dimension originally determined for about 28 agglomerates would change by considering a significantly smaller number of agglomerates. To answer this question, they randomly picked half of the agglomerates from the original sample and determined again the value of  $D_f$ . Forty realizations of this procedure resulted in a small standard deviation and in a mean value very close to the value of  $D_f$  previously determined for the original, large sample.



## Chapter 4

# Spatial morphology of agglomerates: Real structure evaluation vs. spherical primary particle model

*This chapter is a modified version of "Spatial morphology of maltodextrin agglomerates from X-ray microtomographic data: Real structure evaluation vs. spherical primary particle model, Powder Technology (2018)".*

### 4.1 Introduction

The shape of a primary particles affects the agglomeration mechanisms and the properties of the resulting agglomerates [Cuq et al., 2013]. Lack of consideration of these factors in models may lead to inaccurate results. Most of the previous research studies performed in this regard deal with simplified models of agglomerates which are cost and time effective but not very accurate. A simplified model was applied by Dadkhah, Peglow, and Tsotsas [2012] for agglomerates in which the primary particles did not deviate too much from the spherical shape. For calculating the fractal dimension of diesel soot agglomerates, Lapuerta, Ballesteros, and Martos [2006] also considered primary particles to be spherical; sintering or flattening effects were not taken into account. Oh and Sorensen [1997] showed that, although the effect of sintering is very relevant for the prefactor, it is small for the fractal dimension.

However most agglomerates of powder like maltodextrin have irregularly shaped primary particles and the material undergoes glass transition and deforms during the agglomeration process. Therefore, when analyzing the spatial morphology of maltodextrin agglomerates it is very important to consider the features of the real structure. This study focuses on the morphological characterization of maltodextrin agglomerates with the help of two different study models: the simplified spherical primary particle model (SPPM) and the

real structure model (RSM), which considers the irregularities of primary particles. Based on these models various three-dimensional morphological descriptors are developed, such as coordination number, coordination angle distribution, radial distribution of primary particles and open pores porosity. The differences in morphological descriptors between the two models are unveiled. In this way it becomes visible, for which kind of characterization the simplified model can be applied. Different input parameters are used for each model, the input for the SPPM originating from the real structure by considering the primary particles to be equivalent spheres. While the only input for the real structure model (RSM) is a stack of 2D binarized images of agglomerate specimens obtained from X-ray micro tomographic scanning.

## 4.2 Study models

Two different models are employed in order to understand the morphological structure of agglomerates in both simplified and comprehensive manner. The objective behind using two different study models is to check the precision of results obtained through simplified models and to quantify the variations when compared with a detailed model. For this purpose, a detail oriented model named as "real structure model" (RSM) and a simplified model termed as "spherical primary particle model" (SPPM) are used in the present study (see Fig. 4.1).

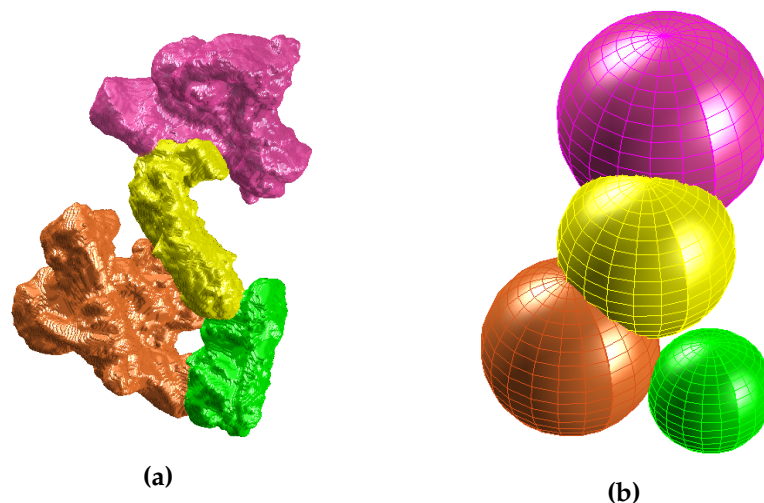


**Figure 4.1:** Volume images of an agglomerate comprised of four particles: (a) reconstructed by the real structure model and (b) the spherical primary particle model.

#### 4.2.1 Real structure model (RSM)

The RSM is very close to the actual structure of maltodextrin agglomerates gained by X-ray micro tomography. In this model, the scanned agglomerate is processed, and 2D binarized images are extracted in a particular spatial direction. These 2D binary images are then used as the sole input for further analysis of the internal structure of agglomerates. Purpose-based specific algorithms are developed in order to evaluate 3D morphological descriptors of the agglomerate. The computational cost and effort required for this model is relatively high as compared to the SPPM, but the results obtained are more accurate. Fig. 4.1a visualizes four primary particles separated from the real structure of an agglomerate. The primary particles of all agglomerates studied with this model are separated individually by means of the preflooded watershed method, which has been discussed thoroughly in Sec. 3.2. Then, each primary particle is sliced in a specific spatial direction to obtain a stack of 2D binarized images.

#### 4.2.2 Spherical primary particle model (SPPM)

Agglomerates reconstructed according to the SPPM, as seen in Fig. 4.1b, are considered as an approximation to the real structure. The basis of this model is that each primary particle is represented by an equivalent sphere with the same geometric center as the real primary particle. The diameter of the sphere in this model was set in a way that resulted in the same volume as for the real primary particle in all morphological characterizations except of the coordination number and the coordination angle distributions. Alternatively, the diameter of the sphere may be set equal to the mean diameter of the respective primary particle. This diameter was defined as the mean value of primary particle diameters obtained in 13 discrete directions on the cuboidal lattice (three coordinate directions, six face diagonals and four space diagonals). Since these values are somewhat larger than diameters based on equal volume, for calculating the coordination number and the coordination angle distributions the mean diameter was used in the approximate model (SPPM).

### 4.3 Methodology and evaluation of 3D morphological descriptors

#### 4.3.1 Coordination number

Coordination number (CN) of a primary particle in an agglomerate is the total number of neighboring contacts of that particle with its surrounding particles. It expresses the connectivity of primary particles in the aggregate, which mainly depends upon the properties of

the aggregate material and on the techniques utilized to produce the aggregate [Wang et al., 2012].

### Coordination number for SPPM

The coordination number of primary particles for the approximate model is calculated by counting contacts between neighboring spherical particles. One contact is counted if the following condition is satisfied:

$$\sqrt{(X_i - X_j)^2 + (Y_i - Y_j)^2 + (Z_i - Z_j)^2} \leq |R_i + R_j|. \quad (4.1)$$

Here,  $X$ ,  $Y$  and  $Z$  are the center coordinates of each primary particle and  $R$  is the radius of each spherical particle;  $i$  denotes the primary particle under consideration and  $j$  is one of the surrounding primary particles of the agglomerate.

This relation was used by Dadkhah, Peglow, and Tsotsas [2012] for nearly monodispersed and spherical primary particles. In the present study, an algorithm has been developed based on the above mentioned relation for polydispersed primary particles of maltodextrin agglomerates. The main inputs for the algorithm are basically two matrices: one represents the center coordinates of primary particles of the agglomerate and the other one accounts for the radius of each spherical primary particle. These two matrices are obtained from the volume images of the scanned agglomerate after separating the primary particles. The algorithm computes the center-center distance between considered primary particle  $i$  and neighboring primary particles  $j$  along with their corresponding sum of radii while checking the condition stated in Eq. 4.1. If the condition is satisfied, then the counter of the coordination number variable will be increased by one and the algorithm will move forward to the next surrounding particle in the matrix, till all the surrounding particles in the agglomerate have been checked. Then another primary particle is chosen from the matrix and the same procedure is repeated. In the end a frequency plot of coordination number is generated along with the values of mean coordination number (MCN), standard deviation  $S_d$  and skewness  $S_k$ .

### Coordination number for RSM

Determination of coordination number for the real structure model is a challenging task, because the previous relation (Eq. 4.1) based on the sum of radii is invalid for the real structure due to irregular shape of primary particles. The concept behind the detection of contact between two primary particles of a real agglomerate is to find mutual contact points between particles. If two primary particles are in contact, then they must have at

least one common coordinate point. As can be seen in Fig. 4.2, the two particles have a contact region, in which they have mutual coordinate points. Hence, the logic behind the algorithm developed for this task is to compute the 3D coordinate points of each primary particle and then compare it with the coordinate points of neighboring primary particles. If they have at least one common coordinate point, then one contact is counted.

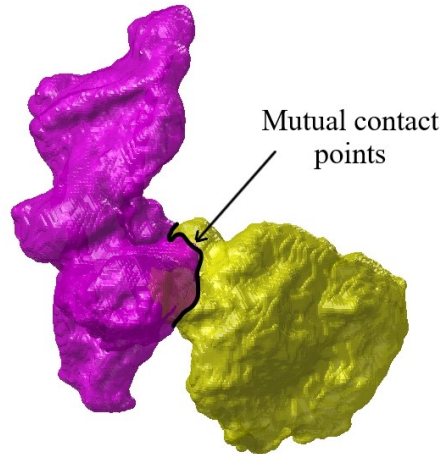


**Figure 4.2:** Mutual contact region representing common coordinate points.

For this purpose, after separating the primary particles, corresponding stacks of 2D binarized images are generated. Then, the 3D matrix of these binary values for each primary particle is created based on these 2D slices. Since coordination number is the parameter related to the boundary of the primary particle, only the boundary coordinates are extracted from the 3D matrix. Computational time can thus be saved. The boundary vertices can be accessed through the isosurface function (see Fig. 4.3). With the help of the vertices data the 3D coordinate points for the complete structure of the primary particle are accessible. This data is generated for the primary particles of each agglomerate and stored in a separate matrix. Based on these matrices, 3D coordinates of each particle are checked with its neighboring primary particles for mutual contact points. Finally a frequency plot of coordination number is generated along with MCN,  $S_d$  and  $S_k$ .

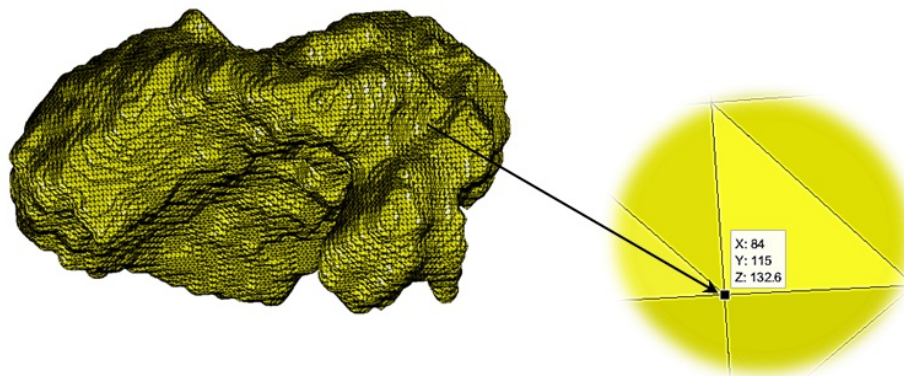


**Figure 4.3:** Visualization of 3D coordinate points of the boundary surface of a primary particle.

### 4.3.2 Coordination angle for SPPM and RSM

Most of the existing literature has focused on scalar parameters, but for detailed understanding of the morphology of agglomerates vector parameters, e. g. the coordination angle, are required. Coordination angle of a primary particle is the angle between the vectors connecting the centers of two contacting neighboring particles to the center of that specific primary particle. It is the parameter through which the overall stability and final shape of the agglomerate morphology can be explained, and also the ability of agglomerate to condense vapors [Brasil et al., 2001].

The coordination angle ( $\theta$ ) is calculated with the help of the scalar product of vectors (cosine law), which is also known as angle between the triplets. The input for both models is their respective coordination numbers of primary particles. For both models, the number of vectors is calculated according to the coordination number of the primary particle in the respective model. The number of vectors has the same count as the CN. Primary particles with CN = 1 have a coordination angle of  $180^\circ$  and are not considered in this task. The coordination angles of all primary particles of an agglomerate result in the distribution of coordination angle.

For illustration (Fig. 4.4a) consider A as a primary particle being in contact with neighboring primary particles B and C. The coordination angle is computed as,

$$\theta_A = \cos^{-1} \frac{\vec{CA} \cdot \vec{BA}}{|\vec{CA}| |\vec{BA}|}, \quad (4.2)$$

where  $\vec{CA}$  and  $\vec{BA}$  are the computed vectors and  $|\vec{CA}|$  and  $|\vec{BA}|$  are their respective magnitudes. In the second case of three neighboring primary particles (Fig. 4.4b) there are three different coordination angles for primary particle A. In the same manner increasing the number of contacting particles increases the number of coordination angles.

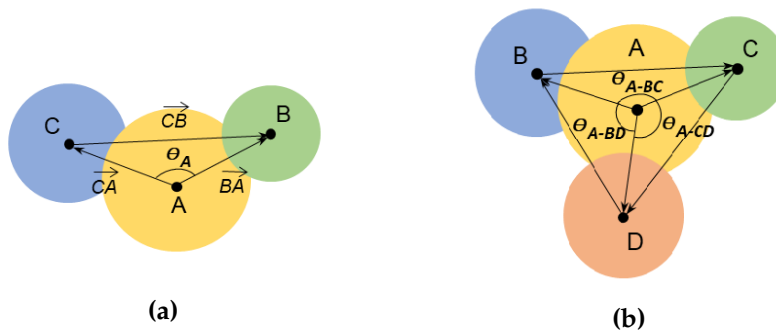


**Figure 4.4:** Illustration of coordination angle for (a) two and (b) three contacting neighbors.

### 4.3.3 Radial distribution of primary particles

The radial distribution of the center coordinates of primary particles describes how the positioning and assembly of primary particles takes place during the agglomeration process to form different shapes and morphological structures of the agglomerates. This 3D morphological descriptor enables to analyze the spatial variation of particle centers and is a measure of packing efficiency of the agglomerate. To measure the placement probability of primary particles at different radial positions, the radial distribution of particles is evaluated by two different approaches: The first approach leads to the cumulative radial distribution of particles, whereas the second one results in the particle density function. Both of these methods are based on the center coordinates of primary particles. Therefore, the results are identical for both the SPPM and RSM.

#### Cumulative radial distribution of particles

The cumulative radial distribution (CRD) method uses a sphere  $S$ , the center of which is the geometric center of the agglomerate. The sphere with radius  $R$  is incremented by  $\Delta R$  after each step. In every step the number of particle centers included in the sphere  $S$  is calculated until all the particle centers have been counted (see Fig. 4.5).

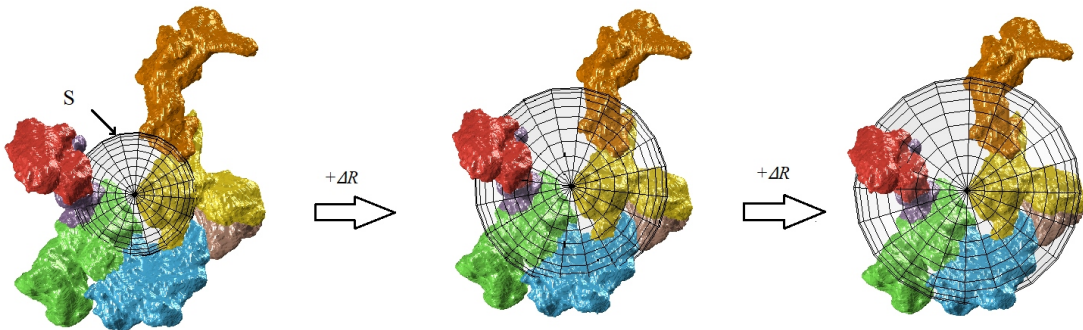


**Figure 4.5:** Visualization of cumulative radial distribution method for an agglomerate comprising of 7 primary particles.

This method has been implemented by Lagarrigue et al. [2010] for agglomerates generated numerically to describe how closely center points are packed. The starting step for the algorithm is the center coordinates of the primary particles. The geometric center (centroid) of the agglomerate is then evaluated. Since the sphere  $S$  is drawn from the centroid of the agglomerate, the distance between each primary particle center and the centroid is calculated and sorted in ascending order. The initial value of the radius of sphere  $S$  is taken as half of the smallest primary particle radius and it is incremented with the same value until all the distances (particle centers) have been covered. Finally, based on the number of primary particles identified in each step, a cumulative radial distribution of primary particles

can be plotted. The geometric center and center coordinates of the primary particles are identical for the SPPM and the RSM. Therefore, the radial distribution of primary particles is jointly presented for both models.

### Particle density function

The density function of primary particle centers results from a modified form of the procedure applied previously for the cumulative radial distribution. This particle density function (PDF) is an indicator of compactness of the internal structure of an agglomerate. Conceptually the two different procedures are conveying the same information about the placement characteristics of primary particles, but they provide good means to visualize the results in different ways. The PDF method uses two spheres, the center of which is the center of the primary particle closest to the geometric center of the agglomerate. The spheres have radii  $R$  and  $R+\Delta R$ , and both grow with the same increment of  $\Delta R$ , the number of primary particles located in the free volume between the two spheres being counted for each calculation step.

As graphically shown in Fig. 4.6, the free volume space between the solid and the transparent sphere is the region where primary particle centers are counted in every step in order to estimate the PDF. This method has been discussed by Dadkhah and Tsotsas [2014] for the calculation of particle density function of monodispersed primary particles of alumina and glass beads.

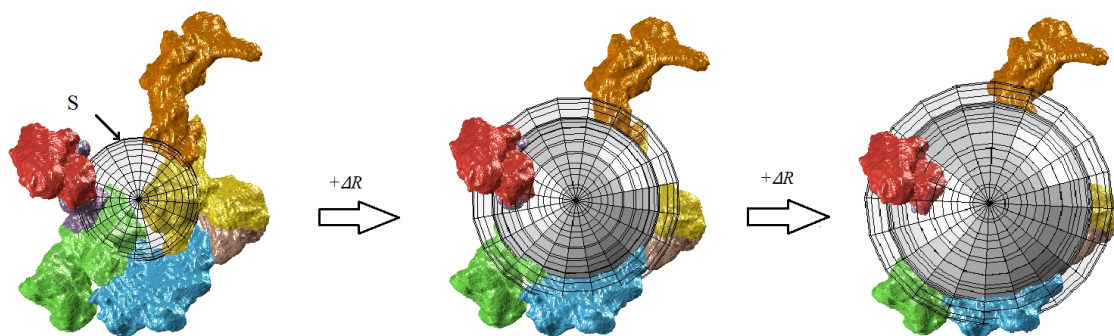


**Figure 4.6:** Visualization of particle density method for an agglomerate comprising of 7 primary particles.

The starting point for PDF determination is the same centroid coordinates as for the previous case. Distances between primary particle centers and the centroid are then calculated to determine the closest primary particle to the centroid of the agglomerate. Then the distances between the center of this closest primary particle and the remaining particle centers are estimated. After that, these distances are sorted in ascending order and compared to the space interval between the two incrementally growing spheres. The starting value of  $R$  is set to zero while the increment  $\Delta R$  is taken as half of the smallest primary particle radius.



The sorted distances of primary particle centers are checked against the range of  $R$  to  $R+\Delta R$  and particle centers present in this range are counted in every step. In the end, the particle density function showing the trend of primary particle concentration with respect to radial coordinate of the agglomerate is plotted.

#### 4.3.4 Open pore porosity for SPPM and RSM

Calculation of the open porosity has been discussed in Sec. 3.4.3. Eq. 3.7 for estimating the open porosity can be also written based on the volume of primary particles:

$$\varepsilon_{op} = 1 - \frac{1}{V_{agg}} \sum_{i=1}^{N_p} V_i, \quad (4.3)$$

where  $V_{agg}$  is the total volume of the agglomerate including open pores and  $V_i$  is the solid volume of primary particles including internal pores. In Sec. 3.4.3, the total volume  $V_{agg}$  of maltodextrin agglomerates has been calculated by applying three different approaches of dilation, convex hull and radius of gyration. It has been concluded that open pore porosities obtained from convex hull and radius of gyration methods are more suitable for agglomerates with such irregular and open structure. Therefore, these two methods are selected for calculation of open porosity for SPPM and RSM.

##### Porosity by convex hull

The convex hull is the smallest convex region that contains a certain object. For SPPM convex hull volume is calculated based on the center coordinates and radii of primary particles. The primary particles of spherical model agglomerate are drawn with respect to their radii and split into 30 meshes which provide a sufficient degree of smoothness and adequately gridded data. After that, points on the surface of each sphere are exported in a separate matrix as an input for convex hull calculation. For real structure model, as it is done for primary particles in Sec. 4.3.1, the boundary vertices of an agglomerate should be exported. Then, the convex hull is generated for a set of vertices based on their coordinates in 3D space. The volume bounded by this convex hull region is then computed. The volume of convex hull obtained for each of the two models is regarded as the total volume of agglomerate  $V_{agg}$  and used along with the volume of primary particles  $V_i$  in Eq. 4.3 to determine the value of open pores porosity. Fig. 4.7a shows the smallest convex region enclosing a SPPM agglomerate while individual primary particles of this agglomerate can be seen in Fig. 4.7b.

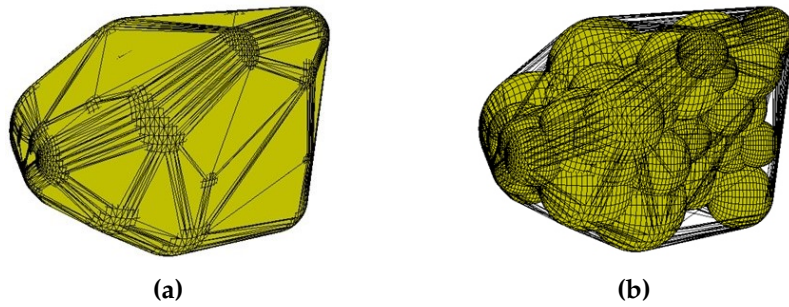


**Figure 4.7:** Convex hull region of an agglomerate comprising of 55 primary particles.

### Porosity by radius of gyration

The total volume of agglomerate  $V_{agg}$  can be calculated based on the radius of gyration for both the SPPM and the RSM. For an object consisting of separated elements or primary particles the radius of gyration can be calculated based on Eq. 3.3.

For the SPPM, the center coordinates and the volume of each primary particle were used to calculate the radius of gyration. For the real structure it was calculated based on the voxel data obtained from the X-ray images of the agglomerate. By considering each voxel as a separated element and having the number of voxels and their position vectors, the radius of gyration was obtained. The values of radius of gyration are then used to obtain the equivalent radius,  $R_e = \sqrt{\frac{5}{3}}R_g$ , and the total volume of agglomerate,  $V_{agg} = \frac{4\pi}{3}R_e^3$ . Fig. 4.8 shows exemplarily the equivalent sphere for radius  $R_e$  (total volume) for one of the investigated agglomerates.

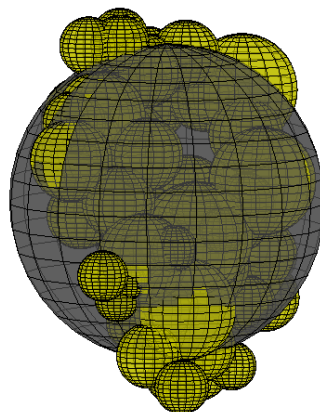


**Figure 4.8:** Equivalent sphere (gray color) obtained by radius gyration.

## 4.4 Results and discussion

The morphological descriptors introduced in Sec. 4.3 have been calculated for a series of 21 agglomerates which are categorized on the basis of the number of primary particles: Small for  $N_p < 18$ , medium for  $18 < N_p < 25$  and large for  $N_p \geq 25$  with  $N_p = 55$  for the largest agglomerate of the series. All the selected agglomerates have been produced during the same experiment with the spray fluidized bed (Trial C, Table 2.2).

### 4.4.1 Coordination number of primary particles

The overall coordination number distribution and the mean coordination number of an agglomerate can appreciably affect the agglomerate physical properties including mechanical strength and effective thermal conductivity [Dadkhah and Tsotsas, 2014]. In this section, coordination number results for primary particles are discussed for both the SPPM and the RSM in order to validate the application of the simplified SPPM in coordination number calculations. The comparison of frequency distributions of CN resulting from the two models is shown in Figs. 4.9 and 4.10 for selected 3 medium and 3 large size agglomerates, respectively. Bar charts for both models are also shown for the largest agglomerate ( $N_p = 55$ ) in Fig. 4.11. It can be seen that the range of coordination numbers is slightly smaller and the frequency of primary particles having three or four contacting neighboring particles is higher in the RSM. This trend is not very significant for medium size agglomerates having  $18 < N_p < 25$  but it is seen prominently in large size agglomerates, specifically for  $N_p = 42$  and for the largest agglomerate of the series with  $N_p = 55$ . The maximum frequency of coordination number attained in the case of spherical and real agglomerate model is 12 and 13, respectively.

From the results it is found that CN for the two models is different and only one coordination number distribution is the same, namely for the smallest agglomerate of the series having  $N_p = 7$ . It can be seen in Fig. 4.12 that contact points of primary particles are not identical for the RSM and the SPPM. The difference in CN values for the two models is due to irregularity in the structure of primary particles. By assuming the irregular particle as sphere, some contact points were not resolved and some new contacts might have been generated. For that reason, the calculation of CN from the real structure model is essential for maltodextrin agglomerates due to complex structure of primary particles. The mean coordination number for the SPPM is relatively constant at around  $MCN = 3.5$ , whereas for the RSM it is around  $MCN = 3.0$  with few exceptions for very small size agglomerates ( $N_p < 9$ ). The standard deviation values for the SPPM and the RSM are relatively constant at around  $S_d = 2$  and  $S_d = 1.5$ , respectively, indicating coordination numbers of the RSM closer to the MCN. The bar graphs of the RSM are more symmetrical and closer to the normal

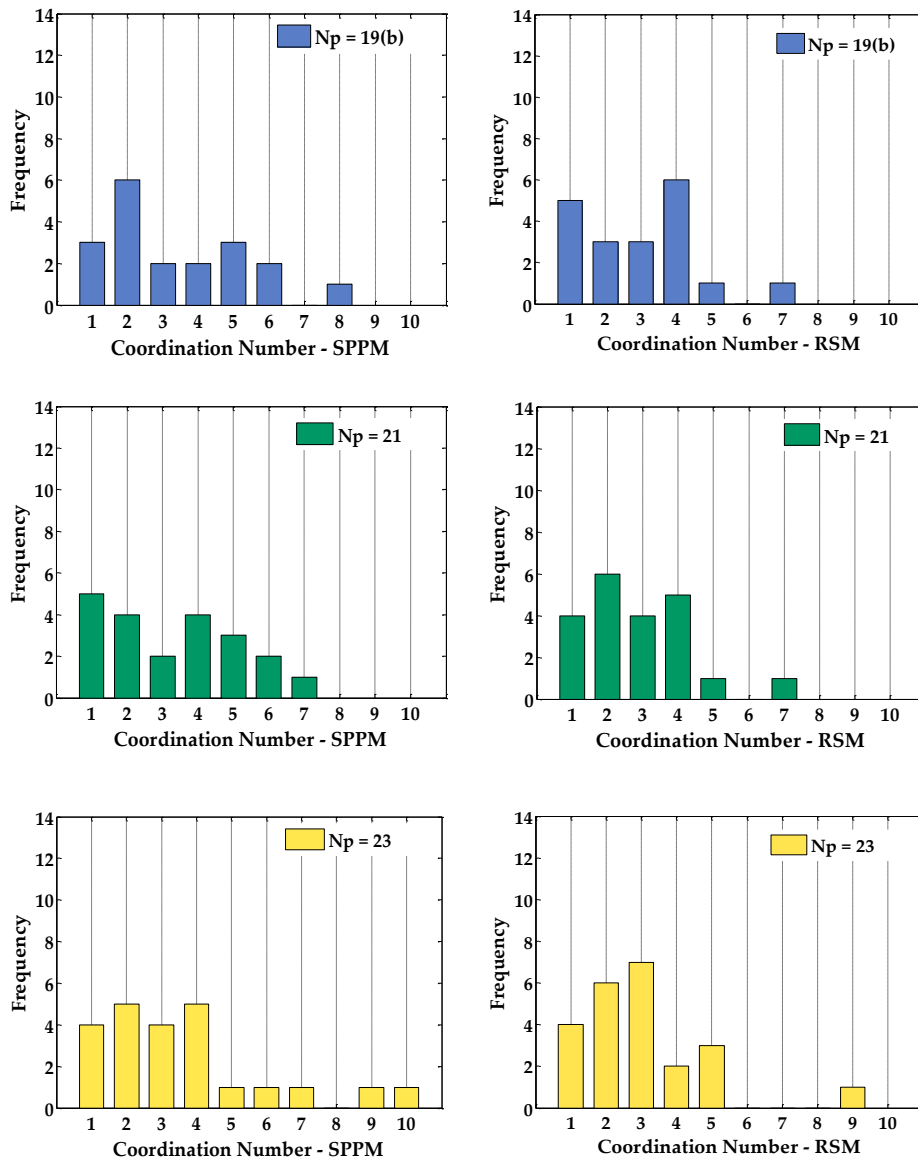
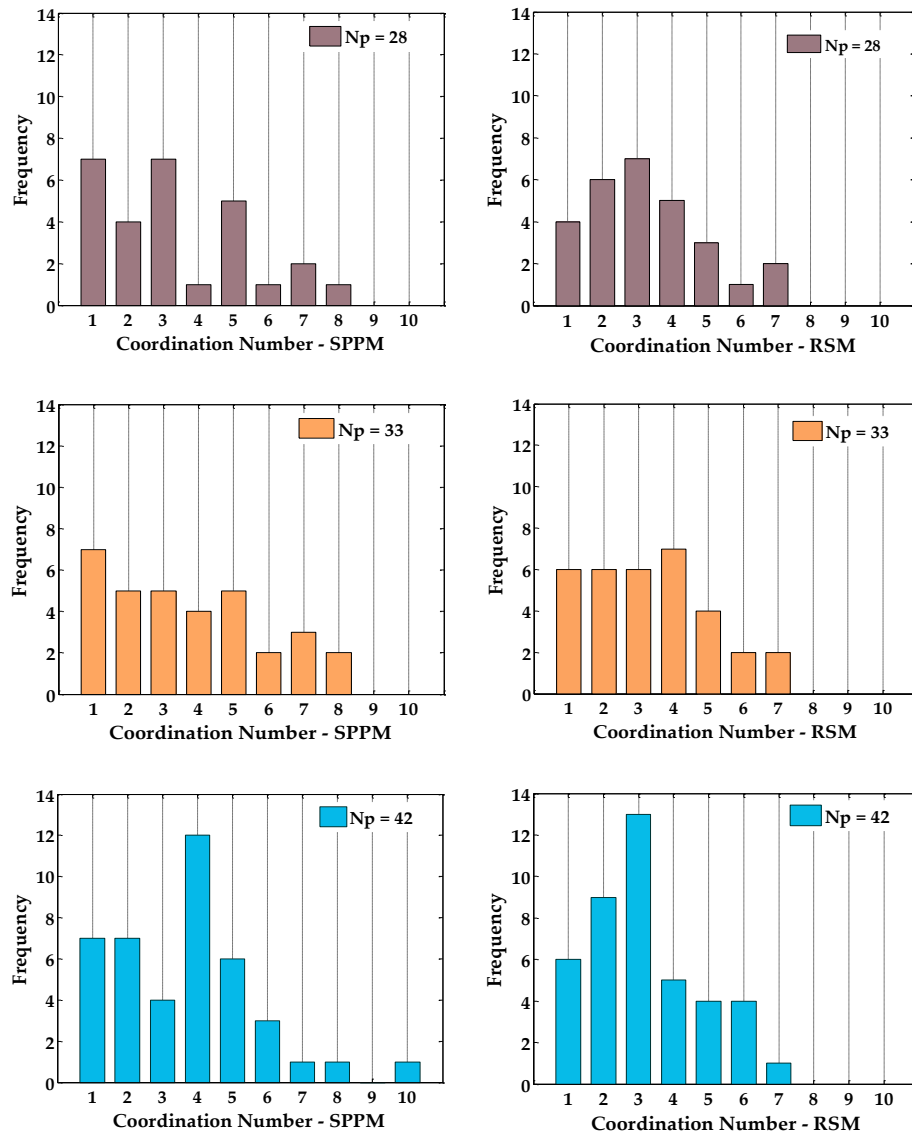


Figure 4.9: Frequency distribution of coordination number; comparison between SPPM and RSM for medium size agglomerates.

distribution as compared to those of the SPPM. This is also evident from the low standard deviation of the RSM (see Appendix A, Table A.1).

The mean coordination number values obtained in this study are in coarse agreement with the result of  $MCN = 4.0$  obtained by Dadkhah and Tsotsas [2014]. The study performed by Dadkhah was on alumina and glass beads using the same top spray fluidized bed granulator. However, the primary particles in that study were monodispersed and agglomerate sizes were much bigger, with  $N_p$  in the range of 17 to 320. This comparison supports the conclusion drawn by Brasil et al. [2001] regarding the fact that coordination number distribution does not significantly depend upon the number of primary particles. However, the comparatively lower value of  $MCN$  obtained in this study may be explained by the



**Figure 4.10:** Frequency distribution of coordination number; comparison between SPPM and RSM for large size agglomerates.

plasticized and sticky nature of maltodextrin particles during the agglomeration process. Undergoing glass transition seems to have resulted in scattered structure of agglomerates with less neighboring primary particles (lower MCN). The value of fractal dimension and prefactor reported in Sec. 3.7.6 for maltodextrin agglomerates produced by using the same fluidized bed under almost identical process conditions was about 1.8 and 1.04, respectively [Pashminehazar, Kharaghani, and Tsotsas, 2016]. This low value of 3D fractal dimension and prefactor delineate the open and fluffy structure of the maltodextrin agglomerates.

Other research studies available for comparison of coordination number lack experimental data. Most of the literature is based on the study of simulated agglomerate structures. The research work carried out by Brasil et al. [2001] dealt with fractal-like aggregates produced by different aggregation mechanisms. When the overlapping (similar as in our

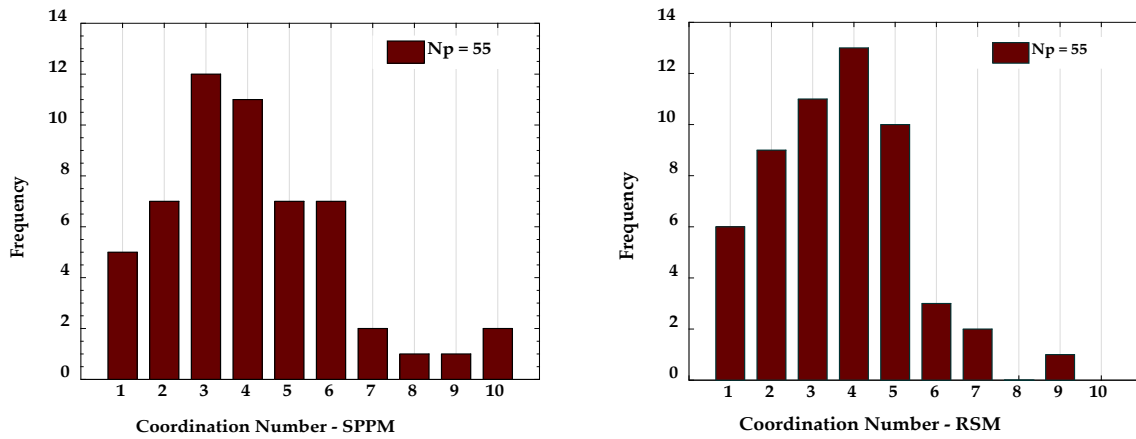


Figure 4.11: Frequency distribution of coordination number; comparison between SPPM and RSM for the largest agglomerate of the series.

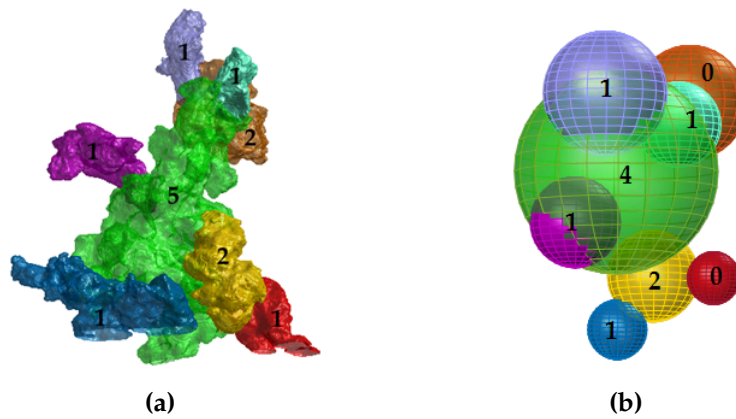
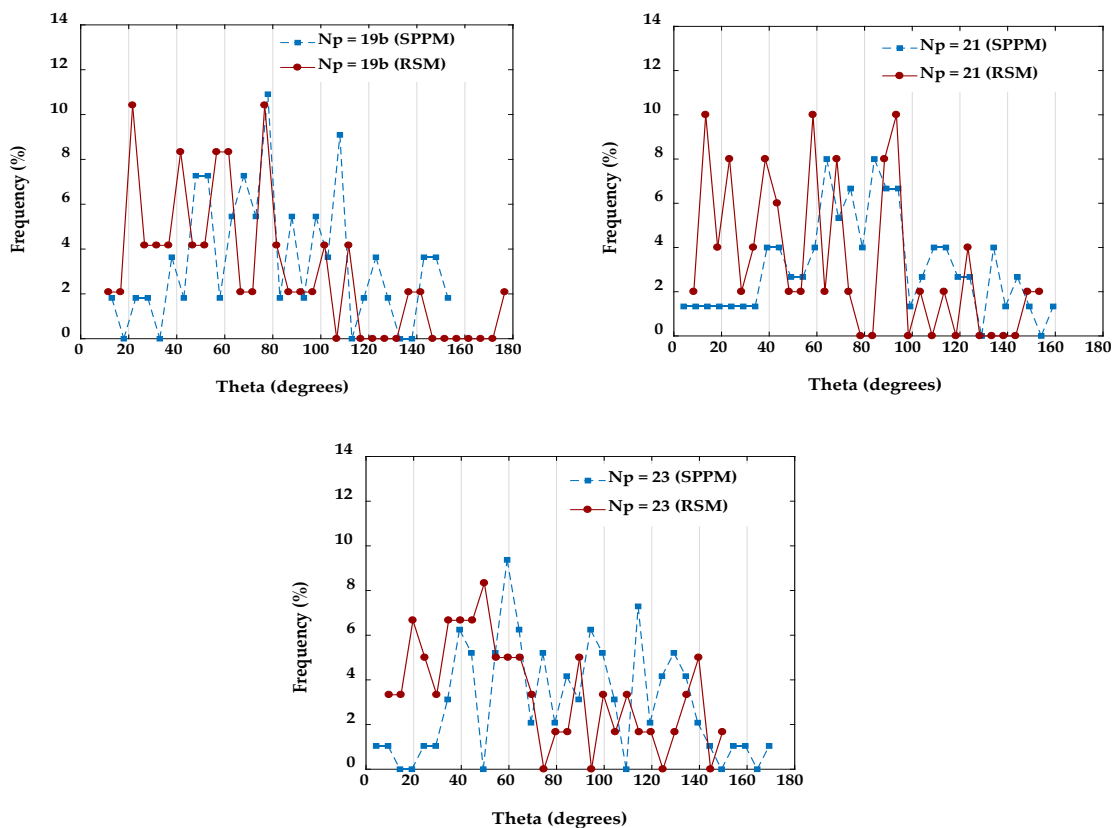


Figure 4.12: Coordination number of each primary particle for an agglomerate comprising of 8 primary particles: (a) RSM and (b) SPPM.

case) of neighboring particles was considered, MCN values around 3 were obtained, which is in good agreement with the value derived by the RSM in the present study. Yang, Zou, and Yu [2000] and Yang et al. [2008] conducted research work to study the packing properties of fine particles and analyzed the mechanical properties of agglomerates by DEM. The study further dealt with effects of packing density and coordination number on agglomerate size. The results showed that for large agglomerates the coordination number of primary particles normally varies between 3 and 10, which is in good agreement with the results obtained in this study (none of the agglomerates had coordination number greater than 10). On the other hand, the mean coordination number calculated in [Yang, Zou, and Yu, 2000; Yang et al., 2008] for primary particle size of  $200 \mu\text{m}$ , similar to the size range of maltodextrin particles ( $300\text{-}500 \mu\text{m}$ ), and porosity of 40% was  $\text{MCN} = 5.78$ , which is not in agreement with the present results. This might be due to the fact that the studied particles were of uniform spherical shape unlike in the present study, and also not undergoing glass transition.

#### 4.4.2 Distribution of coordination angle

Figs. 4.13 and 4.14 represent the coordination angle distribution results for medium and large size agglomerates. Fig. 4.15 shows the distribution of coordination angle for the largest agglomerate of the series. The trend of the results for different sizes of agglomerates is such that the distribution of coordination angle does not significantly depend upon the number of primary particles in the agglomerate, which is in good agreement with the results in [Dadkhah and Tsotsas, 2014; Brasil et al., 2001]. As shown in Figs. 4.13, 4.14 and 4.15, the angle between the triplets is distributed over a wide range ( $0 - 180^\circ$ ) and the results for both models do not show any prominent peak for a specific angle, which is similar to the result obtained by Brasil et al. [2001] for simulated agglomerates without restructuring (collapsing of open-branched structure in a way to increase the number of bonds between neighboring primary particles). In the SPPM the coordination angle is mostly distributed over the range of  $40 - 140^\circ$  and it decreases noticeably for angles out of this range. In contrary, for the RSM the frequency of distribution is high for angles below  $40^\circ$ .



**Figure 4.13:** Coordination angle distribution of medium size agglomerates.

In comparison with the study performed by Dadkhah, Peglow, and Tsotsas [2012] the results obtained here reveal different behaviors, which is expectable in view of various differences in the size and material properties. The agglomerates in the present study consist

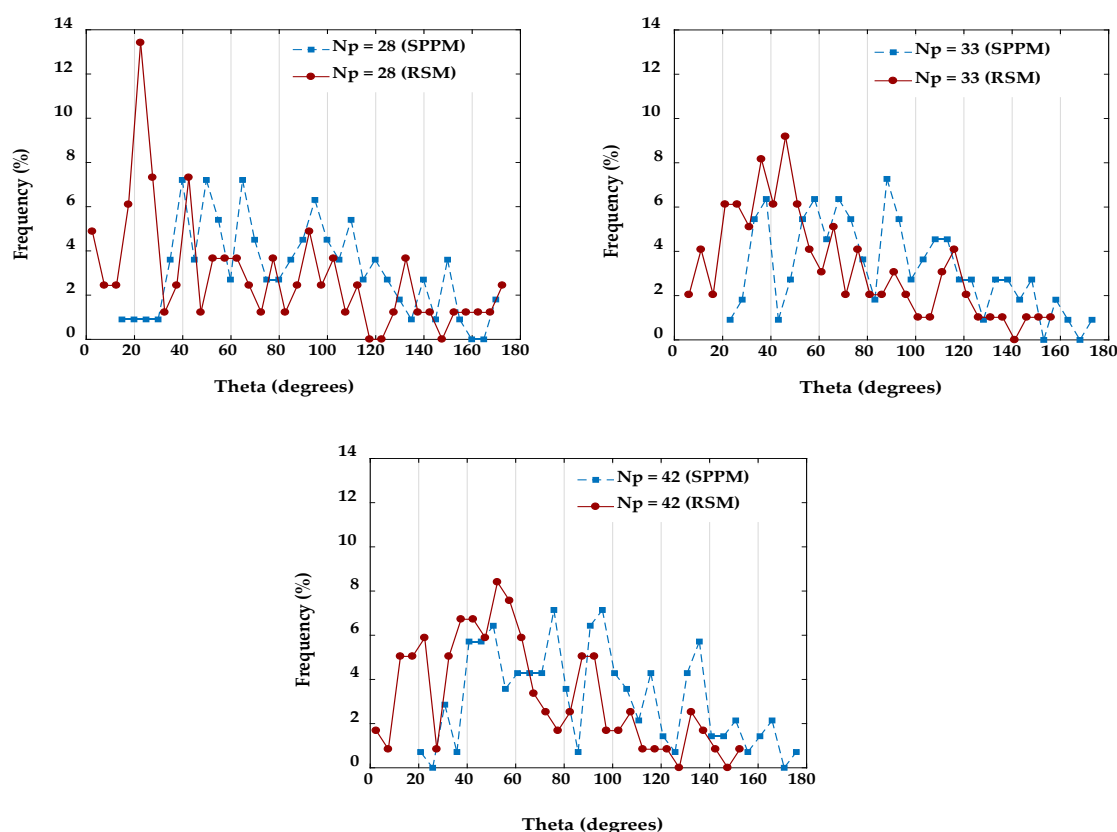
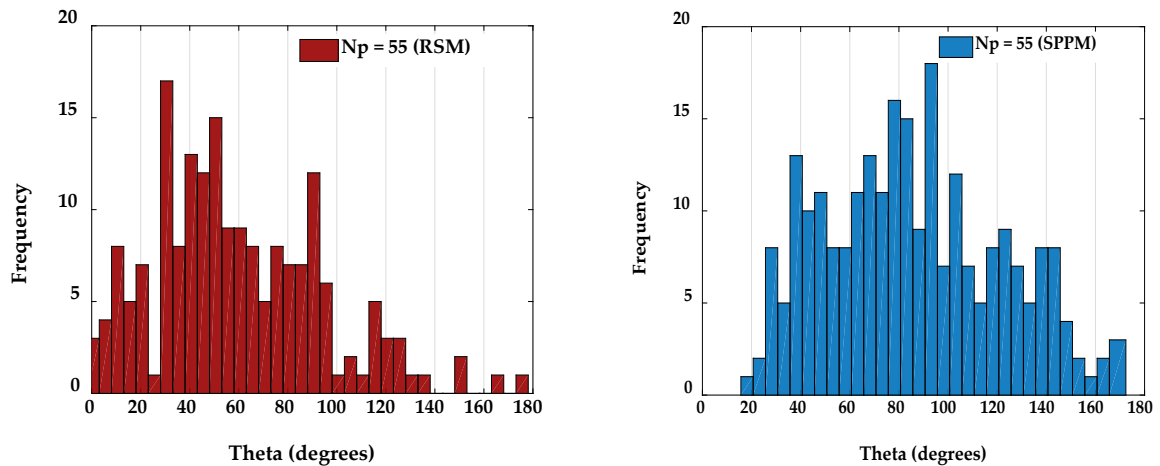


Figure 4.14: Coordination angle distribution of large size agglomerates.

of polydispersed primary particles with irregular shapes, therefore the range of coordination angle is widely distributed between  $0 - 180^\circ$ , whereas in the monodispersed primary particle agglomerates of Dadkhah et al. the distributions of coordination angle were clearly in the range of  $60 - 180^\circ$ . It is clear that when three spheres with the same radius stick together without overlapping the angle between them cannot be below  $60^\circ$ . The most frequent coordination angle reported by Dadkhah et al. was  $60^\circ$  which was similar to the results of simulated restructured cluster-cluster aggregates of Brasil et al. [2001]. In the present work, there was no evident mechanism of restructuring of primary particles during the production of agglomerates in the fluidized bed. This point can also be supported by the sticky nature of maltodextrin material which prevents the primary particles from rearranging and thus makes them form a rather compact structure during the agglomeration process. The results obtained from simulated agglomerates in [Brasil et al., 2001] mainly focus on aggregation mechanisms and aggregate size but lack the consideration of material characteristics, which are quite influential, as observed here.





**Figure 4.15:** Coordination angle distribution for the largest agglomerate of the series.

#### 4.4.3 Radial distribution of primary particle centers

As explained previously, two different methodologies have been employed to compute the radial distribution of primary particles. The first approach leads to the cumulative radial distribution of primary particles while the second method leads to the particle density function of the agglomerate. In both methods the radial distance is normalized by dividing with maximum radial distance, which is the distance of the center of the farthest primary particle to starting point.

##### Cumulative radial distribution of primary particles

The methodology of cumulative radial distribution (CRD) was discussed in the study of Lagarrigue et al. [2010] for agglomerates produced by simulation with pre-defined morphological parameters. It was then followed by Dadkhah and Tsotsas [2014] on monodispersed primary particles of alumina and glass beads. Similarly as shown for the previous morphological descriptors, Figs. 4.16a and 4.16b illustrate the cumulative radial distribution of primary particle centers for medium and large size agglomerates. Fig. 4.16c shows the cumulative radial distribution for the largest agglomerate of the series and a comparison with the work of Dadkhah and Tsotsas [2014].

It can be deduced from the cumulative radial distribution of primary particle centers in medium size agglomerates that their internal structure arrangement was of similar trend. Hardly any primary particle center can be observed close to the centroid of the agglomerate. The CRD curve for large agglomerates shows a similar trend with approximately 10% more particle centers at half of the radial distance in comparison with medium size agglomerates. The agglomerate with  $N_p = 42$  showed an exceptional trend among the large size

agglomerates, because almost 80% of the primary particle centers were concentrated in the region of half of the radial distance from the gravity center. The largest agglomerate of the series had a nearly linear relationship between radial distance and the number of included primary particle centers. The results of Dadkhah and Tsotsas [2014], refer to large agglomerates with greater number of primary particles. The CRD curve of our largest agglomerate with  $N_p = 55$  does not show good agreement when compared with an agglomerate with  $N_p = 289$  from Dadkhah's work (see Fig. 4.16c). It can be observed in Fig. 4.16c that in the agglomerate with  $N_p = 289$  around 30% more primary particle centers are present within half of the radial distance as compared to our agglomerate with  $N_p = 55$ . This proves that the agglomerates produced by Dadkhah, were more compact in comparison with the maltodextrin agglomerates.

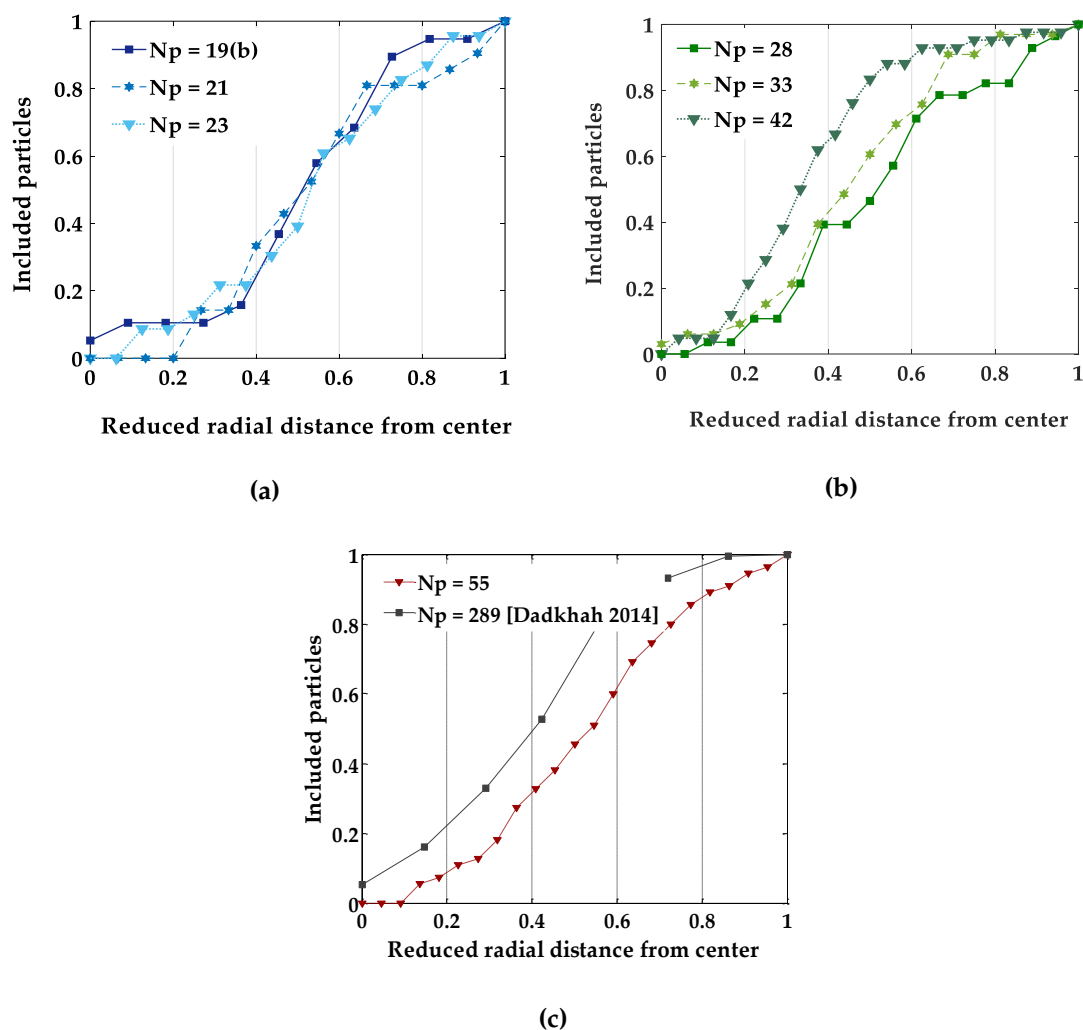


Figure 4.16: Cumulative radial distribution of primary particle centers for medium size (a), large size (b) and largest agglomerate (c).

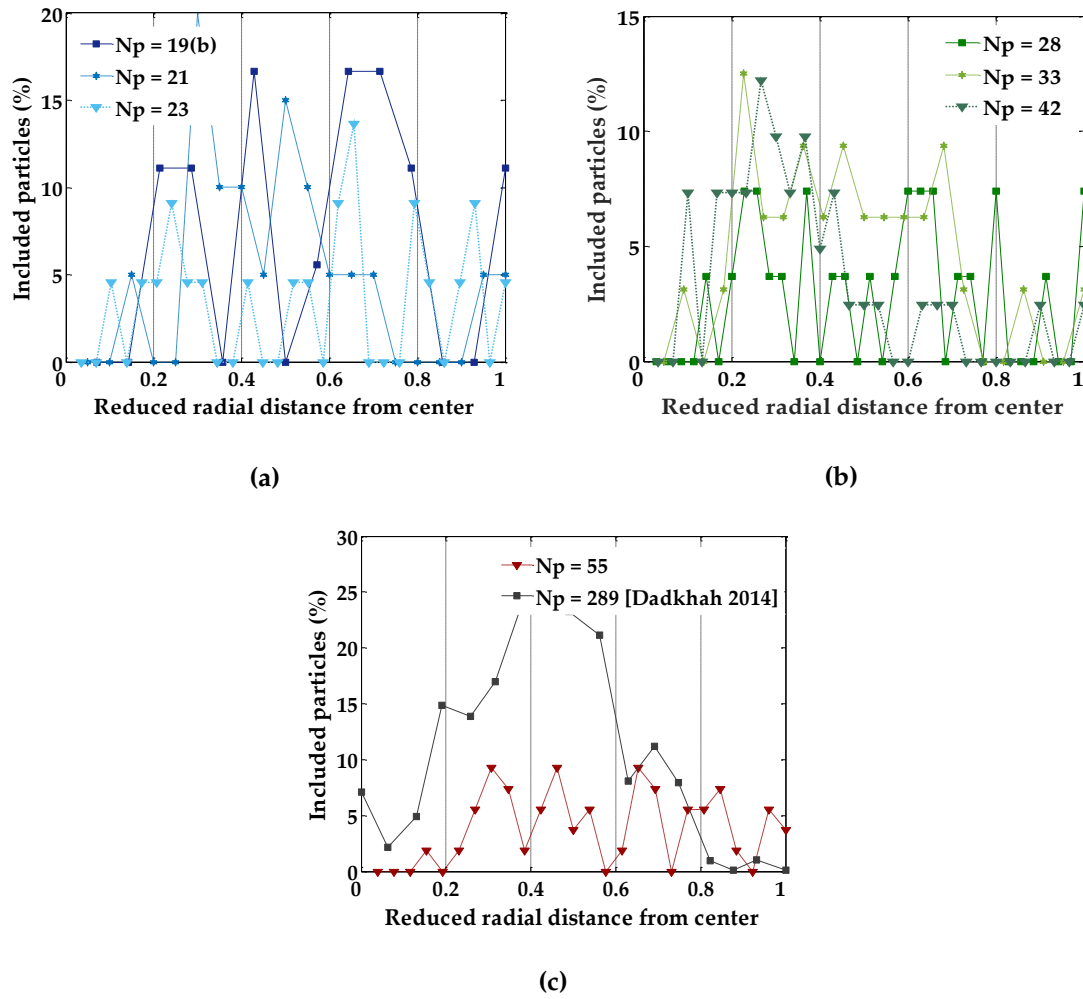
### Particle density function

The results for particle density function are shown in Fig. 4.17, for medium size, large size and the largest agglomerate. In Fig. 4.17a for medium size agglomerates it can be seen that primary particle centers are distributed non-uniformly in the form of chunks along the radial distance of the agglomerate. However, the curve becomes more uniform when the number of particle centers increases, as in the case of  $N_p = 23$ . Similarly, for large size agglomerates the results in Fig. 4.17b show slightly more uniform particle density as compared to medium size agglomerates due to increase in the number of primary particle centers. This plot also displays the previously mentioned exception for the case of the agglomerate with  $N_p = 42$ , whose particle density is higher near its centroid. The largest agglomerate PDF in Fig. 4.17c seems to be the most uniform within the series, as the particle density remains nearly equal throughout the radial distance. The particle density function does not exactly describe the structural arrangement of primary particles, it can however provide a good estimate of agglomerate structure.

A comparison of the present work with the study of Dadkhah and Tsotsas [2014] can be seen in Fig. 4.17c. The result for agglomerate  $N_p = 289$  from [Dadkhah and Tsotsas, 2014] nearly represents a symmetrical distribution of primary particle centers along the reduced radial distance, which is quite different from the results obtained in the present study. The results obtained in the present study are based on agglomerates having irregularly shaped primary particles where the individual primary particle size also varies appreciably. In contrast, the results from [Dadkhah and Tsotsas, 2014] refer to agglomerates that have spherically shaped monodispersed primary particles. Secondly, the number of particle centers involved in the present study is quite low as compared to the previous one. Therefore, several drops are observed in the PDF curves showing that no particle center exists in some of the steps along the radial distance.

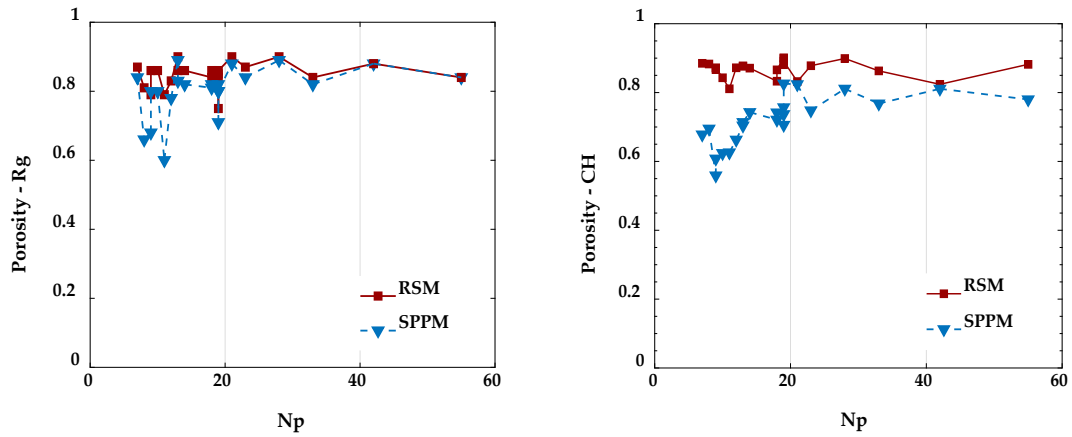
#### 4.4.4 Porosity of open pores

The main purpose of carrying out open porosity calculations in this study was to compare and understand the changes in the results when using the spherical primary particle model or the real structure of the agglomerates. Fig. 4.18 displays the comparison of porosities evaluated by the method of radius of gyration ( $R_g$ ) and convex hull (CH) for both models. It can be observed that for the SPPM, porosities evaluated by radius of gyration are higher than the ones evaluated by convex hull method. Both (blue) curves in Fig. 4.18 follow similar trend with nearly identical variation in results within subsequent  $N_p$ -increments. However, for the real structure the differences in porosity values between the two methods (red curves) is much less and the average values for porosity are nearly the same (see Appendix A, Table A.2).



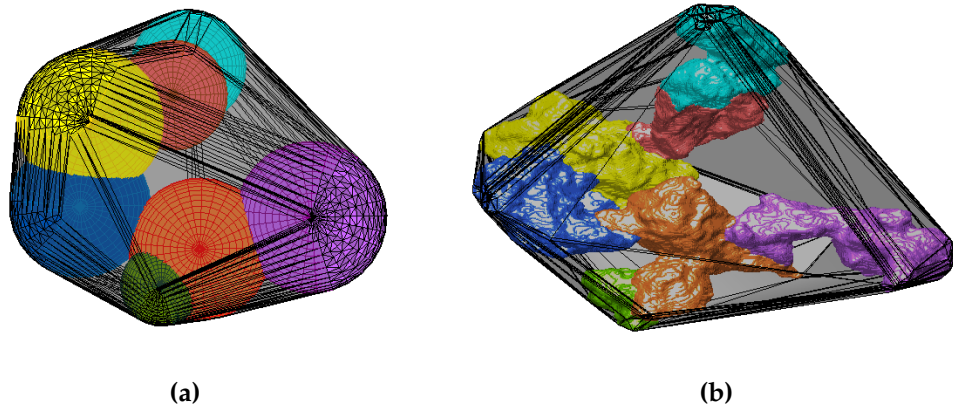
**Figure 4.17:** Particle density function of primary particle centers for medium size (a), large size (b) and largest agglomerate (c).

Fig. 4.18 also shows that at low values of  $N_p$  the deviation in porosity between SPPM and RSM is relatively high, but the models converge with increasing  $N_p$ . The average porosity values based on the radius of gyration method are very close for both models,  $\varepsilon(R_g - SPPM) = 0.80$  and  $\varepsilon(R_g - RSM) = 0.85$ . Porosity depends on to the total volume of agglomerate, and in this method the total volume of agglomerate directly depends on the radius of gyration, which does not change appreciably for polydispersed spherical particles and the voxel based real structure of the agglomerate. The average porosities obtained by the convex hull method are  $\varepsilon(CH - SPPM) = 0.72$  and  $\varepsilon(CH - RSM) = 0.86$ . As solid volume  $V_i$  is constant for both models, the differences in porosity are due to the larger volume of convex hull for the real structure. The main reason for this is the irregularity of real structure, convex hull volume significantly depending upon the extent of irregularity. The minimum convex hull region for an exemplary agglomerate consisting of 7 primary particles is shown for both (a) spherical primary particles and (b) the real structure in Fig. 4.19. It can be observed that the RSM agglomerate tends to occupy a larger convex hull region as compared to the SPPM agglomerate. As a consequence, it has larger volume and hence



**Figure 4.18:** Porosities of SPPM and RSM calculated by the methods of radius of gyration and convex hull.

larger estimated value of porosity.



**Figure 4.19:** Convex hull volume for an agglomerate comprising of 7 primary particles (a) spherical primary particles model and (b) real structure model.

Higher open pore porosity by radius of gyration than by convex hull method is in agreement with Dadkhah and Tsotsas [2014]. The open pore porosity evaluated for not too small maltodextrin agglomerates by different methods and for different models seems to be in the range of 70-85%, which is quite high as compared to previously studied agglomerates produced in a fluidized bed [Dadkhah, Peglow, and Tsotsas, 2012; Farber, Tardos, and Michaels, 2003]. The most frequent value of open pore porosity obtained in the study of Dadkhah, Peglow, and Tsotsas [2012] was 63% for glass beads. The reason of this difference, as mentioned previously, is seen in the solubility of amorphous maltodextrin in water, which leads to creation of non-uniform open structure of agglomerates contrary to the more compact agglomeration of insoluble glass beads by means of a binder.



## Chapter 5

# Fractal dimension and prefactor of agglomerates with irregular structure

*This chapter is partly taken from the paper "Fractal dimension and prefactor of agglomerates with irregular structure, Powder Technology (2018)".*

### 5.1 Introduction

Characterization of the morphology of the produced agglomerates can lead to a better understanding of the agglomeration mechanism by which they are formed and their resulting physical and chemical properties. When the irregularity of the agglomerates increases, their surface area also increases, which has an influence on the instant properties of agglomerates like dispersing and dissolving in liquids. Also the morphology of the agglomerates has an influence on their aerodynamic behavior during fluidization or in handling processes [Lapuerta, Martos, and Martín-González, 2010; Ibaseta and Biscans, 2010]. The complex structure and widely scattered shape of maltodextrin agglomerates produced in fluidized bed and their impact on end-use properties make a morphological and structural characterization necessary. The most common way to describe the morphology of agglomerates is fractal dimension which can be used as a measure of the openness of the structure. The popularity of fractal dimension arises from the large amount of information that can be deduced from it. It describes the agglomerate structure, necessary to model diffusion processes inside the agglomerates and agglomerate breakage, and it also gives information about the growth mechanism of the agglomerates [De Martín, Fabre, and Ruud van Ommen, 2014]. For instance, a small fractal dimension implies a small coordination number, and hence a smaller tensile strength of the agglomerate. Agglomerates with a small fractal dimension are then easier to disperse in a liquid, but they can also liberate more ultrafine particles in the air during powder handling [Ibaseta and Biscans, 2010]. The prefactor is another parameter whose importance is increasingly being appreciated; its value must correctly be known in order to fully define the fractal structure of a specific aggregate [Brasil, Farias,

and Carvalho, 1999]. The radius of gyration as a geometric measure of the spatial mass distribution around the aggregate center of mass should also be defined for calculating the fractal dimension.

Two general approaches are available in literature to determine the fractal dimension of agglomerates. The first approach is focused on simulated agglomerates in which most of the required data like number and position of the primary particles are easily accessible. Brasil et al. [2001] studied the effects of agglomeration mechanism and agglomerate size on the fractal dimension. The fractal dimension of agglomerates undergoing sintering and restructuring during agglomeration were also investigated. For instance, Lapuerta, Expósito, and Martos [2015] studied the effect of sintering on the fractal prefactor of agglomerates. Eggersdorfer et al. [2011] presented the evolution of the fractal dimension during viscous sintering of amorphous aerosol materials for aggregates simulated by various collision mechanisms. A correlation for the determination of the prefactor as a function of the fractal dimension and the number of elementary structures is proposed in [Lapuerta, Martos, and Martín-González, 2010]. Eggersdorfer and Pratsinis [2012] simulated agglomerates with four different collision mechanisms and the effects of polydispersity of primary particles on the fractal dimension and prefactor were investigated.

The second approach for estimating the fractal dimension uses real agglomerates which have been produced experimentally. In this regard, most investigators have been forced to estimate the fractal dimension by light scattering or studied projected images of collections of aggregates. The majority of these studies involved analysis of transmission electron microscope (TEM) or scanning electron microscope (SEM) projected images of aggregates. Hence, relationships between the two-dimensional information and the real three-dimensional properties are required. Ibaseta and Biscans [2010] compared the light scattering and electron microscope methods for calculating the fractal dimension of fumed silica. Köylü, Xing, and Rosner [1995] investigated the fractal dimension and prefactor of flame-generated aggregates by using angular light scattering and electron microscope images. Quantitative analysis of fractal dimension of soot agglomerates with the help of SEM and image processing techniques was performed by Chakrabarty et al. [2008] in order to find the dependence of particle morphology on particle electrical charging. Instead of the mean value of fractal dimension for a large series of agglomerates, Lapuerta, Ballesteros, and Martos [2006] suggested a new method to estimate the fractal dimension of individual soot agglomerates which can be applied to TEM images.

The main difficulty in the TEM and SEM analysis of aggregates is that three-dimensional (actual) morphological information must be inferred from projected (two-dimensional) images. This estimation of the fractal dimension of an agglomerate from its 2D projection often involves some assumptions and does not provide exact results. Here, X-ray micro tomography is used as an appropriate method to overcome this lack of data by a thorough characterization of the three-dimensional internal structure of agglomerates. After distinguishing



the primary particles that constitute an agglomerate, calculations of radius of gyration as an elementary step for deriving fractal dimension are discussed and compared based on two approaches: separated primary particles (monodisperse and polydisperse model) and voxel data. A number of techniques that can be used for fractal dimension estimation were discussed by Mandelbrot [Mandelbrot, 1983]. In the present study, two of those methods, the scaling law (power law relation) and the box-counting method were used because they are applicable for patterns with or without self-similarity (a self-similar object is exactly or approximately similar to a part of itself) [Melas et al., 2014; Foroutan-pour, Dutilleul, and Smith, 1999]. Computation of fractal dimension and prefactor by the scaling law is presented for both separated primary particles and real structure (voxel data). The radius of primary particles as an important parameter in the scaling law equation should be defined properly. Due to the irregular shape of maltodextrin primary particles, their radii can be considered based on corresponding ball radius or mean value of radii reported in 13 different directions. The effect of these two alternatives on fractal dimension and prefactor is discussed and compared to the values obtained from voxel data.

## 5.2 Radius of gyration

### 5.2.1 Radius of gyration based on separated primary particles

In this study the separation of primary particles is done by segmentation using the pre-flooded watershed method over X-ray images. Some post and pre image-processing steps are required in order to separate properly the primary particles. The comprehensive methodology and all the required details for separating primary particles with the pre-flooded watershed method are discussed in [Pashminehazar, Kharaghani, and Tsotsas, 2016].

Using the data extracted from volume images, the primary particles can be labeled and counted, providing the number of primary particles  $N_p$  per agglomerate. Center coordinates and volume of each primary particle are identified (Fig. 5.1). This data was stored in matrices for further evaluation such as calculating radius of gyration and fractal dimension. The definition and methods of calculating the radius of gyration were discussed thoroughly in Sec. 3.3. The maltodextrin agglomerates consist of polydisperse primary particles with different sizes and volumes. Therefore, the radius of gyration is calculated by implementing the obtained data in Eq. 3.3. However, the radius of gyration can also be approximated based on Eq. 3.4, which is valid for agglomerates consisting of monodisperse particles.

In Chapter 3, the radius of gyration for agglomerates was calculated based on the monodisperse assumption. Here, a comprehensive study of radius of gyration is presented for polydisperse or monodisperse primary particles and also for voxel data.

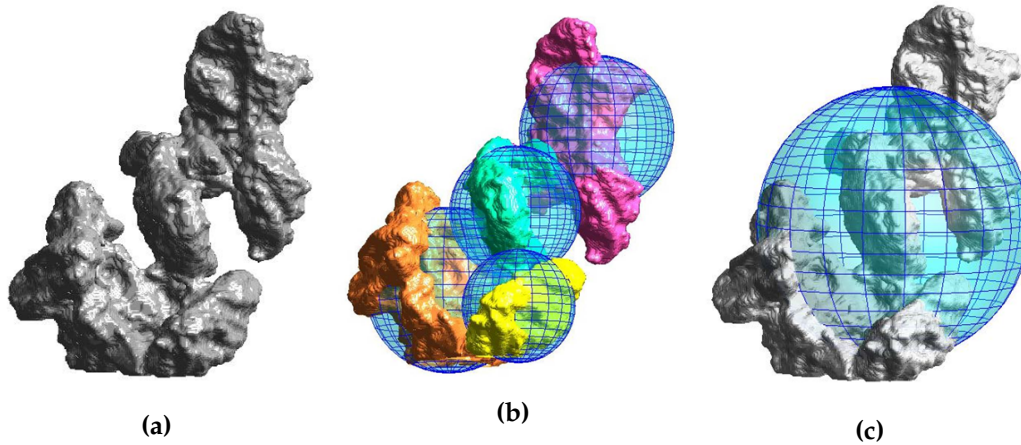


**Figure 5.1:** (a) The overall 3D view of a maltodextrin agglomerate, (b) separated primary particles, (c) estimated radius of gyration.

### 5.2.2 Radius of gyration based on voxel information

In order to calculate and compare fractal dimension and radius of gyration for the real structure of agglomerates, the voxel data obtained from the X-ray images of the agglomerate are used. In this regard, the 3D X-ray images are divided into series of 2D slices from one specified direction. Then the 3D matrix of the image is created based on all 2D slices with a Matlab code developed for this purpose. After that the positions of all the voxels which belong to the agglomerate structure (voxel value 1), are defined and stored. As exemplarily shown in Fig. 5.2, the 3D image of one agglomerate is divided into 342 slices with a size of  $327 \times 310$  pixels; all this pixel information is stored in a 3D matrix. By considering each voxel with value 1 as a separated element which has the same size and having the number of voxels and position vectors, the radius of gyration can be calculated based on Eq. 3.5. In this case, due to the large number of voxels, the computational time is long. Therefore, the downsampling function is applied to reduce the size of an image while conserving the basic information contained in the image. The reduction factor for each coordinate direction can be set separately.

## 5.3 Fractal dimension

A number of techniques that can be used for fractal dimension estimation were discussed by Mandelbrot [1983]. In this study, two of those methods, the scaling law (power law relation) and the box-counting method were used because they are applicable to patterns with or without self-similarity (a self-similar object is exactly or approximately similar to a part of itself) [Melas et al., 2014; Foroutan-pour, Dutilleul, and Smith, 1999].

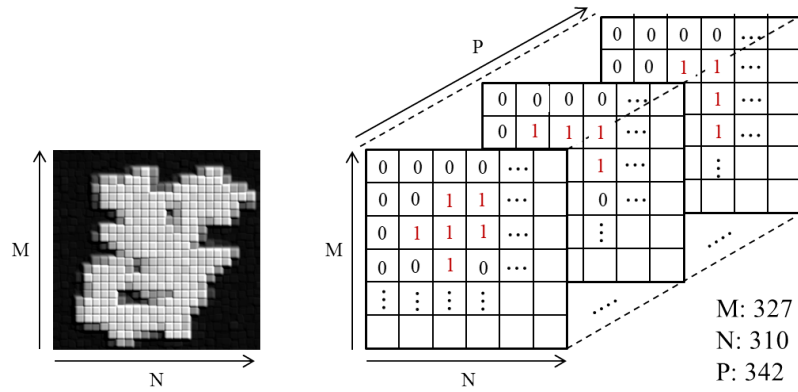


**Figure 5.2:** Schematic view of generating the 3D matrix of an agglomerate that is required for the voxel based method.

### 5.3.1 Scaling law (Power law equation)

The scaling law method which was introduced in Sec. 3.6 needs to collect data from a number of agglomerates, and finally provides a mean fractal dimension characteristic of the whole particle population. At the same time as the fractal dimension ( $D_f$ ), the prefactor ( $K_f$ ) of the power-law relationship is also obtained. This parameter, whose importance is increasingly being appreciated, is an essential ingredient for a complete description of a power-law aggregate [Melas et al., 2014]. The prefactor has also been termed lacunarity, filling factor or structural coefficient and mostly expresses how the primary particles are packed in an agglomerate [Lapuerta, Expósito, and Martos, 2015]. Agglomerates with similar size and fractal dimension may have different shapes, the difference being characterized by the prefactor.

The radius of gyration of the agglomerate is calculated based on the known positions of the primary particles or voxels (Eqs. 3.3 and 3.5). Since the primary particles of maltodextrin are not spherical, for calculating fractal dimension based on separated primary particles, the radius of each primary particle needs to be approximated. One option is reporting for each primary particle the radii in 13 discrete directions of the cuboidal lattice (3 coordinate directions, 6 face diagonals, 4 space diagonals) and then considering the mean value as the radius of the primary particle. Another option is the corresponding ball radius, i.e. the radius of a sphere with volume equal to primary particle volume. Therefore, maltodextrin agglomerates can be represented by a spherical primary particle model based on either the corresponding ball radii or the mean values of 13 reported radii [Pashminehazar et al., 2018]. At the end, for each agglomerate, the value of  $R_p$  in Eq. 3.14 is considered as the arithmetic mean value of primary particle radii obtained by either of the two mentioned approximations.

### 5.3.2 Box-counting method

The box-counting analysis is an appropriate method of fractal dimension estimation for images with or without self-similarity. This method is frequently used in various application fields because it is straightforward, automatically computable, and adaptable to many situations. However, this technique, including processing of the images and definition of the range of box sizes, requires a proper implementation to be effective in practice. The box-counting technique involves determination of the number of cells required to entirely cover an object with grids of boxes of varying size. For this purpose, first the 3D X-ray image is binarized and all the voxels belonging to the solid phase get the value 1 whereas air voxels get the value 0. Then, the entire image is covered by boxes of size  $\epsilon$  and all the non-empty boxes  $N(\epsilon)$  are counted. The procedure is repeated for smaller boxes and for each step two values are recorded:  $N(\epsilon)$  and  $\epsilon$ . All the steps are done for real 3D X-ray images of agglomerates with sequences represented in Fig. 5.3 for two-dimensional view. The regression slope of the straight line formed by plotting  $\log(N(\epsilon))$  against  $\log(\frac{1}{\epsilon})$  indicates the degree of complexity, or fractal dimension:

$$D_f = \lim_{\epsilon \rightarrow 0} \frac{\log(N(\epsilon))}{\log(\frac{1}{\epsilon})}. \quad (5.1)$$

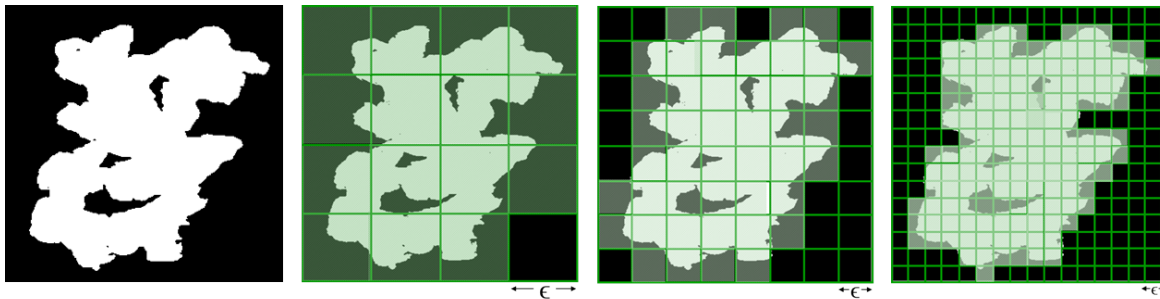


**Figure 5.3:** The sequence of calculating fractal dimension by the box-counting method for a single agglomerate (the size of boxes is decreased in each step and non-empty boxes are counted).

The box-counting dimension shows how rapidly the irregularities develop as  $\epsilon$  tends to 0 [Ai et al., 2014]. In contrast to the scaling law which gives the average value of a series of agglomerates, by this method the fractal dimension of an individual agglomerate can be calculated.

Different algorithms and software were used or developed for calculating fractal dimension based on the box-counting method. A comprehensive comparison between available software packages was conducted by [Hadzieva et al., 2015] to show which one has a better translation of the level of complexity or irregularity of objects with minimum error. For this comparison fractal images with known fractal dimensions were chosen. Based on this comparative analysis, the FracLac, Fractal Count and Fractalyse software packages have more

accurate results with an average error of below 1.5%. In this research, the Fractal Count package, which is easy to implement over a 3D image as a plugin of imageJ software has been chosen. ImageJ is an open source image processing software package, developed by Wayne Rasband (National Institute of Health, Bethesda, Maryland, USA) and designed for scientific multidimensional image analysis.

## 5.4 Results and discussion

### 5.4.1 Radius of gyration

For a series of agglomerates (20 agglomerates of Trial F, Table 2.2), the radius of gyration has been calculated based on Eqs. 3.3 and 3.5 which are valid for agglomerates made of polydisperse and monodisperse primary particles, respectively. Although the computation is easier by assuming monodisperse primary particles, the resulting value can be different from the polydisperse case. In Table 5.1 the values of radius of gyration for these two cases are summarized and compared. As it is observed there are differences in the calculated radii of gyration. For most agglomerates, the radius of gyration with monodisperse assumption is larger than the value obtained from polydisperse primary particles. In the maximum case the monodisperse gyration radius is 19% higher than the polydisperse value, and in minimum case it is 5% lower. The volume of each primary particle in the polydisperse case plays an important role in the calculated values.

For comparison, the radius of gyration is also calculated for the real structure of the agglomerate from the voxel coordinates and values of 3D X-ray images. In this study, in order to save time of computation, reduction factors of 3 and 4 have been applied for each direction (Fig. 5.4). Therefore, for example with reduction factor 4, each 4 voxels in X, Y, Z direction are combined and thus the number of voxels is decreased by factor of 64. In the case of a 3D image, the value of a voxel in the resulting image is the mean value of all voxels within a cuboid with the size of the reduction factor in the input image. As shown in Fig. 5.4, for the original image of the agglomerate the calculation of the radius of gyration is not feasible because the distances of each two voxels for more than 3 million voxels would need to be estimated. After reduction by a factor of 3 or 4, however, the radius of gyration can be calculated. The calculation time by reduction factor of 4 is decreased significantly (by around 90%) in comparison to a reduction factor of 3 while the gyration radius is not noticeably changed. For the same agglomerate, the radius of gyration based on separated monodispersed primary particles is also shown in Fig. 5.4. The radius of gyration was calculated with both the mentioned reduction factors of 3 and 4 for several agglomerates which were produced with almost the same conditions as the agglomerates of Table 5.1 but at somewhat lower injection rate (Trial D, Table 2.2). Results in Table 5.2 show that the calculated values are almost identical and only a minor difference is observed. Although values

**Table 5.1:** The radius of gyration of agglomerates using either the polydisperse or the monodisperse primary particle (PP) model (Eq. 3.3 and Eq. 3.5).

Agg no.	$N_P$	Volume of solid phase ( $\mu m^3$ ) * $10^8$	Monodisperse	Polydisperse	Difference $R_g(1)-R_g(2)$ ( $\mu m$ )
			PP (Eq. 3.5) $R_g(1)(\mu m)$	PP (Eq. 3.3) $R_g(2)(\mu m)$	
n1	5	1.34	361.62	291.34	70.28
n2	5	1.12	281.71	279.39	2.32
n3	5	1.26	399.55	374.23	25.32
n4	5	1.29	380.99	379.87	1.12
n5	5	1.12	395.98	383.34	12.64
n6	6	1.05	376.67	394.00	-17.33
n7	6	1.28	462.89	407.23	55.66
n8	6	1.11	347.27	319.46	27.81
n9	7	1.70	424.87	436.24	-11.37
n10	7	1.86	575.28	499.79	75.49
n11	7	1.38	452.06	389.79	62.27
n12	9	1.81	604.43	535.95	68.48
n13	9	1.87	484.62	455.41	29.21
n14	10	1.62	484.88	468.63	16.25
n15	10	1.92	553.77	564.04	-10.27
n16	11	2.15	722.02	636.01	86.01
n17	15	2.99	684.34	606.35	77.99
n18	16	4.48	857.14	809.01	48.13
n19	16	2.62	499.39	505.31	-5.92
n20	26	4.05	666.42	678.51	-12.09

estimated with a reduction factor of 3 are more accurate, using the reduction factor of 4 is much more effective considering the computation time. Therefore, for further evaluation of agglomerates from Table 5.1, downsampling with reduction factor 4 is applied.

Values of the radius of gyration calculated based on either voxel information or separated polydisperse particles (from Table 5.1) are compared in Fig. 5.5. The  $R_g$  value obtained from voxel data corresponds to the real structure of the agglomerate in which all irregularities are considered. Therefore, as shown in Fig. 5.5, the gyration radii based on voxel data are higher than radii calculated from separated polydisperse primary particles. In general, values of the gyration radius are difficult to interpret immediately and compare with other data for agglomerates. However, for calculating fractal dimension having this data is necessary.

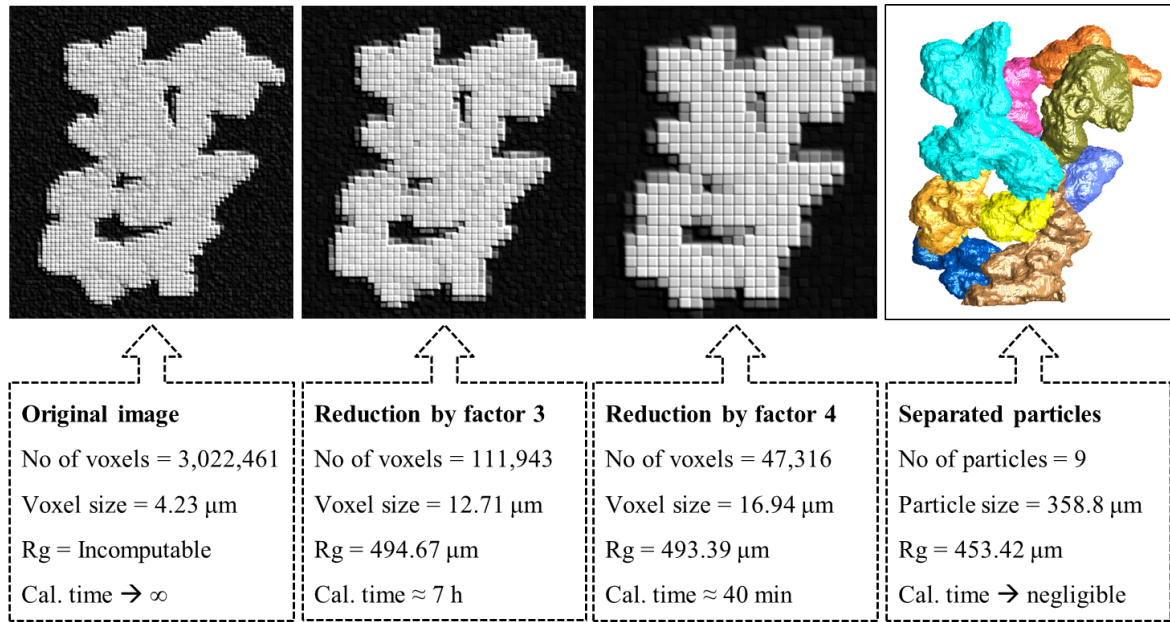


**Figure 5.4:** Illustration of the calculation of the radius of gyration based on voxel data with different reduction factors and also based on separated primary particles.

#### 5.4.2 Fractal dimension (Scaling law)

For estimating fractal dimension based on the scaling law, it is necessary to have the value of the radius of gyration and of the mean radius of primary particles. The radius of gyration obtained with different methods has been discussed in Sec. 5.4.1. The radius of each primary particle can be set equal to the corresponding ball radius of equal volume or to the mean value of 13 characteristic radii. Those two values are not same. Therefore considering each of these values has an influence on the calculated value of fractal dimension and prefactor. Fractal dimension and prefactor obtained by the two mentioned options of primary particle radius determination are reported in Table 5.3.

As can be noticed in Table 5.3, the fractal dimension values obtained from separated primary particles are almost the same but the prefactor changes significantly by considering different values for the radius of primary particles. When the radius of primary particles is based on the mean over 13 lattice directions, due to the larger value, the overlapping of primary particles (virtual sintering) is increased and a higher value for the prefactor is obtained. Oh and Sorensen [1997] showed that, although the effect of sintering is very relevant for the prefactor, it is very small in regard of the fractal dimension. From the simulations in [Oh and Sorensen, 1997] it was observed that the prefactor value reaches up to 3 by increasing the sintering between primary particles. Also in [Lapuerta, Expósito, and Martos, 2015] it was mentioned that sintering increases the prefactor significantly, which leads to a slight decrease in the fractal dimension of the agglomerates. Certainly, very high sintering coefficients would lead to coalesced agglomerates, which would sharply increase

**Table 5.2:** Gyration radii calculated from voxel data for different reduction factors.

Reduction by factor 3			Reduction by factor 4			Difference
No. of voxels	Voxel size ( $\mu m$ )	$R_g(1)$ ( $\mu m$ )	No. of voxels	Voxel size ( $\mu m$ )	$R_g(2)$ ( $\mu m$ )	$R_g(1)-R_g(2)$ ( $\mu m$ )
107651	12.77	517.99	45610	17.02	517.39	0.6
66796	12.81	421.59	28411	17.08	421.75	-0.16
52103	12.81	375.66	22252	17.08	376.17	-0.51
66569	12.81	401.69	25734	17.08	402.27	-0.58
53720	12.81	354.96	22650	17.08	353.75	1.21
102632	12.81	432.55	43574	17.07	432.35	0.2
65871	12.81	446.02	27941	17.08	445.79	0.23
46799	12.81	415.81	19824	17.08	415.52	0.29
59273	12.73	502.47	25191	16.97	502.8	-0.33
36783	12.73	384.95	15656	16.97	385.27	-0.32
90624	12.71	417.04	38450	16.94	417.03	0.01
59272	12.71	421.33	25208	16.94	421.32	0.01
79021	12.71	445.84	33460	16.94	445.44	0.4
111943	12.71	494.67	47316	16.94	493.39	1.28

**Table 5.3:** Fractal dimension and prefactor of agglomerates calculated based on separated primary particles and voxel data.

	Separated primary particles (polydisperse)		Voxel data
	$R_p$ based on corresponding ball radius	$R_p$ based on mean radius (obtained in 13 directions)	
$D_f$	1.68	1.60	1.92
$K_f$	1.45	3.12	49.0
$r^2$	0.84	0.83	0.87

their fractal dimension. These trends are also in agreement with results by Eggersdorfer et al. [2012] in which during sintering the fractal dimension goes first through a moderate minimum before increasing sharply to 3 for a compact sphere.

A very wide range of prefactor values can be found in the literature. Lapuerta et al. conducted a comprehensive comparison of fractal dimensions and prefactors for experimental and simulated agglomerates [Lapuerta, Martos, and Martín-González, 2010]. Low values of prefactor, 0.82 and 0.53, have been reported for diffusion-limited particle-cluster agglomeration (DLPCA) and ballistic particle-cluster agglomeration (BPCA), respectively [Eggersdorfer et al., 2011]. However, some experimental studies on soot agglomerates resulted in prefactors up to 4.95, 8.50, or even 9.00 [Lapuerta, Martos, and Martín-González, 2010]. The prefactor for  $\gamma$ - $AL_2O_3$  agglomerates which were produced with binder in a spray fluidized bed was reported at around 1.6 [Dadkhah, Peglow, and Tsotsas, 2012]. In



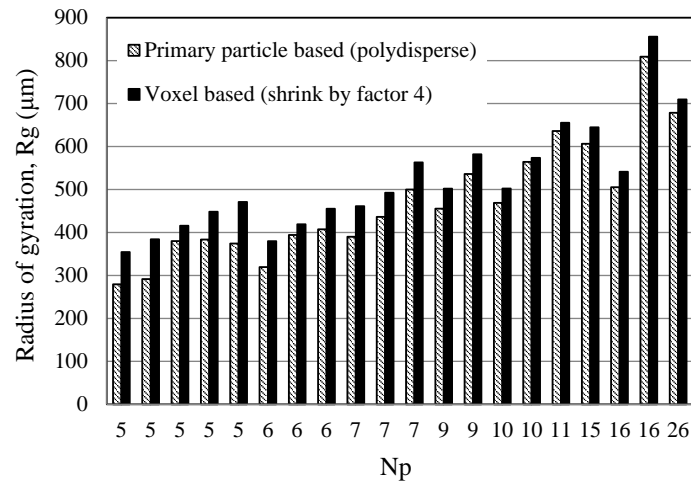


**Figure 5.5:** Radius of gyration calculated for series of agglomerates based on separated primary particles and voxel data.

that case the primary particles were nearly spherical and mono-dispersed, with no real and relatively small virtual sintering.

For the voxel based calculation, the number of voxels is considered as a number of primary particles ( $N_p$ ). A larger value of fractal dimension,  $D_f = 1.92$ , is obtained in this case, which is more comparable with results reported for spray fluidized bed agglomerates. The prefactor obtained by this method is 49.0 which is much higher than most of the values reported in literature. However, for some agglomerates made of fluidized nanoparticles prefactors in the range of 17-140 were presented [De Martín, Fabre, and Ruud van Ommen, 2014].

In general it can be concluded that the fractal dimension is an indicator of the overall agglomerate shape (large-scale morphology), while the prefactor becomes an indicator of local structure (small-scale morphology). Wu and Friedlander [1993] also mentioned that the prefactor is a descriptor for the packing of primary particles. Alternative indicators of local compactness can be the coordination number and angle of primary particles. In [Melas et al., 2014] it was noted that for a fixed value of fractal dimension, as the prefactor increases the number of small coordination angles ( $< 80^\circ$ ) increases. This observation also indicates that the prefactor is a measure of local structure and compactness. Therefore, obtaining a very large value of the prefactor by the voxel based method is expectable, because each voxel is considered as a primary particle in this method, and most of those virtual primary particles are very closely and compactly packed.

In general the low value of fractal dimension obtained either based on separated primary particles or voxel data illustrates the non-compact and fluffy structure of maltodextrin agglomerates in comparison to  $\gamma\text{-}AL_2O_3$  agglomerates which were produced with binder at otherwise almost same conditions and had a fractal dimension around 2.61 [Dadkhah, Peglow, and Tsotsas, 2012]. The sticky and plasticized surfaces of maltodextrin particles

during agglomeration lead to the creation of more irregularly shaped agglomerates with open structures in the spray fluidized bed. Another reason for the open structure of maltodextrin agglomerates is the polydispersity of primary particles (the geometric standard deviation of maltodextrin primary particle size is 1.24). It was pointed out by Eggersdorfer and Pratsinis [2012] that the presence of various primary particle sizes results in more space between them during agglomeration. They showed that for different collision mechanisms of agglomeration, the fractal dimension decreases monotonically with increasing polydispersity. That is most notable for particle–cluster and to a smaller extent for cluster–cluster ballistic and diffusion-limited collision-generated agglomerates. Eventually regardless of the collision mechanism the fractal dimension reaches 1.5 as the geometric standard deviation of primary particles increases to 2.5 [Eggersdorfer and Pratsinis, 2012]. For the prefactor such monotonic behavior was not reported. The fractal dimension reported in Chapter 3 for maltodextrin agglomerates was 1.81. This value was determined based on separated primary particles and is higher than the present value of 1.60 (Table 5.3). The main reason for this difference is that the spraying rate used in Chapter 3 for the production of the agglomerates was lower than here (1.75 g/min instead of 2.25 g/min corresponding to trials D and F from Table 2.2). Consequently, the agglomerates structure was less irregular in Chapter 3.

Most of the values of fractal dimension reported in literature are for soot agglomerates which have been generated experimentally or by simulation; a comprehensive comparison is available in [Lapuerta, Martos, and Martín-González, 2010; Brasil, Farias, and Carvalho, 2000]. The simulated agglomerates are usually generated based on two main algorithms: cluster-cluster mechanism which naturally leads to open-structured morphologies and particle-cluster mechanism which is appropriate to create compact agglomerates. Therefore, low values of fractal dimensions (below 2) were reported for cluster-cluster generated agglomerates while higher values (above 2) resulted from the particle-cluster approach. For example, Eggersdorfer and Pratsinis have reported that agglomerates made by diffusion-limited cluster–cluster agglomeration (DLCCA) have  $D_f = 1.79$ , by diffusion-limited particle–cluster agglomeration (DLPCA) have  $D_f = 2.25$ , by ballistic cluster–cluster agglomeration (BCCA) have  $D_f = 1.89$ , and by ballistic particle–cluster agglomeration (BPCA) have  $D_f = 2.81$ . Simulation results by Brasil et al. [2001] yielded  $D_f = 1.82$  and 2.75 for cluster-cluster and particle-cluster aggregates, respectively. As can be noticed the fractal dimensions of synthetic cluster-cluster agglomerates are comparable to the fractal dimensions presented in this study.

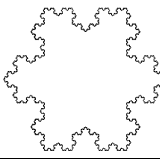

From experimental data for aerosol agglomerates, fractal dimensions in the range of 1.75 to 1.88 for diesel soot,  $D_f = 1.62$  for ethylene and  $D_f = 1.40$  for acetylene soot have been reported in [Lapuerta, Martos, and Martín-González, 2010]. The reported low values of fractal dimension, which are in good agreement with the current study, suggest that the growth of soot agglomerates is mostly controlled by the cluster-cluster mechanism. It seems

that in present study also after the agglomeration process started miniature aggregates of primary particles were created rapidly due to the sticky nature of maltodextrin and then combined to larger structures by cluster-cluster agglomeration.

### 5.4.3 Fractal dimension (Box-counting)

In using the box-counting method, challenges arise when the range of box sizes is to be determined [Foroutan-pour, Dutilleul, and Smith, 1999]. In this study the largest box was chosen as one quarter of the largest side of the image and the box size has been decreased by a factor of 2 in each iteration step until it reached  $6 \times 6 \times 6$  pixels in 3D or  $6 \times 6$  pixels in 2D. Two 2D images with known fractal dimension were used to validate our setting of the box-counting method. As seen in Table 5.4 the estimated values are very close to the theoretical values. A similar procedure in regard of box sizes and limitation was also reported in [Foroutan-pour, Dutilleul, and Smith, 1999] for proper implementation of the box-counting method. The described procedure was applied over the 3D X-ray image of each of the 20 agglomerates of Table 5.1, and the mean value of the fractal dimension was obtained to  $D_f = 2.25 \pm 0.030$ .

**Table 5.4:** Testing the box-counting setting for known fractal images.

Name	Koch snowflake	Sierpinski triangle
Image		
Theoretical value	1.26	1.58
Estimated value (Fractal Count)	1.31	1.56

Most of the studies using the box-counting method for the calculation of fractal dimension are in two dimensions and the reported values are smaller than our case. For example, the 2D fractal dimension for silver nanoparticles was reported in a range of 1.73 to 1.84 by Shin et al. [2009] and at 1.58 by Ku and Maynard [2006]. For soot aerosol agglomerates the 2D fractal dimension was around 1.75 and for more elongated agglomerates it was around 1.46 [Chakrabarty et al., 2008]. Recently a 3D investigation with the box-counting method for simulated agglomerates has been conducted by Sommerfeld and Stübing [2017]. They have reported that the fractal dimension is scattered around a value of 2.1, which is in good agreement with the result obtained in this study.

In the present study, the fractal dimension calculated by using the box-counting algorithm is larger than the value obtained from the scaling law method based on voxel data (by almost 15%). Not having the same values is expectable because the basics of the two methods are completely different. It is also reported in [Dietzel and Sommerfeld, 2013] that

different approaches for calculating the fractal dimension of a three-dimensional object can lead to different results. Not many articles are available comparing these two methods for the same object. In [Shin et al., 2009], for agglomerates of silver nanoparticles, the 2D fractal dimension calculated from the box-counting method was also around 16% higher than the value obtained by the scaling law. Moreover, for soot aerosol agglomerates higher values of fractal dimension from the box-counting method were reported in comparison to the scaling law [Chakrabarty et al., 2008].

## Chapter 6

# Influence of process parameters on morphological characterization

### 6.1 Introduction

Different studies were performed on the effect of process parameters such as fluidizing air flow rate, temperature, agglomeration time and binder injection rate on agglomerate growth kinetics as well as on the physical, mechanical and rheological properties of agglomerates [Avilés-Avilés, Dumoulin, and Turchiuli, 2015; Dopfer et al., 2013; Ziyani and Fatah, 2014]. Fries et al. [2014] describes the influence of process parameters (i.e., fluidization air flow rate, temperature, and liquid injection rate) and the granulator configurations (i.e., top spray, Wurster coater, spouted bed) on the agglomeration behavior of amorphous food powders in fluidized beds. He experimentally investigated the behavior of maltodextrin agglomeration in terms of growth rate, process stability, and product particle structure and strength. The fluidization regime, and the particle and collision dynamics were also simulated by using a discrete particle model (DPM) under different process conditions and in different granulator configurations [Fries et al., 2014].

A stochastic model was developed by Terrazas-Velarde, Peglow, and Tsotsas [2009] to describe agglomerate growth and particle formation during fluidized bed spray agglomeration. The performance of the model was improved and evaluated by analyzing the effect of variation of process parameters on agglomeration kinetics and comparing with the experimental results. Investigated process parameters were the binder addition rate, the binder initial viscosity, the superficial fluidization velocity and the gas inlet temperature [Terrazas-Velarde, Peglow, and Tsotsas, 2011a]. Most of the simulations and modeling of fluidized bed agglomeration were done for agglomerates produced by spraying binder. For the first time, the model presented by Rieck et al. [2018] is applicable for binderless agglomeration (spraying only water over amorphous primary particles). Despite of several assumptions used in their simulation, the model is able to correctly describe the influence of process parameters, such as inlet gas temperature and spraying rate, on the agglomeration behavior.

The model developed by Rieck et al. [2018] is based on the Monte Carlo method in the scale of the single particle and can describe the agglomeration process of amorphous particles in a fluidized bed. The deposition of droplets on the particle surface, droplet imbibition, and glass transition were considered in their model. The simulation data was also compared with experimental results obtained for maltodextrin with different DE values [Rieck et al., 2018].

From literature, it is known that process conditions can have a significant influence on the final properties of agglomerates, such as instant properties, flowability and strength, arising from changes in the internal microstructure of the agglomerates. So far, the internal microstructure of agglomerates has rarely been investigated due to measurement difficulties, and such investigations were performed with non-soluble particles. The effect of process parameters on microstructure and morphology of glass bead agglomerates (as non-soluble particles) was thoroughly investigated by Dadkhah and Tsotsas [2014].

The focus of this work is to gain a better understanding of the influence of process parameters on the internal microstructure of the final soft maltodextrin agglomerates. Maltodextrin agglomerates were produced in a spray fluidized bed at different conditions, as summarized in Table 2.2. Agglomerate growth and shape are studied by tracking the evolution of the median diameter, particle size distribution and circularity in order to capture the influence of the varied process parameter. Moreover, with the help of 3D X-ray volume images, the morphological descriptors of agglomerates are discussed in regard to the process conditions used to generate them. The morphological and microstructural characterization is evaluated in terms of sphericity, porosity and fractal dimension. A certain number of agglomerates ranging from 21 to 25 per trial were selected to be scanned individually for the examination of morphological descriptors.

## 6.2 Influence of spraying rate

For the agglomeration of food powders in fluidized beds, the liquid injection rate is an important parameter because viscous liquid layers are required to initiate the adhesion of particles. Due to the sprayed liquid over the particles the glass transition temperature is decreased and the particle surface becomes sticky, which may cause the particles to agglomerate. Depending on the spraying rate, the availability of activated adhesive particle surfaces is limited to smaller or larger regions throughout the bed [Fries et al., 2014]. Therefore, the overall agglomeration rate and the structure of agglomerates are dependent on the amount of liquid spraying during the process. It should be considered that high injection rates lead to an increased relative humidity and consequently a higher risk of bed collapse [Fries et al., 2014]. Moreover, at high injection rate oversize agglomerates are produced

while large portions of the particles remain unagglomerated [Fries et al., 2011]. In our investigation, as it was mentioned in Table 2.2, the spraying rate has been varied in the range of 1.25-2.25 g/min.

### 6.2.1 Size distribution analysis

The effect of binder injection rate on the agglomerate size distribution is investigated by dynamic digital image analysis (Camsizer). Median is the property value exceeded by half of the population, the other half residing below this point. For particle size distributions the median is denoted by  $D_{50}$  and it can be obtained from volume, number or surface area distributions. Usually and also in this study,  $D_{50}$  is the median diameter of the volume distribution. This value is one of the easiest statistical indices to understand and characterize a particle size distribution. The primary particle size distribution is also shown in Fig. 6.1 and has a median diameter of 0.34 mm. It can be observed that at lower spraying rate (1.25 g/min) there are still some primary particles which are not agglomerated. As it is shown in the cumulative volume size distributions of Fig. 6.1, by increasing the rate of binder injection, agglomerate size is increased. The median diameter ( $D_{50}$ ) of agglomerates at 1.25 g/min injection rate is 0.45 mm, whereas it is increased to 0.86 mm at 2.25 g/min. Also, higher binder injection rate leads to a broader size distribution of agglomerates.

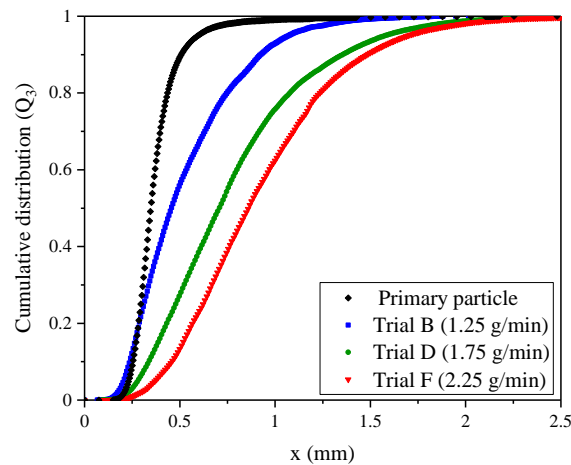


**Figure 6.1:** Cumulative volume size distribution of agglomerates produced at different spraying rates.

This observation is in agreement with Monte Carlo simulations for non-soluble particle agglomerates made with binder solution [Terrazas-Velarde, Peglow, and Tsotsas, 2009; Terrazas-Velarde, Peglow, and Tsotsas, 2011a; Terrazas-Velarde, Peglow, and Tsotsas, 2011b]. Higher spraying rate means more wet spots on the particle surface and higher probability of wet collision. This leads to the formation of more liquid bridges between the particles and allows them to grow to larger sizes within a shorter period of time. For soluble

maltodextrin particles, able to undergo glass transition and sprayed with water, the particle surface stickiness and viscosity are the reason of bridge formation. In this case, at higher spraying rate, more water droplets adhere to the surface of particles and penetrate their supramolecular structure. Therefore, the surface becomes more sticky and viscous because it undergoes glass transition, and finally the agglomeration rate is increased.

For glass bead agglomerates produced in spray fluidized bed, it was shown that by increasing the initial binder mass fraction the particles grow faster and larger agglomerates are produced. Maltodextrin DE12 and DE21 particles with different glass transition temperature were agglomerated at different injection rates by [Avilés-Avilés, Dumoulin, and Turchiuli, 2015] in order to investigate the influence of particle stickiness on agglomerate growth kinetics and mechanism. For maltodextrin DE12, the size and growth rate increased significantly with the sprayed water flow rate but only a small variation was observed for maltodextrin DE21.

For binderless agglomeration, the effect of water spraying rate on maltodextrin agglomerates was modeled in details by Rieck et al. [2018] with Monte Carlo method. Different effects of spraying rate were considered in his modeling and he concluded that the positive influence of increasing spraying rate on the agglomeration rate predominates the negative influence. Therefore, based on his simulation a high spraying rate leads to faster agglomeration, while a lower spraying rate leads to slower agglomeration. The experimental evaluation of the Sauter mean diameter of maltodextrin agglomerates produced at different spraying rate shows similar trend as the simulation data [Rieck et al., 2018].

The association of primary particles into bigger agglomerates can occur either by the progressive incorporation of primary particles into larger agglomerates or by first the formation of initial clusters of primary particles and then the association of these clusters into larger agglomerates. Depending on the agglomeration mechanism, the obtained agglomerates will have different structures, with probably more porous agglomerates obtained in the second case [Avilés-Avilés, Dumoulin, and Turchiuli, 2015].

In our experiments, by investigating the number size distribution (Fig. 6.2), we can notice that at higher injection rate, secondary agglomeration takes place. Three large peaks are visible in the number size distribution at higher injection rate. The first one is associated with primary particles which are not involved in the agglomeration process. The second peak represent intermediate agglomerates of primary particles. The third peak, which appears only at higher binder injection rate, is for the secondary agglomeration, during which the intermediate agglomerates stick together and produce bigger agglomerates. When the water spraying rate is decreased, the transition from the first growth mechanism to the second one is inhibited, so that only few large agglomerates are formed in this case.



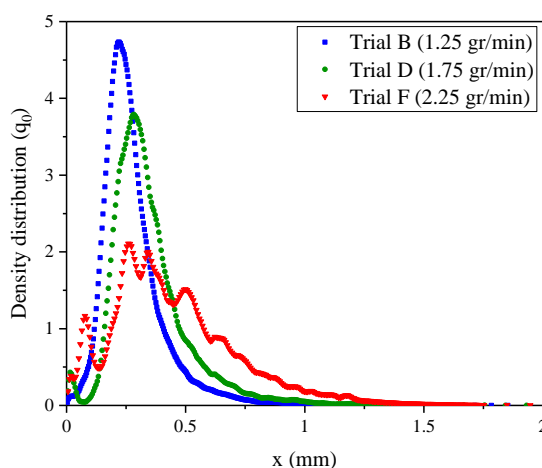


**Figure 6.2:** Number density distribution of the size of agglomerates produced at different spraying rates.

### 6.2.2 Porosity

The internal porosity or closed pores porosity of agglomerates which is not connected to the surface is around 0.18. No significant differences in closed porosity values are found between agglomerates produced at different binder injection rates. The internal porosity in agglomerates mostly belongs to the structure of the primary particles and their porosity. So during the different agglomeration processes this porosity does not change. It should be noted that the resolution of  $\mu$ -CT images was  $2.2 \mu\text{m}$ , therefore it was not feasible to detect pores smaller than  $5.5 \mu\text{m}$ .

In this chapter, the discussion is based on the convex hull method, but results for the two other methods (equivalent radius from gyration radius and dilation, see Chapter 3) are also reported in appendix A. Unlike closed pores, the open pores which are connected to the surrounding air are formed by the agglomeration process, during which the primary particles stick together. Therefore, the process parameters of agglomerates production have an effect on the open pore porosity. Higher values are observed for agglomerates produced at a higher injection rate (Fig. 6.3). As mentioned in Sec. 3.7.3, in general the higher value of the porosity of maltodextrin agglomerates in comparison to the porosity of rigid agglomerates is attributed to the properties of maltodextrin as an amorphous water-soluble substance. The sticky and plasticized surface of maltodextrin during the spraying of water leads to creation of more irregularly shaped porous agglomerates. This stickiness and plasticization are increased at higher spraying rate and consequently result in agglomerates with higher porosity. Therefore, by increasing the injection rate, not only the size of the agglomerates increases, but also their structure becomes more complex with more open pores (Fig. 6.4). To achieve good instant properties, agglomerate structures with open pores are desirable, because they allow quick penetration of water into the particle matrix [Fries et al., 2014].

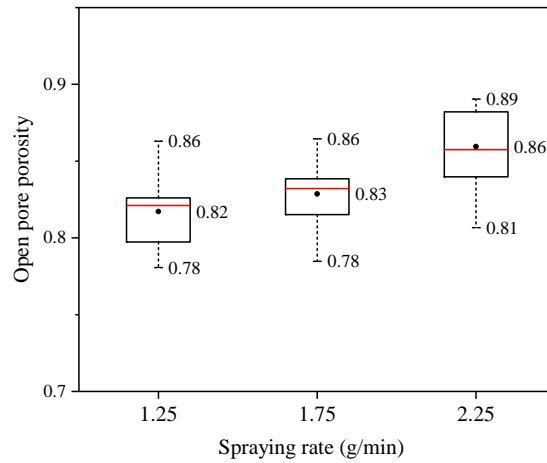


**Figure 6.3:** Open porosity of agglomerates produced at different spraying rates.

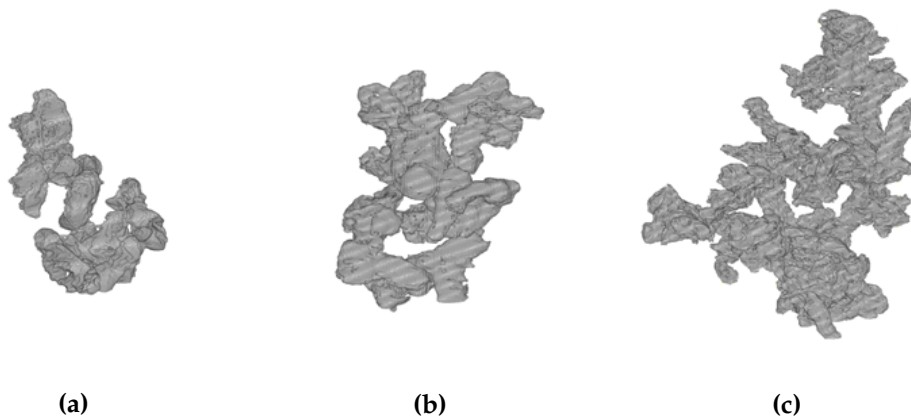


**Figure 6.4:** 3D view of maltodextrin agglomerates produced at different spraying rates (g/min): (a) 1.25, (b) 1.75, (c) 2.25.

The porosity of glass bead agglomerates was found to moderately increase at higher binder mass fraction, which is due to generation of more viscous bridges [Dadkhah and Tsotsas, 2014]. It was shown that by increasing the mass fraction of HPMC binder from 2% up to 10%, the porosity of agglomerates increased from 0.53 to 0.63. Investigations with granules made of pharmaceutical excipients show a similar trend of porosity values by increasing the binder concentration (hydroxypropyl-cellulose (HPC) in water solution) [Rajniak et al., 2007]. In our study, only pure water was sprayed over the particles, so that increasing the concentration of binder had no relevance. Therefore, only the influence of spraying rate on agglomerate morphology has been investigated.

The bulk porosity of agglomerates which are packed in a cylindrical tube (Sec. 3.7.4) increases at higher water injection rate in the spray fluidized bed. The bulk porosity of agglomerates which are produced at different binder injection rate is shown in Fig. 6.5. One can see that the bulk porosity of primary particles is around 0.60, whereas it increases

to 0.85 for agglomerates produced at the highest binder injection rate.

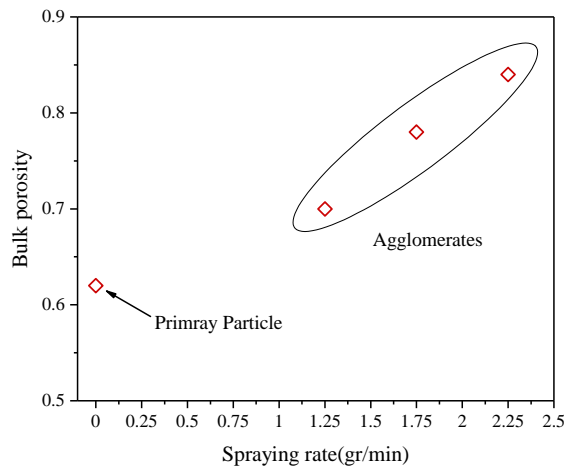


**Figure 6.5:** Bulk porosity of primary particles and agglomerates produced at different spraying rates.

### 6.2.3 Circularity and sphericity

The circularity of agglomerates produced at different binder injection rates was investigated by Camsizer for 2D images. As shown in Fig. 6.6, the trend for circularity is same for all agglomerates and there is not any large difference in circularity values by changing the injection rate. By X-ray  $\mu$ -CT investigation, the sphericity can be obtained from 3D images. The value of sphericity for agglomerates produced at different spraying rate also does not change noticeably. The mean value of sphericity for agglomerates produced at lowest spraying rate (1.25 g/min) is 0.17, and this value is increased only slightly up to 0.19 for agglomerates at 1.75 g/min injection rate. The sphericity value at the highest injection rate (2.25 g/min) is decreased to 0.15, which indicates that agglomerates become more complex and irregular (Fig. 6.7).

### 6.2.4 Fractal dimension

Table 6.1 illustrates that by increasing the binder spraying rate from trial B to trial D and trial F the fractal dimension decreases. This would mean that the majority of agglomerates produced at higher binder spraying rate are less compact and fill the space loosely. When the agglomeration rate is high, primary particles stick together too rapidly in different directions and there is not enough time to make a compact and dense structure. This observation is also in agreement with the increase in porosity at higher spraying rate. A low fractal dimension is associated with agglomerates having dendritic arms and hence a high porosity. For simulated agglomerates it was also reported by Sommerfeld and Stübing

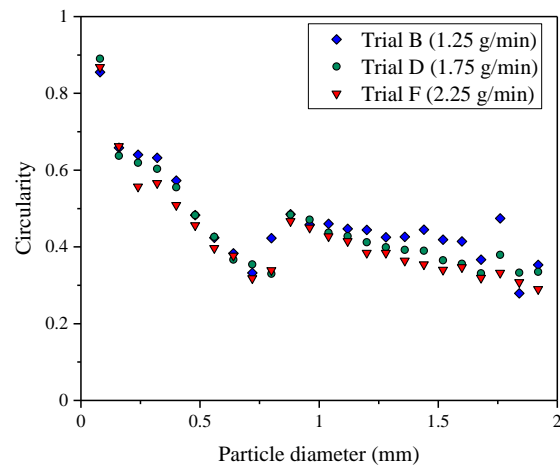


Figure 6.6: Circularity of agglomerates produced at different spraying rates.

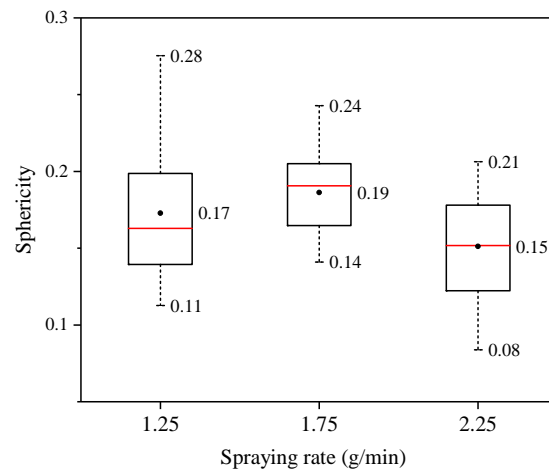


Figure 6.7: Sphericity of agglomerates produced at different spraying rates.

[2017] that when the fractal dimension is in the range of 1.7 up to 2.3, the porosity value from convex hull is quite high, i.e. has a mean value of about 0.7. When the fractal dimension approaches 3 (compact sphere) expectedly the porosity reaches to zero. In the work of Dadkhah and Tsotsas [2014] the same trend as in this study was reported for the fractal dimension when increasing the binder mass fraction.

The prefactor value shows opposite trend compared to the fractal dimension and it increases when the agglomerates are produced at higher spraying rate. As it was mentioned in Chapter 5, the prefactor is an indicator of local structure, and sintering of primary particles during agglomeration has noticeable influence on it. At higher spraying rate, also due to higher amount of absorbed water by primary particles, sintering plays a bigger role in the agglomeration process and results in higher values of the fractal prefactor.

## 6.3 Influence of process temperature

The other important parameter that has influence on the agglomeration process is the process temperature. For the agglomeration of amorphous water soluble particles, usually two opposite effects are expected. At higher process temperature, the evaporation of water from the surface of primary particles takes place more rapidly. Therefore, the plasticized area on the particle will dry out faster. Additionally, a possibly larger fraction of the injected spray droplets will dry out even before deposition on a particle, which should decrease the aggregation rate. On the other hand, the glass transition temperature of amorphous particles is an important factor for stickiness. If the operating temperature is increased, a larger amount of particles will undergo glass transition and may potentially form agglomerates, which should increase the aggregation rate. The influence of the inlet gas temperature on the parameters of the agglomeration criteria is discussed in detail by Rieck et al. [2018] for binderless agglomeration (spraying only water). In that work with the help of Monte Carlo simulations the influence of temperature on the number of droplets (wet positions) in the particle system, and the evolution of the water mass fraction, the glass transition temperature, and the viscosity of a wet spot during drying for different inlet gas temperatures were shown and discussed.

In our investigation agglomerates were also produced at different temperatures which are listed in Table 2.2. As it can be seen, the value of process temperature was changed for each spraying rate. It is not possible to change the temperature too much because at too high temperature no agglomerates are produced and most of the sprayed water is evaporated before reaching the surface of particle; when the temperature is too low, the bed collapses due to overwetting of the entire bed.

### 6.3.1 Size distribution analysis

Based on the size distribution of agglomerates produced at different temperatures, it is noticed that with increasing temperature the agglomeration rate is decreased and smaller agglomerates are produced (Fig. 6.8). This observation shows that for maltodextrin agglomerates produced under the investigated conditions, the main effect of temperature is related to its role in evaporating water droplets and making the sticky zones on the particles to be dried faster. As seen in Fig. 6.8 for both series of agglomerates produced at different spraying rates, when the temperature is decreased, the agglomeration rate is increased and bigger agglomerates are produced. The same is also observed for agglomerates of trials C, D and E which have been produced at constant spraying rate of 1.75 g/min with different process temperatures ranging from 45 to 55 °C; (the median diameter is reported in Table 6.1).

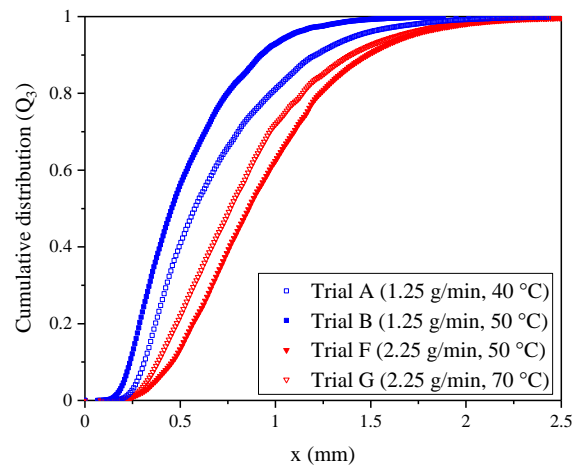


**Figure 6.8:** Cumulative volume size distribution of agglomerates produced at different temperatures.

The same observation from experimental work was reported by Dadkhah and Tsotsas [2014] for glass bead agglomerates, that by increasing the inlet air temperature the agglomeration rate was decreased. The relation between gas temperature and agglomeration rate has been explained by Terrazas-Velarde, Peglow, and Tsotsas [2011a] with the help of Monte Carlo simulations of spray fluidized bed agglomeration. It should be noted that in both mentioned works the binder was sprayed over rigid primary particles that did not undergo glass transition. But as it was mentioned before in principle for amorphous particles, process temperature has two contrary influences on agglomeration rate due to glass transition. It was shown by Rieck et al. [2018] for maltodextrin particles that a low temperature leads to faster agglomeration, while a high temperature consequently leads to slower agglomeration. This trend was observed in both the experimental and simulation results of each maltodextrin with DE 6, 12, 47. Avilés-Avilés, Dumoulin, and Turchiuli [2015] show that in general the size of maltodextrin agglomerates is increased by decreasing the temperature. When comparing the size increase for two kinds of maltodextrin, different effects of the air temperature were obtained. They reported that, due to the different glass transition temperature, for maltodextrin DE 12 the size increase was lower than for maltodextrin DE 21 [Avilés-Avilés, Dumoulin, and Turchiuli, 2015]. Eventually, from our investigation and the reported values of simulation and experimental data, it can be concluded that the negative influence of high temperature on maltodextrin agglomeration rate prevail. The experimental results by Fries et al. [2013] for dextrose syrup DE21 also show that the Sauter mean diameter decreases in all the spray, spouted and Wurster fluidized beds, if the operating temperature is increased. This shows that the drying rate is the limiting factor for the growth kinetics of dextrose syrup under the given process conditions.

### 6.3.2 Porosity

For the same reason as mentioned in Sec. 6.2.2, no changes are observed in the internal porosity of agglomerates produced at different temperatures. Fig. 6.9 represents the open porosities by convex hull method for agglomerates produced at different fluidizing temperatures. It is evident from the figure that porosity of the agglomerates decreases with increasing air temperature. For example, at constant spraying rate of 1.75 g/min (Fig. 6.9a), when the process temperature is increased from 45 to 55 °C, the mean porosity decreases by almost 8%. At higher fluidizing air temperature, sessile droplets of water dry out quickly from the surface of particles. Therefore, the probability of successful collision of the particle to form an agglomerate is lower. Consequently, agglomerates produced at higher fluidizing air temperature are more compact with less porosity.

The same behavior is also observed when changing the process temperature of agglomeration at lower or high spraying rate (Figs. 6.9b and 6.9c). At higher injection rate (2.25 g/min) temperature increase by 20 °C (from 50 °C to 70 °C) results in less decrease in porosity than 10 °C temperature increase (from 40 °C to 50 °C) at low injection rate (1.25 g/min). In general, it is difficult to change the porosity value dramatically by changing only the process parameters. The value of porosity also depends on primary particle properties and the apparatus used to produce the agglomerates. In the work of Dadkhah and Tsotsas [2014] on glass bead agglomerates, the maximum decrease in porosity value is 14%, which was obtained by increasing the temperature by almost 60 °C. Due to the random nature of the agglomeration and fluidization process, the fluidized bed agglomerates are very irregular and highly porous. When the primary particles also have amorphous structure, the irregularity and porosity are increased noticeably. Three different configurations of fluidized bed (top-spray, Wurster-coater and spouted bed) were studied and the results show that the most stable, compact and dense agglomerates are achieved using the spouted bed [Fries et al., 2013]. Much more compact agglomerates with lower porosity as compared to fluidized bed agglomerates can be produced by pressure agglomeration, e.g., by the roller compacting method.

### 6.3.3 Sphericity

Variation of fluidization air temperature has more effect on sphericity in comparison to spraying rate. The sphericity is decreased considerably at a lower temperature. For agglomerates produced at constant spraying rate of 1.75 g/min, as shown in Fig. 6.10a the mean value of sphericity of agglomerates produced at production temperature of 45 °C is 0.10 which is increased up to 0.20 for agglomerates produced at 55 °C. At a lower spraying rate (1.25 g/min) also the mean value of sphericity at 40 °C is also 0.10 (Fig. 6.9b). Producing agglomerates at a temperature lower than 50 °C with high spraying rate (2.25 g/min) was not

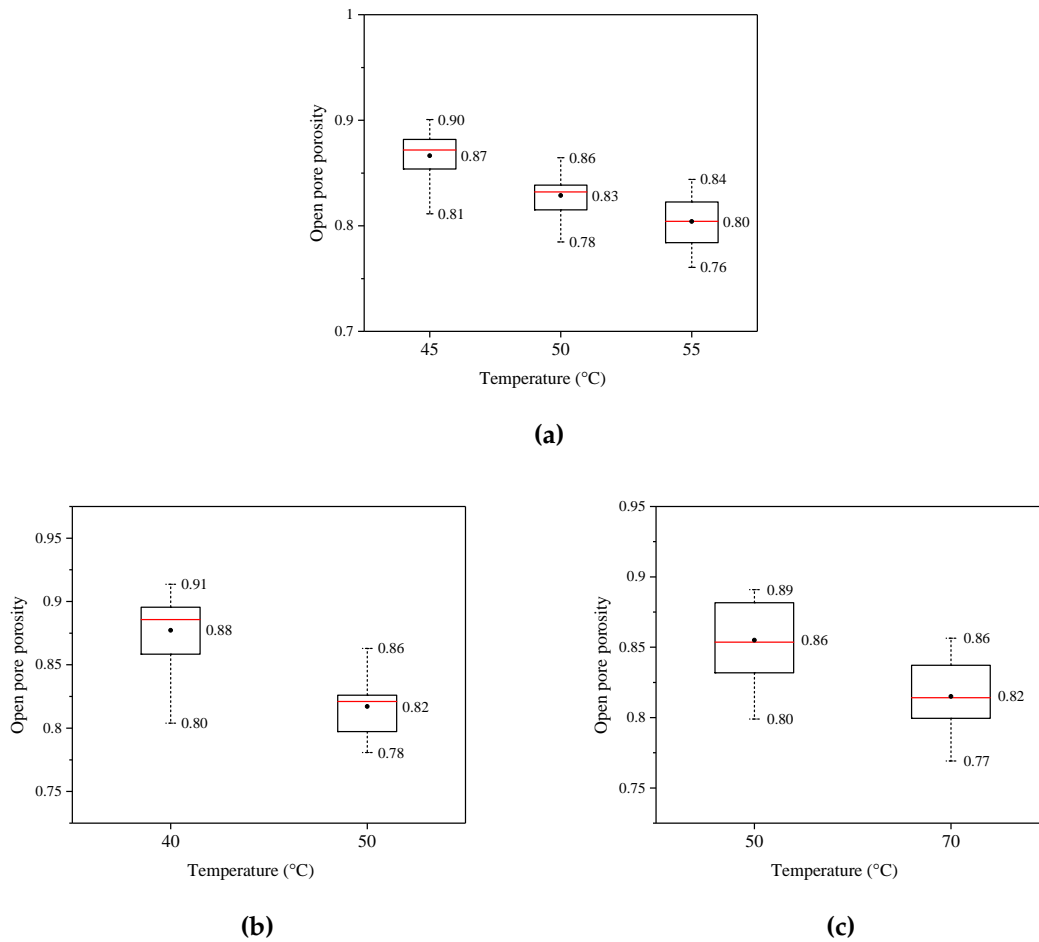


**Figure 6.9:** Open pore porosity of agglomerates produced at different inlet air temperatures and constant spraying rate of (g/min): (a) 1.75, (b) 1.25, (c) 2.25.

possible, due to overwetting of the bed and collapsing phenomena. Therefore, experiments with this spraying rate were only carried out at 50 and 70 °C. The value of sphericity for these two temperatures does not change noticeably and only a minor increase is observed at 70 °C (Fig. 6.10c). The lower values of sphericity at lower temperatures are related to high agglomeration rate, which results in more irregularly structured particles. In general, the low values of sphericity measured for fluidized bed agglomerates of maltodextrin (ranging between 0.10 and 0.20) show that the overall structure of the agglomerates deviates considerably from a sphere with the same volume. Low value of sphericity is the main feature of fluidized bed agglomerates especially of agglomerates made of soft material. Hafsa et al. [2014] also observed that grain granules which were produced under low shear conditions during the mixing step had low values of sphericity (0.20-0.23), while industrial granules produced at high shear condition have sphericity in the range of 0.40-0.45. Higher values of sphericity (0.78-0.87) were reported for granules produced by a twin screw extruder or high shear mixer [Lee, Ingram, and Rowson, 2013].



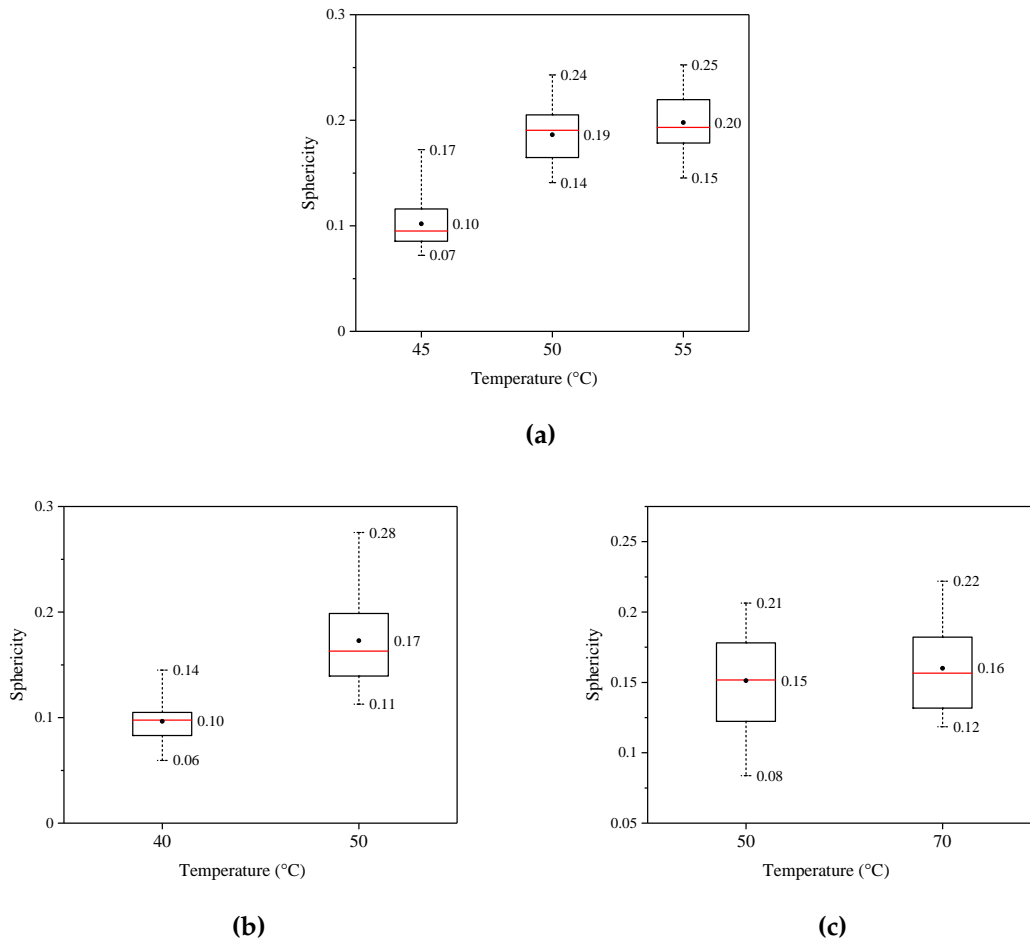


**Figure 6.10:** Sphericity of agglomerates produced at different inlet air temperatures and constant spraying rate of (g/min): (a) 1.75, (b) 1.25, (c) 2.25.

### 6.3.4 Fractal dimension

As it was discussed in Chapter 5, the fractal dimension can be investigated based on monodisperse or polydisperse separated primary particles, and it can also be obtained from voxel data. Polydisperse separated primary particles is the more proper method by considering the estimation time. In Table 6.1, the values for fractal dimension and prefactor are reported based on polydisperse primary particles, where the mean radius of primary particles has been the number average of primary particle radii in 13 discrete directions. By increasing the temperature from 45°C (Trial C) to 55°C (Trial E), the fractal dimension value increases from 1.64 to 1.91. This would mean that the majority of agglomerates made at high temperature (e.g. at 55 °C in case of Trial E) are much denser and more space filling, containing more primary particles in the same length. The main reason for this trend is higher agglomeration rate at lower temperature. Agglomerates produced at higher agglomeration rate have more open and fluffy structure, while on the other hand agglomerates produced at lower agglomeration rate tend to create a more closely packed structure. The fractal dimension of glass bead agglomerates also shows a similar trend with increasing production

temperature [Dadkhah and Tsotsas, 2014]. Ku and Maynard [2006] reported 2D projected fractal dimensions for agglomerates of silver nanoparticles in the size ranging from 20 to 100 nm at different temperatures. In their work, the fractal dimension is also increased at higher temperature, which is mostly due to the higher ratio of sintering of primary particles during the agglomeration process. Some research works stress the importance of the effect of temperature on agglomerate structure. Weber et al. [1996] claimed that it is possible to produce agglomerates of a well-defined fractal dimension by carefully adjusting the temperature. In the case of amorphous particles agglomerating in a spray fluidized bed, due to the two competing effects of temperature on agglomeration rate, finding a simple and generally valid relation between temperature and fractal dimension is a challenging issue. Moreover, variation of the temperature is limited due to the collapse of the fluid bed at lower temperature and no agglomeration at higher temperature. Therefore, it is difficult to produce amorphous agglomerates with specified structure only by optimizing the temperature.

Regarding the prefactor value, there is no specified trend of decreasing or increasing obtained by changing the temperature. According to the previous section (Sec. 6.2.4) increasing the spraying rate causes a decrease in fractal dimension and an increase in prefactor. It means that prefactor and fractal dimension change in opposite direction. In that case, increasing prefactor is mainly due to more sintering and overlapping of primary particles at higher injection rate. However, at lower temperature although the agglomeration rate is increased, no more sintering happens necessarily. Therefore, when the fractal dimension is decreased, an increase of the prefactor should not be expected.

**Table 6.1:** Evaluated morphological descriptors for agglomerates produced at different process conditions.

Trial	A	B	C	D	E	F	G
Gas inlet temperature (°C)	40	50	45	50	55	50	70
Spraying rate (g/min)	1.25	1.25	1.75	1.75	1.75	2.25	2.25
Median diameter (mm)	0.578	0.453	0.825	0.703	0.605	0.862	0.763
Average porosity	0.88	0.82	0.87	0.83	0.80	0.86	0.82
Sphericity	0.10	0.17	0.10	0.19	0.20	0.15	0.16
Fractal dimension	1.74	2.04	1.64	1.82	1.91	1.60	1.82
Prefactor	3.52	2.74	3.83	2.85	3.29	3.12	3.72

## Chapter 7

# Conclusion and outlook

### 7.1 Conclusion

The present work provided a comprehensive characterization of the internal structure of maltodextrin agglomerates produced in spray fluidized bed by means of X-ray micro tomography. This technique gave the opportunity to completely visualize and quantify the internal structure of such agglomerates in 3D at scales down to the micron level. Then, by a series of image processing steps performed on the X-ray images, the porosity of single agglomerates was calculated in terms of closed pores and open pores. The bulk porosity of the packed bed was also investigated for maltodextrin particles before and after agglomeration. The sphericity of maltodextrin agglomerates with an irregular structure was calculated based on the volume and surface area obtained from the 3D X-ray images. Sphericity was compared to the circularity of agglomerates obtained from an analysis of 2D images acquired by a Camsizer. The rather large difference of these two values was first explained by differences in the image resolution between the two techniques. Second, for irregular particles, the 2D image analysis gives only partial information on the shape, whereas 3D image analysis allows the measurement of the true characteristics of the particles.

The separation of the primary particles of maltodextrin with non-spherical shape was done by an improved preflooded watershed segmentation method. In order to separate the primary particles of the agglomerate in a reasonable way, the suitable minimal pixel number was found for this kind of agglomerates, which exhibit a complex structure. Based on the information obtained from separated primary particles, the radius of gyration, the fractal dimension, coordination number, coordination angle and radial distribution of primary particles were calculated for a series of agglomerates.

Overall features of 3D morphological descriptors such as high porosity value, low value of the fractal dimension and sphericity, low mean coordination number and sparse radial distribution of primary particles proved that maltodextrin agglomerates produced in a

spray fluidized bed have irregular, open and fluffy structure with relatively unstable arrangement. Moreover, the results show that coordination number, coordination angle and open pore porosity are rather independent of the size of agglomerates and the number of primary particles involved.

This research work also aimed at a better understanding of the internal microstructure of agglomerates evaluated by either the simplified spherical primary particle model (SPPM) or the real structure model (RSM) for maltodextrin agglomerates produced in a spray fluidized bed. The data for RSM was obtained by post processing of X-ray micro tomography images, whereas the spherical model was established by considering each irregular primary particle as a sphere.

The results of coordination number for the two models are different, and it was observed that by simplifying the irregular shape of primary particles to spheres the accuracy of contact point detection is not preserved. Coordination angles show differences because they depend on the coordination points in the two models. The values of open pore porosity which were calculated based on the radius of gyration are almost identical for the two models. However, higher values of open pore porosity are obtained from the RSM if the convex hull method is used. The radial distribution of primary particles is identical for both models, because it only depends on the center coordinates of primary particles which are exactly the same for the two cases.

In general, it can be concluded that if the shape of primary particles in agglomerates deviates too much from spherical, the simplified SPPM does not provide precise results of microstructural characterization. This has appreciable influence on characterization features like the coordination number, which depends significantly on the shape of primary particles. Therefore, 3D morphological studies of complex agglomerate structures made of soft material, such as maltodextrin, should be carried out based on the real structural information which can be obtained by X-ray tomography scanning.

In this research, the radius of gyration and fractal dimension were calculated by separating primary particles in the agglomerates, which can be considered as a simplified method. Alternatively, these morphological descriptors of the real structure were deduced directly from voxel information. The obtained values for radius of gyration and fractal dimension from the voxel information are more accurate, but more time and effort is needed to extract the data of each voxel and implement them in the calculation process. Moreover, due to considering each voxel as a primary particle, a high and unrealistic value for the fractal prefactor is obtained. Therefore, the estimation process based on separated primary particles can be seen as a suitable alternative method. Although this method may cause some error, an easier implementation makes it to a proper choice for cases in which the value of fractal dimension is not needed with high precision. For this method, the identification of primary particles in a 3D X-ray image is crucial.

The radius of gyration for separated primary particles was calculated and compared considering two assumptions: monodisperse or polydisperse particles. For most of the agglomerates the gyration radius value from monodisperse assumption is higher than in the polydisperse case, with an average difference of around 14%. Due to the relatively broad size distribution of maltodextrin primary particles, calculating the radius of gyration by means of the polydisperse model is highly recommended and can be achieved without much more effort than for the monodisperse model.

Fractal dimension and prefactor were obtained from the power law equation, in which the radius of primary particles should be defined properly. The radius of each irregular primary particle of maltodextrin was assumed as corresponding to either the ball radius of equal volume or to the mean value of radii reported in 13 discrete directions. Due to the large mean value of discrete radii, the ratio of overlapping and virtual sintering of primary particles is high in this case, which increases significantly the prefactor while the fractal dimension decreases only slightly. This observation indicated that the large scale distribution of primary particles is mainly determined by fractal dimension, whereas the fractal prefactor describes local primary particle distribution. It is difficult to conclude which assumption is more appropriate in our case, because in literature very wide ranges are reported for prefactor values. Also, there is a lack of data for fractal prefactors of amorphous agglomerates, so that the present prefactor results from the mentioned two assumptions cannot directly be compared to any other results for experimental or simulated agglomerates.

Moreover, the proper implementation of the box-counting method as another option for calculating the fractal dimension was investigated. Identification of primary particles can be avoided in the box counting method, but the value of fractal dimension obtained by this method differs markedly from the results calculated by the power law method. This discrepancy is expectable due to different concepts behind these two methods.

Results show that the operating conditions of the production process have an influence on the internal morphology of the agglomerates produced. It was shown that agglomeration rate was increased by decreasing the inlet air temperature or by increasing the spraying rate. At high agglomeration rates, the fractal dimension and sphericity are low whereas agglomerate porosity and the fractal prefactor are relatively high. Consequently, a looser, open structure and fluffier agglomerates are obtained. On contrary, fractal dimension and sphericity are higher at low agglomeration rate, whereas agglomerate porosity and the prefactor are lower. This means that agglomerates produced under these conditions have a more compact and denser structure.

The present work demonstrates the ability of the X-ray  $\mu$ -CT method to describe the 3D morphology and the internal microstructure of food agglomerates. The most serious limitation concerns the time and effort necessary for measurement and, especially, for image processing, which limits the number of agglomerates that can be analyzed and assessed.

## 7.2 Outlook

In this work only the influence of main process parameters (temperature and spraying rate) on the morphology of the agglomerates was studied. In future work, the other parameters which have been kept constant during the agglomeration process could be varied, and their influence on the structure of the produced agglomerates could be studied. Studying the structure of maltodextrin agglomerates produced only by sintering at higher temperature (without spraying water) would also be an interesting topic. Moreover, maltodextrin with different DE values also can be used in agglomeration process to understand the effect of DE on the structure of the final product.

Open porosity is an important parameter that has noticeable influence on the instant properties of agglomerates. A comprehensive study over the effect of open pores on dispersing and dissolution of the agglomerates could be done by analysing the size distribution of these pores. The long term vision is to link the morphology of particulate materials with the process conditions on one side and with their end-user properties (e.g. strength, flowability, compressibility, instant properties) on the other side. The presented morphological characterization is an essential step along this path.

# Bibliography

- Ai, T., R. Zhang, H. W. Zhou, and J. L. Pei. "Box-counting methods to directly estimate the fractal dimension of a rock surface". In: *Applied Surface Science* 314 (2014), pp. 610–621.
- Asahina, D. and M. A. Taylor. "Geometry of irregular particles: Direct surface measurements by 3-D laser scanner". In: *Powder Technology* 213.1-3 (2011), pp. 70–78.
- Avilés-Avilés, C., E. Dumoulin, and C. Turchiuli. "Fluidised bed agglomeration of particles with different glass transition temperatures". In: *Powder Technology* 270 (2015), pp. 445–452.
- Bagheri, G., C. Bonadonna, I. Manzella, and P. Vonlanthen. "On the characterization of size and shape of irregular particles". In: *Powder Technology* 270 (2014), pp. 141–153.
- Baker, D. R., L. Mancini, M. Polacci, M. D. Higgins, G. A. R. Gualda, R. J. Hill, and M. L. Rivers. "An introduction to the application of X-ray microtomography to the three-dimensional study of igneous rocks". In: *Lithos* 148 (2012), pp. 262–276.
- Barbosa-Cánovas, G. V., E. Ortega-Rivas, P. Juliano, and H. Yan. *Food Powders: Physical Properties, Processing, and Functionality*. New York: Kluwer Academic/Plenum Publishers, 2005.
- Barkouti, A., C. Turchiuli, J. A. Carcel, and E. Dumoulin. "Milk powder agglomerate growth and properties in fluidized bed agglomeration". In: *Dairy Science and Technology* 93.4-5 (2013), pp. 523–535.
- Belaid, L. J. and W. Mourou. "Image segmentation: A watershed transformation algorithm". In: *Image Analysis and Stereology* 28.2 (2009), pp. 93–102.
- Bhandari, B. R. and T. Howes. "Implication of glass transition for the drying and stability of dried foods". In: *Journal of Food Engineering* 40.1 (1999), pp. 71–79.
- Bleau, A. and L. Leon. "Watershed-based segmentation and region merging". In: *Computer Vision and Image Understanding* 77.3 (2000), pp. 317–370.
- Blott, S. J. and K. Pye. "Particle shape: A review and new methods of characterization and classification". In: *Sedimentology* 55.1 (2008), pp. 31–63.
- Boas, F. and D. Fleischmann. "CT artefacts: Causes and reduction techniques". In: *Imaging in Medicine* 4.2 (2012), pp. 229–240.

- Börjesson, E., F. Innings, C. Trägårdh, B. Bergenståhl, and M. Paulsson. "Evaluation of particle measures relevant for powder bed porosity: A study of spray dried dairy powders". In: *Powder Technology* 253 (2014), pp. 453–463.
- Brasil, A. M., T. L. Farias, and M. G. Carvalho. "A recipe for image characterization of fractal-like aggregates". In: *Journal of Aerosol Science* 30.10 (1999), pp. 1379–1389.
- Brasil, A. M., T. L. Farias, and M. G. Carvalho. "Evaluation of the fractal properties of cluster-cluster aggregates". In: *Aerosol Science and Technology* 33.5 (2000), pp. 440–454.
- Brasil, A. M., T. L. Farias, M. G. Carvalho, and U. O. Koylu. "Numerical characterization of the morphology of aggregated particles". In: *Journal of Aerosol Science* 32.4 (2001), pp. 489–508.
- Bück, A. and E. Tsotsas. "Agglomeration". In: *Encyclopedia of Food and Health*. Elsevier, 2016, pp. 73–81.
- Califice, A., F. Michel, G. Dislaire, and E. Pirard. "Influence of particle shape on size distribution measurements by 3D and 2D image analyses and laser diffraction". In: *Powder Technology* 237 (2013), pp. 67–75.
- Chakrabarty, R. K., H. Moosmüller, M. A. Garro, W. Patrick Arnott, J. G. Slowik, E. S. Cross, J. H. Han, P. Davidovits, T. B. Onasch, and D. R. Worsnop. "Morphology based particle segregation by electrostatic charge". In: *Journal of Aerosol Science* 39.9 (2008), pp. 785–792.
- Chronakis, I. S. "On the molecular characteristics, compositional properties, and structural-functional mechanisms of maltodextrins : A review". In: *Critical Reviews in Food Science and Nutrition* 38.7 (1998), pp. 599–637.
- Cierniak, R. *X-ray Computed Tomography in Biomedical Engineering*. London: Springer, 2011.
- Cormack, A. M. "Representation of a function by its line integrals, with some radiological applications. II". In: *Journal of Applied Physics* 35.10 (1964), pp. 2908–2913.
- Cuq, B., S. Mandato, R. Jeantet, K. Saleh, and T. Ruiz. "Agglomeration/granulation in food powder production". In: *Handbook of Food Powders* (2013), pp. 150–177.
- Dadkhah, M. "Morphological characterization of agglomerates produced in a spray fluidized bed by X-ray tomography". PhD thesis. Otto-von-Guericke-University of Magdeburg, 2014.
- Dadkhah, M., M. Peglow, and E. Tsotsas. "Characterization of the internal morphology of agglomerates produced in a spray fluidized bed by X-ray tomography". In: *Powder Technology* 228 (2012), pp. 349–358.
- Dadkhah, M. and E. Tsotsas. "Influence of process variables on internal particle structure in spray fluidized bed agglomeration". In: *Powder Technology* 258 (2014), pp. 165–173.



- Davis, G. R. and J. C. Elliott. "Artefacts in X-ray microtomography of materials". In: *Materials Science and Technology* 22.9 (2006), pp. 1011–1018.
- De Martín, L., A. Fabre, and J. Ruud van Ommen. "The fractal scaling of fluidized nanoparticle agglomerates". In: *Chemical Engineering Science* 112 (2014), pp. 79–86.
- Dernedde, M., M. Peglow, and E. Tsotsas. "Stochastic modeling of fluidized bed granulation: Influence of droplet pre-drying". In: *Chemical Engineering and Technology* 34 (2011), pp. 1177–1184.
- Dernedde, M., M. Peglow, and E. Tsotsas. "A novel, structure-tracking Monte Carlo algorithm for spray fluidized bed agglomeration". In: *AIChE Journal* 58 (2012), pp. 3016–3029.
- Descamps, N., S. Palzer, Y. H. Roos, and J. J. Fitzpatrick. "Glass transition and flowability/caking behaviour of maltodextrin DE 21". In: *Journal of Food Engineering* 119.4 (2013), pp. 809–813.
- Dietzel, M. and M. Sommerfeld. "Numerical calculation of flow resistance for agglomerates with different morphology by the Lattice-Boltzmann method". In: *Powder Technology* 250 (2013), pp. 122–137.
- Dopfer, D., S. Palzer, S. Heinrich, L. Fries, S. Antonyuk, C. Haider, and A. D. Salman. "Adhesion mechanisms between water soluble particles". In: *Powder Technology* 238 (2013), pp. 35–49.
- Eggersdorfer, M. L. and S. E. Pratsinis. "The structure of agglomerates consisting of poly-disperse particles". In: *Aerosol Science and Technology* 46.3 (2012), pp. 347–353.
- Eggersdorfer, M. L., D. Kadau, H. J. Herrmann, and S. E. Pratsinis. "Aggregate morphology evolution by sintering: Number and diameter of primary particles". In: *Journal of Aerosol Science* 46 (2012), pp. 7–19.
- Eggersdorfer, M. L., D. Kadau, H. J. Herrmann, and S. E. Pratsinis. "Multiparticle sintering dynamics: From fractal-like aggregates to compact structures". In: *Langmuir* 27.10 (2011), pp. 6358–6367.
- Elliott, J. C. and S. D. Dover. "X-ray microtomography". In: *Journal of Microscopy* 126 (1982), pp. 211–213.
- Farber, L., G. Tardos, and J. N. Michaels. "Use of X-ray tomography to study the porosity and morphology of granules". In: *Powder Technology* 132.1 (2003), pp. 57–63.
- Foroutan-pour, K, P Dutilleul, and D. L. Smith. "Advances in the implementation of the box-counting method of fractal dimension estimation". In: *Applied Mathematics and Computation* 105.2-3 (1999), pp. 195–210.

- Fox, T. G. and P. J. Flory. "Second-order transition temperatures and related properties of polystyrene. Part 1: Influence of molecular weight". In: *Journal of Applied Physics* 21.6 (1950), pp. 581–591.
- Fries, L., S. Antonyuk, S. Heinrich, and S. Palzer. "DEM-CFD modeling of a fluidized bed spray granulator". In: *Chemical Engineering Science* 66.11 (2011), pp. 2340–2355.
- Fries, L., S. Antonyuk, S. Heinrich, D. Dopfer, and S. Palzer. "Collision dynamics in fluidised bed granulators: A DEM-CFD study". In: *Chemical Engineering Science* 86 (2013), pp. 108–123.
- Fries, L., S. Antonyuk, S. Heinrich, G. Niederreiter, and S. Palzer. "Product design based on discrete particle modeling of a fluidized bed granulator". In: *Particuology* 12 (2014), pp. 13–24.
- Garboczi, E. J., X. Liu, and M. a. Taylor. "The 3-D shape of blasted and crushed rocks: From 20  $\mu\text{m}$  to 38 mm". In: *Powder Technology* 229 (2012), pp. 84–89.
- Gordon, M. and J. S. Taylor. "Ideal copolymers and the second-order transitions of synthetic rubbers. I. Non-crystalline copolymers". In: *Journal of Applied Chemistry*. 2 (1952), pp. 493–500.
- Hadzieva, E., D. C. Bogatinoska, L. Gjergjeska, M. Shuminoska, and R. Petroski. "Review of the Software Packages for Estimation of the Fractal Dimension". In: *ICT Innovations* (2015), pp. 201–211.
- Hafsa, I., S. Mandato, T. Ruiz, P. Schuck, R. Jeantet, S. Mejean, S. Chevallier, and B. Cuq. "Impact of the agglomeration process on structure and functional properties of the agglomerates based on the durum wheat semolina". In: *Journal of Food Engineering* 145 (2015), pp. 25–36.
- Hafsa, I., B. Cuq, S. J. Kim, A. Le Bail, T. Ruiz, and S. Chevallier. "Description of internal microstructure of agglomerated cereal powders using X-ray microtomography to study of process-structure relationships". In: *Powder Technology* 256 (2014), pp. 512–521.
- Hassanpour, A., S. J. Antony, and M. Ghadiri. "Modeling of agglomerate behavior under shear deformation: Effect of velocity field of a high shear mixer granulator on the structure of agglomerates". In: *Advanced Powder Technology* 18.6 (2007), pp. 803–811.
- Hogekamp, S. and M. Pohl. "Porosity measurement of fragile agglomerates". In: *Powder Technology* 130.1-3 (2003), pp. 385–392.
- Hussain, M., J. Kumar, and E. Tsotsas. "Modeling aggregation kinetics of fluidized bed spray agglomeration for porous particles". In: *Powder Technology* 270 (2015), pp. 584–591.

- Hussain, M., J. Kumar, M. Peglow, and E. Tsotsas. "Modeling spray fluidized bed aggregation kinetics on the basis of Monte-Carlo simulation results". In: *Chemical Engineering Science* 101 (2013), pp. 35–45.
- Ibaseta, N. and B. Biscans. "Fractal dimension of fumed silica: Comparison of light scattering and electron microscope methods". In: *Powder Technology* 203.2 (2010), pp. 206–210.
- Kak, A. C. and M. Slaney. *Principles of Computerized Tomographic Imaging*. New York: IEEE Press, 1988.
- Kearsly, M. and S. Dziedzic. *Handbook of Starch Hydrolysed Products and their Derivatives*. Glasgow: Blackie Academic Professional, 1995.
- Köylü, Ü. Ö., Y. C. Xing, and D. E. Rosner. "Fractal morphology analysis of combustion-generated aggregates using angular light scattering and electron microscope images". In: *Langmuir* 11.12 (1995), pp. 4848–4854.
- Ku, B. K. and A. D. Maynard. "Generation and investigation of airborne silver nanoparticles with specific size and morphology by homogeneous nucleation, coagulation and sintering". In: *Journal of Aerosol Science* 37.4 (2006), pp. 452–470.
- Kumar, J., M. Peglow, G. Warnecke, and S. Heinrich. "An efficient numerical technique for solving population balance equation involving aggregation, breakage, growth and nucleation". In: *Powder Technology* 182.1 (2008), pp. 81–104.
- Lagarrigue, M., J. Debayle, S. Jacquier, F. Gruy, and J. C. Pinoli. "Geometrical characterization of various shaped 3D-aggregates of primary spherical particules by radial distribution functions". In: *Image Analysis and Recognition*. Ed. by A. Campilho and M. Kamel. Berlin, Heidelberg: Springer, 2010, pp. 434–443.
- Lapuerta, M., R. Ballesteros, and F. J. Martos. "A method to determine the fractal dimension of diesel soot agglomerates". In: *Journal of Colloid and Interface Science* 303.1 (2006), pp. 149–158.
- Lapuerta, M., J. J. Expósito, and F. J. Martos. "Effect of sintering on the fractal prefactor of agglomerates". In: *Powder Technology* 271 (2015), pp. 141–154.
- Lapuerta, M., F. J. Martos, and G. Martín-González. "Geometrical determination of the lacunarity of agglomerates with integer fractal dimension". In: *Journal of Colloid and Interface Science* 346.1 (2010), pp. 23–31.
- Lee, K. T., A. Ingram, and N. A. Rowson. "Comparison of granule properties produced using twin screw extruder and high shear mixer: A step towards understanding the mechanism of twin screw wet granulation". In: *Powder Technology* 238 (2013), pp. 91–98.
- Mandelbrot, B. B. *The Fractal Geometry of Nature*. New York: WH Freeman and Co., 1983.

- Marabi, A. and I. S. Saguy. "Effect of porosity on rehydration of dry food particulates". In: *Journal of the Science of Food and Agriculture* 84.10 (2004), pp. 1105–1110.
- Melas, A. D., L. Isella, A. G. Konstandopoulos, and Y. Drossinos. "Morphology and mobility of synthetic colloidal aggregates". In: *Journal of Colloid and Interface Science* 417 (2014), pp. 27–36.
- Merkus, H. G. *Particle Size Measurements: Fundamentals, Practice, Quality*. New York: Springer Science & Business Media, 2009.
- Moreno-Atanasio, R. and M. Ghadiri. "Mechanistic analysis and computer simulation of impact breakage of agglomerates: Effect of surface energy". In: *Chemical Engineering Science* 61.8 (2006), pp. 2476–2481.
- Oh, C. and C. M. Sorensen. "The effect of overlap between monomers on the determination of fractal cluster morphology". In: *Journal of Colloid and Interface Science* 193.1 (1997), pp. 17–25.
- Ohser, J. and K. Schladitz. *3D Images of Materials Structures: Processing and Analysis*. Weinheim: Wiley-VCH, 2009.
- Ortega-Rivas, E. "Bulk properties of food particulate materials: An appraisal of their characterisation and relevance in processing". In: *Food and Bioprocess Technology* 2.1 (2009), pp. 28–44.
- Otsu, N. "A threshold selection method from gray-level histograms". In: *IEEE Transactions on Systems, Man, and Cybernetics* 9.1 (1979), pp. 62–66.
- Palzer, S. "Agglomeration of pharmaceutical, detergent, chemical and food powders: Similarities and differences of materials and processes". In: *Powder Technology* 206.1-2 (2011), pp. 2–17.
- Palzer, S. "Chapter 13 Agglomeration of dehydrated consumer foods". In: *Handbook of Powder Technology* 11 (2007), pp. 591–671.
- Palzer, S. "Influence of material properties on the agglomeration of water-soluble amorphous particles". In: *Powder Technology* 189.2 (2009), pp. 318–326.
- Palzer, S. "The relation between material properties and supra-molecular structure of water-soluble food solids". In: *Trends in Food Science and Technology* 21.1 (2010), pp. 12–25.
- Parikh, D. M. *Handbook of Pharmaceutical Granulation Technology*. Boca Raton: Taylor & Francis Group, 2005.
- Pashminehazar, R., A. Kharaghani, and E. Tsotsas. "Three dimensional characterization of morphology and internal structure of soft material agglomerates produced in spray fluidized bed by X-ray tomography". In: *Powder Technology* 300 (2016), pp. 46–60.

- Pashminehazar, R., S. J. Ahmed, A. Kharaghani, and E. Tsotsas. "Spatial morphology of maltodextrin agglomerates from X-ray microtomographic data: Real structure evaluation vs. spherical primary particle model". In: *Powder Technology* 331 (2018), pp. 204–217.
- Pietsch, W. *Agglomeration Processes: Phenomena, Technologies, Equipment*. Weinheim: Wiley-VCH Verlag GmbH, 2002.
- Rahmanian, N., M. Ghadiri, X. Jia, and F. Stepanek. "Characterisation of granule structure and strength made in a high shear granulator". In: *Powder Technology* 192.2 (2009), pp. 184–194.
- Rajniak, P., C. Mancinelli, R. T. Chern, F. Stepanek, L. Farber, and B. T. Hill. "Experimental study of wet granulation in fluidized bed: Impact of the binder properties on the granule morphology". In: *International Journal of Pharmaceutics* 334.1-2 (2007), pp. 92–102.
- Ratti, C. *Advances in Food Dehydration*. Boca Raton: Taylor & Francis Group, 2009.
- Rieck, C., M. Schmidt, A. Bück, and E. Tsotsas. "Monte Carlo modeling of binder-less spray agglomeration in fluidized beds". In: *AIChE Journal* 64 (2018), pp. 3582–3594.
- Rumpf, H. *Particle Technology*. London: Chapman and Hall, 1990.
- Schörner, K. "Development of methods for scatter artifact correction in industrial X-ray cone-beam computed tomography". PhD thesis. Technical University of Munich, 2012.
- Schubert, H. "Instantization of powdered food products". In: *International Chemical Engineering* 33 (1993), pp. 28–45.
- Shin, W. G., J. Wang, M. Mertler, B. Sachweh, H. Fissan, and D. Y. H. Pui. "Structural properties of silver nanoparticle agglomerates based on transmission electron microscopy: Relationship to particle mobility analysis". In: *Journal of Nanoparticle Research* 11.1 (2009), pp. 163–173.
- Sommerfeld, M. and S. Stübing. "A novel Lagrangian agglomerate structure model". In: *Powder Technology* 319 (2017), pp. 34–52.
- Tahmasebi, P. and M. Sahimi. "Reconstruction of nonstationary disordered materials and media: Watershed transform and cross-correlation function". In: *Physical Review E* 91.3 (2015), pp. 1–11.
- Taylor, M. A., E. J. Garboczi, S. T. Erdogan, and D. W. Fowler. "Some properties of irregular 3-D particles". In: *Powder Technology* 162.1 (2006), pp. 1–15.
- Teraoka, I. *Polymer Solution: An Introduction to Physical Properties*. New York: John Wiley & Sons, Inc., 2002.

- Terrazas-Velarde, K., M. Peglow, and E. Tsotsas. "Investigation of the kinetics of fluidized bed spray agglomeration based on stochastic methods". In: *AIChE J* 57 (2011), pp. 3012–3026.
- Terrazas-Velarde, K., M. Peglow, and E. Tsotsas. "Kinetics of fluidized bed spray agglomeration for compact and porous particles". In: *Chemical Engineering Science* 66 (2011), pp. 1866–1878.
- Terrazas-Velarde, K., M. Peglow, and E. Tsotsas. "Stochastic simulation of agglomerate formation in fluidized bed spray drying: A micro-scale approach". In: *Chemical Engineering Science* 64 (2009), pp. 2631–2643.
- Tsotsas, E. "Heat and mass transfer in packed beds with fluid flow". In: *VDI Heat Atlas*. 10th ed. Berlin/Heidelberg: Springer, 2010, pp. 1327–1341.
- Tsotsas, E. and A. S. Mujumdar. *Modern Drying Technology*. Weinheim: Wiley-VCH, 2011.
- Wang, Y., A. Kharaghani, T. Metzger, and E. Tsotsas. "Pore network drying model for particle aggregates: Assessment by X-ray microtomography". In: *Drying Technology* 30.15 (2012), pp. 1800–1809.
- Weber, A. P., U Baltensperger, H. W. Gaggeler, and A SchmidtOtt. "In situ characterization and structure modification of agglomerated aerosol particles". In: *Journal of Aerosol Science* 27.6 (1996), pp. 915–929.
- Williams, R. A. and M. S. Beck. *Process Tomography: Principles, Techniques and Applications*. Oxford: Butterworth-Heinemann, 1995.
- Wu, M. K. and S. K. Friedlander. "Note on the power law equation for fractal-like aerosol agglomerates". In: *Journal of Colloid and Interface Science* 159.1 (1993), pp. 246–248.
- Yang, R. Y., R. P. Zou, and A. B. Yu. "Computer simulation of the packing of fine particles". In: *Physical Review E* 62.3 B (2000), pp. 3900–3908.
- Yang, R. Y., A. B. Yu, S. K. Choi, M. S. Coates, and H. K. Chan. "Agglomeration of fine particles subjected to centripetal compaction". In: *Powder Technology* 184.1 (2008), pp. 122–129.
- Zeidan, M., X. Jia, and R. A. Williams. "Errors implicit in digital particle characterisation". In: *Chemical Engineering Science* 62.7 (2007), pp. 1905–1914.
- Ziyani, L. and N. Fatah. "Use of experimental designs to optimize fluidized bed granulation of maltodextrin". In: *Advanced Powder Technology* 25.3 (2014), pp. 1069–1075.
- Zou, R. and A. Yu. "Evaluation of the packing characteristics of mono-sized non-spherical particles". In: *Powder Technology* 88.1 (1996), pp. 71–79.

## Appendix A

# Evaluated morphological descriptors

**Table A.1:** Mean coordination number (MCN), standard deviation ( $S_d$ ) and skewness ( $S_k$ ) calculated for spherical primary particle and real structure model (Trial C).

$N_p$	SPPM				RSM			
	$\Sigma CN$	MCN	$S_d$	$S_k$	$\Sigma CN$	MCN	$S_d$	$S_k$
7	12	1.71	0.76	0.46	12	1.71	0.76	0.46
8	10	1.25	1.28	1.25	16	2.00	1.69	1.90
9a	36	4.00	1.73	-0.46	28	3.11	1.27	-0.21
9b	30	3.33	1.41	0.78	30	3.33	1.32	0.73
10	26	2.60	1.51	-0.10	22	2.20	1.14	0.08
11	46	4.18	2.23	0.73	28	2.55	1.29	-0.54
12	44	3.67	1.97	0.11	38	3.17	1.59	0.15
13a	46	3.54	1.27	0.42	34	2.62	0.96	-0.34
13b	44	3.38	1.71	0.00	32	2.46	1.39	0.47
18a	54	3.00	2.25	0.86	56	3.11	1.88	0.77
18b	62	3.44	2.38	0.96	54	3.00	1.57	0.84
19a	64	3.37	1.80	0.37	54	2.84	1.54	0.74
19b	64	3.37	2.01	0.66	56	2.95	1.65	0.54
19c	74	3.89	2.47	1.83	62	3.26	1.66	2.11
19d	68	3.58	2.63	2.48	60	3.16	2.29	3.16
21	68	3.23	1.97	0.18	60	2.86	1.53	0.85
23	82	3.57	2.50	1.10	68	2.96	1.87	1.39
28	92	3.28	2.01	0.66	92	3.29	1.70	0.61
33	122	3.70	2.21	0.41	110	3.33	1.76	0.39
42	154	3.67	2.03	0.76	134	3.19	1.60	0.56
55	226	4.11	2.18	0.74	200	3.64	1.71	0.53
Average value	67.81	3.33	1.92	0.68	59.33	2.89	1.53	0.72

**Table A.2:** Open pore porosities evaluated by radius of gyration and convex hull method for SSPM and RSM (Trial C).

$N_P$	$\sum_{i=1}^{N_P} V_i$ ( $\mu\text{m}^3$ ) * $10^8$	RSM			SSPM		
		$R_g(\mu\text{m})$	$\varepsilon(R_g)$	$\varepsilon(CH)$	$R_g(\mu\text{m})$	$\varepsilon(R_g)$	$\varepsilon(CH)$
7	1.19	468.04	0.87	0.89	432.23	0.84	0.68
8	2.32	514.94	0.81	0.88	422.06	0.66	0.69
9a	2.24	492.41	0.79	0.87	424.96	0.68	0.56
9b	2.84	613.76	0.86	0.87	539.54	0.80	0.61
10	2.13	559.31	0.86	0.84	491.08	0.80	0.62
11	2.65	516.23	0.79	0.81	420.16	0.60	0.63
12	2.57	556.01	0.83	0.87	508.02	0.78	0.66
13a	3.48	724.99	0.90	0.88	698.88	0.89	0.70
13b	2.85	615.45	0.86	0.88	565.64	0.83	0.71
14	2.93	610.99	0.86	0.87	570.41	0.82	0.74
18a	2.26	537.06	0.84	0.83	507.97	0.81	0.72
18b	3.55	678.50	0.87	0.89	623.44	0.84	0.77
19a	3.19	612.53	0.85	0.90	585.43	0.82	0.74
19b	2.49	552.92	0.84	0.88	519.78	0.80	0.76
19c	2.47	540.25	0.83	0.88	517.82	0.80	0.71
19d	4.02	587.50	0.78	0.87	512.68	0.67	0.72
21	3.03	695.54	0.90	0.83	653.27	0.88	0.82
23	5.27	762.69	0.87	0.88	719.67	0.84	0.75
28	5.21	824.47	0.90	0.90	797.45	0.89	0.81
33	6.78	774.89	0.84	0.86	750.61	0.82	0.77
42	7.41	881.95	0.88	0.82	870.74	0.88	0.81
55	10.60	895.81	0.84	0.88	901.73	0.84	0.78
Average value	-	-	0.85	0.87	-	0.80	0.72



**Table A.3:** Result of trial A.

$N_P$	$\Phi_S$	Radius of gyration, $R_g(\mu m)$			Porosity		
		Monodisperse PP	Polydisperse PP	Voxel data	CH	$R_g$	Dilation
9	0.13	559.20	475.76	523.12	0.86	0.88	0.48
10	0.12	431.34	422.13	447.21	0.84	0.76	0.50
12a	0.11	542.89	542.55	619.67	0.89	0.77	0.47
12b	0.10	492.42	391.12	498.03	0.91	0.90	0.54
12c	0.10	550.10	538.73	589.75	0.87	0.90	0.49
13a	0.11	556.54	512.38	555.47	0.87	0.82	0.47
13b	0.10	542.99	520.51	550.90	0.87	0.89	0.44
14a	0.15	649.59	597.56	573.12	0.85	0.78	0.50
14b	0.11	705.61	653.09	711.71	0.90	0.91	0.49
14c	0.09	507.46	491.75	526.21	0.88	0.81	0.53
14d	0.10	626.90	691.07	647.06	0.85	0.88	0.48
15a	0.10	690.41	654.86	701.93	0.91	0.87	0.48
15b	0.10	524.61	535.89	562.73	0.89	0.82	0.45
16	0.11	583.26	551.44	591.32	0.80	0.79	0.57
17	0.10	572.65	572.60	608.40	0.90	0.84	0.43
18	0.09	628.77	583.56	625.94	0.89	0.87	0.59
19a	0.08	698.51	670.45	702.23	0.90	0.77	0.50
19b	0.10	675.22	611.34	664.49	0.84	0.79	0.56
20	0.09	692.59	676.41	707.09	0.89	0.90	0.57
24a	0.08	727.82	713.20	760.91	0.89	0.85	0.48
24b	0.08	663.48	649.38	682.58	0.83	0.87	0.53
27a	0.07	721.46	651.77	681.36	0.86	0.85	0.49
27b	0.08	756.38	753.99	779.51	0.88	0.85	0.46
29	0.07	768.89	775.19	815.03	0.91	0.88	0.50
43	0.06	825.01	860.19	831.12	0.89	0.86	0.49

**Table A.4:** Result of trial B.

$N_P$	$\Phi_S$	Radius of gyration, $R_g(\mu m)$			Porosity		
		Monodisperse PP	Polydisperse PP	Voxel data	CH	$R_g$	Dilation
3a	0.22	246.10	253.49	322.36	0.83	0.75	0.47
3b	0.28	404.09	331.64	389.19	0.82	0.78	0.43
4a	0.21	394.24	351.02	420.20	0.80	0.77	0.43
4b	0.21	334.99	326.55	394.95	0.79	0.71	0.44
4c	0.20	452.47	420.74	486.86	0.79	0.76	0.44
5a	0.20	353.40	308.39	368.07	0.79	0.66	0.44
5b	0.21	265.76	246.60	332.14	0.78	0.75	0.45
5c	0.18	300.19	296.52	355.46	0.79	0.77	0.42
6a	0.20	301.74	324.12	370.19	0.80	0.73	0.45
6b	0.16	425.73	347.29	419.92	0.82	0.68	0.45
6c	0.19	493.99	427.09	542.57	0.84	0.73	0.41
7a	0.16	361.39	351.77	379.07	0.82	0.70	0.46
7b	0.15	390.96	377.79	403.05	0.82	0.79	0.40
8a	0.16	489.29	487.29	519.89	0.86	0.84	0.44
8b	0.17	415.54	393.73	418.23	0.82	0.84	0.48
9a	0.14	454.74	418.12	474.01	0.81	0.66	0.42
9b	0.16	461.31	437.36	506.89	0.84	0.72	0.39
9c	0.15	440.97	412.35	458.03	0.83		
10a	0.13	450.64	437.17	503.58	0.82	0.79	0.40
10b	0.14	518.78	535.13	570.56	0.85	0.83	0.42
13a	0.14	448.16	411.31	383.50	0.82	0.69	0.44
13b	0.11	472.40	442.90	519.66	0.82	0.70	0.46
19	0.11	571.20	543.21	572.52	0.80	0.80	0.44

**Table A.5:** Result of trial C.

$N_P$	$\Phi_S$	Radius of gyration, $R_g(\mu m)$			Porosity		
		Monodisperse PP	Polydisperse PP	Voxel data	CH	$R_g$	Dilation
7	0.17	441.00	432.23	468.04	0.88	0.85	0.54
8	0.13	602.00	422.06	514.94	0.88	0.88	0.59
9a	0.12	442.00	424.96	492.41	0.86	0.71	0.47
9b	0.11	570.00	539.54	613.76	0.87	0.83	0.47
10	0.13	495.21	491.08	559.31	0.84	0.81	0.53
11	0.10	462.20	420.16	516.23	0.81	0.70	0.57
12	0.10	531.00	508.02	556.01	0.87	0.81	0.50
13a	0.09	738.00	698.88	724.99	0.87	0.90	0.48
13b	0.11	617.00	565.64	615.45	0.87	0.86	0.46
14	0.13	611.87	570.41	610.99	0.87	0.86	0.43
18a	0.09	529.00	507.97	537.06	0.83	0.82	0.60
18b	0.09	615.00	623.44	678.50	0.86	0.83	0.44
19a	0.10	604.00	585.43	612.53	0.90	0.84	0.63
19b	0.08	539.00	519.78	552.92	0.88	0.82	0.55
19c	0.08	514.00	517.82	540.25	0.85	0.80	0.50
19d	0.09	632.30	512.68	587.50	0.89	0.84	0.64
21	0.07	722.00	653.27	695.54	0.83	0.91	0.55
23	0.09	722.00	719.67	762.69	0.87	0.85	0.45
28	0.07	797.00	797.45	824.47	0.89	0.88	0.49
33	0.08	759.39	750.61	774.89	0.86	0.83	0.54
42	0.07	843.00	870.74	881.95	0.82	0.84	0.44
55	0.07	934.00	901.73	895.81	0.88	0.86	0.47

**Table A.6:** Result of trial D.

$N_P$	$\Phi_S$	Radius of gyration, $R_g(\mu m)$			Porosity		
		Monodisperse PP	Polydisperse PP	Voxel data	CH	$R_g$	Dilation
3	0.22	390.85	346.54	415.52	0.85	0.82	0.42
4a	0.21	329.81	311.20	402.27	0.77	0.60	0.40
4b	0.20	288.49	261.50	353.75	0.75	0.47	0.42
4c	0.21	394.28	363.38	421.32	0.82	0.78	0.41
4d	0.19	365.39	397.70	418.83	0.77	0.54	0.38
5a	0.24	255.34	255.30	310.69	0.83	0.67	0.46
5b	0.21	325.38	346.85	433.07	0.78	0.50	0.39
5c	0.22	329.47	339.06	385.27	0.84	0.76	0.44
5d	0.20	396.82	379.78	445.44	0.84	0.71	0.40
6a	0.17	458.62	376.81	446.15	0.85	0.84	0.44
6b	0.19	359.25	303.27	376.17	0.78	0.73	0.43
6c	0.19	488.03	448.09	520.92	0.78	0.78	0.36
7a	0.19	401.80	416.27	445.79	0.81	0.76	0.41
7b	0.16	381.05	370.01	417.03	0.81	0.62	0.41
8a	0.16	429.43	377.98	432.45	0.80	0.70	0.40
8b	0.15	434.85	441.49	502.80	0.86	0.83	0.47
9a	0.17	412.12	391.42	424.05	0.83	0.77	0.43
9b	0.16	453.42	450.53	493.40	0.83	0.72	0.39
10	0.18	445.68	382.45	421.75	0.83	0.82	0.43
12	0.14	483.92	490.87	517.39	0.83	0.78	0.42
13	0.14	372.35	396.79	432.48	0.83	0.74	0.39
14	0.14	617.865	573.325	593.984	0.880	0.881	0.412

Table A.7: Result of trial E.

$N_p$	$\Phi_s$	Radius of gyration, $R_g(\mu m)$			Porosity		
		Monodisperse PP	Polydisperse PP	Voxel data	CH	$R_g$	Dilation
9	0.21	550.57	554.35	586.64	0.81	0.89	0.34
10a	0.16	438.30	439.22	515.63	0.83	0.77	0.40
10b	0.19	435.67	358.81	416.94	0.77	0.85	0.41
10c	0.22	640.19	635.84	661.21	0.77	0.88	0.48
12a	0.20	495.33	482.89	510.38	0.85	0.83	0.35
12b	0.19	601.38	509.08	571.52	0.83	0.89	0.41
12c	0.17	434.21	427.65	483.15	0.82	0.82	0.37
12d	0.22	593.83	552.53	574.48	0.80	0.86	0.48
13	0.18	596.82	469.26	524.07	0.83	0.86	0.37
14	0.23	693.43	699.12	714.30	0.78	0.71	0.32
15a	0.23	566.89	470.65	507.54	0.82	0.76	0.42
15b	0.19	579.81	566.40	605.54	0.79	0.85	0.44
16	0.18	665.97	586.87	620.75	0.76	0.85	0.48
18	0.19	684.35	740.56	774.79	0.80	0.86	0.33
19	0.15	701.30	647.79	671.51	0.81	0.87	0.46
20a	0.24	630.40	593.73	623.35	0.80	0.87	0.33
20b	0.15	654.50	641.48	683.12	0.82	0.85	0.47
21	0.25	711.82	677.37	712.13	0.84	0.89	0.31
23	0.19	936.99	845.83	885.76	0.77	0.93	0.31
24	0.20	707.94	656.27	720.36	0.78	0.82	0.46
27	0.22	694.50	640.32	667.85	0.82	0.83	0.47

**Table A.8:** Result of trial F.

$N_P$	$\Phi_S$	Radius of gyration, $R_g(\mu m)$			Porosity		
		Monodisperse PP	Polydisperse PP	Voxel data	CH	$R_g$	Dilation
5a	0.19	361.62	291.34	384.17	0.80	0.70	0.50
5b	0.20	281.71	279.39	354.61	0.84	0.77	0.42
5c	0.17	399.55	374.23	471.20	0.84	0.73	0.45
5d	0.16	380.99	379.87	415.84	0.83	0.74	0.45
5e	0.21	395.98	383.34	448.25	0.81	0.78	0.42
6q	0.20	376.67	394.00	419.21	0.83	0.81	0.42
6b	0.13	462.89	407.23	455.35	0.88	0.79	0.48
6c	0.19	347.27	319.46	379.89	0.83	0.69	0.44
7a	0.15	424.87	436.24	492.50	0.86	0.77	0.44
7b	0.15	575.28	499.79	563.18	0.89	0.84	0.43
7c	0.14	452.06	389.79	461.30	0.86	0.74	0.46
9a	0.14	604.43	535.95	582.03	0.89	0.87	0.45
9b	0.13	484.62	455.41	502.23	0.88	0.78	0.49
10a	0.11	484.88	468.63	502.46	0.88	0.83	0.49
10b	0.16	553.77	564.04	573.67	0.85	0.88	0.42
11	0.16	722.02	636.01	655.38	0.85	0.91	0.51
15	0.12	684.34	606.35	644.72	0.89	0.85	0.43
16a	0.11	857.14	809.01	855.80	0.88	0.91	0.47
16b	0.11	499.39	505.31	541.46	0.85	0.78	0.46
26	0.08	666.42	678.51	709.76	0.88	0.86	0.46

**Table A.9:** Result of trial G.

$N_P$	$\Phi_S$	Radius of gyration, $R_g(\mu m)$			Porosity		
		Monodisperse PP	Polydisperse PP	Voxel data	CH	$R_g$	Dilation
9	0.17	557.44	523.87	559.52	0.84	0.82	0.45
10	0.12	554.46	478.51	543.43	0.84	0.81	0.39
11	0.13	563.96	447.70	534.22	0.78	0.76	0.40
12a	0.13	611.70	422.70	546.09	0.84	0.79	0.40
12b	0.16	599.67	495.13	550.88	0.80	0.83	0.44
13a	0.12	563.89	541.23	582.60	0.80	0.86	0.40
13b	0.13	533.81	488.06	542.51	0.81	0.75	0.42
13c	0.12	512.21	464.87	514.31	0.84	0.80	0.37
13d	0.13	562.11	581.63	620.83	0.83	0.80	0.47
14a	0.13	537.26	479.02	528.23	0.81	0.80	0.37
14b	0.15	591.80	546.23	602.64	0.85	0.77	0.45
14c	0.17	454.30	515.17	507.77	0.80	0.68	0.48
15a	0.12	581.40	502.45	552.23	0.82	0.79	0.43
15b	0.20	661.40	592.37	654.67	0.77	0.86	0.38
16	0.12	565.19	543.66	581.00	0.86	0.79	0.44
18a	0.22	609.76	628.18	698.49	0.80	0.85	0.42
18b	0.14	508.51	519.76	574.65	0.80	0.76	0.39
19a	0.22	736.55	784.99	747.22	0.78	0.72	0.38
19b	0.18	705.87	669.25	704.47	0.82	0.87	0.47
20	0.15	636.75	601.32	627.24	0.83	0.83	0.46
22a	0.17	644.64	629.38	663.88	0.81	0.82	0.41
22b	0.18	759.41	684.52	723.62	0.84	0.80	0.47
23	0.19	601.56	579.91	616.91	0.79	0.81	0.40
24	0.16	725.19	651.55	667.72	0.83	0.82	0.43
27	0.21	736.27	711.01	720.01	0.78	0.86	0.44





# Scientific contributions

## Journal publications

1. **R. Pashminehazar**, A. Kharaghani, E. Tsotsas, "Influence of process variables on internal structure of soft material agglomerates produced in spray fluidized bed", In preparation.
2. J. Szadzinska, Dominik Mierzwa, A. Pawlowski, **R. Pashminehazar**, A. Kharaghani, E. Tsotsas, "Ultrasound- and microwave-assisted intermittent drying of red beetroot", *Drying Technology*, (2019).  
<https://doi.org/10.1080/07373937.2019.1624565>.
3. J. Szadzinska, J. Lechtanska, **R. Pashminehazar**, A. Kharaghani, E. Tsotsas, "Nonstationary convective drying of raspberries assisted with microwaves and ultrasound", *Drying Technology*, (2019).  
<https://doi.org/10.1080/07373937.2018.1481087>.
4. **R. Pashminehazar**, A. Kharaghani, E. Tsotsas, "Determination of fractal dimension and prefactor of agglomerates with irregular structure", *Powder Technology* 343 (2019) 765 -774.  
<https://doi.org/10.1016/j.powtec.2018.10.046>
5. **R. Pashminehazar**, S.J. Ahmed, A. Kharaghani, E. Tsotsas, "Spatial morphology of maltodextrin agglomerates from X-ray microtomographic data: Real structure evaluation vs. spherical primary particle model", *Powder Technology* 331 (2018) 204 -217.  
<https://doi.org/10.1016/j.powtec.2018.03.008>
6. J. Szadzinska, J. Lechtanska, **R. Pashminehazar**, A. Kharaghani, E. Tsotsas, "Microwave and ultrasound-assisted convective drying of raspberries: Drying kinetics and microstructural changes", *Drying Technology* (2018).  
<https://doi.org/10.1080/07373937.2018.1433199>
7. **R. Pashminehazar**, A. Kharaghani, E. Tsotsas, "Three dimensional characterization of morphology and internal structure of soft material agglomerates produced in spray fluidized bed by X-ray tomography", *Powder Technology* 300 (2016) 46 -60.  
<https://doi.org/10.1080/07373937.2018.1433199>

8. **R. Pashmineh azar**, C. Falamaki, "Removal of aqueous  $Fe^{++}$  using  $MnO_2$ -Clinoptilolite in batch slurry reactor: Catalyst synthesis, characterization and modeling of catalytic behavior", *Journal of Industrial and Engineering Chemistry*.  
<https://doi.org/10.1016/j.jiec.2011.11.112>

## Conference proceedings

1. **R. Pashminehazar**, A. Kharaghani, E.Tsotsas, "Influence of process conditions on the morphology of maltodextrin agglomerates investigated by 3D X-ray images", *International Congress on Particle Technology (PARTEC)*, April 2016, Nurnberg, Germany.
2. **R. Pashminehazar**, A. Kharaghani, E.Tsotsas, "Development of 3D morphological descriptors for agglomerates with complex structures", *6th Conference on Industrial Computed Tomography (iCT)*, February 2016, Wels, Austria.
3. **R. Pashminehazar**, A. Kharaghani, E.Tsotsas, "Micro-structure of maltodextrin agglomerates produced by fluidized bed", *7th International Granulation Workshop*, July 2015, Sheffield, England.

## Conference presentations

1. Spatial Morphology of real structure and simplified model of irregular agglomerates, presented (oral) in GRK workshop, May 2018, Tangermunde, Germany.
2. Comparison of spatial morphology for real structure and spherical model of maltodextrin agglomerates by post processing X-Ray microtomographic images, presented (poster) in 8th International Granulation Workshop, June 2017, Sheffield, England.
3. Spatial morphology of real and model agglomerates determined from X-ray microtomography images, presented (poster) in GRK workshop, May 2017, Leipzig, Germany.
4. Influence of process conditions on the morphology of Maltodextrin agglomerates investigated by 3D X-ray images, presented (oral) in International Congress on Particle Technology (PARTEC), April 2016, Nurnberg, Germany.
5. Determination of the fractal dimension of soft agglomerates produced in spray fluidized bed, presented (poster) in Jahrestreffen der Fachgruppen Agglomerations-und Schautguttechnik, February-March 2019, Bingen, Germany.

6. Development of 3D morphological descriptors for agglomerates with complex structures, presented (oral) in 6th Conference on Industrial Computed Tomography (iCT), February 2016, Wels, Austria
7. Determination of fractal dimension and coordination number of soft agglomerates produced in spray fluidized bed, presented (poster) in GRK workshop, November 2015, Brandenburg, Germany.
8. Microstructural details of maltodextrin agglomerates produced by fluidized bed agglomeration, presented (oral) in 10th European Congress of Chemical Engineering, September-October 2015, Nice, France.
9. Micro-structure of maltodextrin agglomerates produced by fluidized bed, presented (oral) in 7th International Granulation Workshop, July 2015, Sheffield, England.
10. Development of 3D morphological descriptors for agglomerate with complex structure, presented (oral) in GRK summer school, June 2015, Berlin, Germany.
11. Production and microstructural characterization of maltodextrin agglomerates, presented (poster) in Jahrestreffen der Fachgruppen Agglomerations-und Schuttgut-technik, March 2015, Magdeburg, Germany.
12. Microstructure characterization of maltodextrin agglomerates by X-ray microtomography, presented (oral) in GRK workshop, November 2014, Quedlinburg, Germany.
13. Selection of operational parameters for agglomeration and granulation of maltodextrin by fluidized bed, presented (oral) in GRK workshop, May 2014, Dessau, Germany.
14. Micro-structure of particles produced by fluidized bed agglomeration of soft materials, presented (poster) in GRK workshop, January 2014, Magdeburg, Germany.
15. Micro-structure of particles produced by fluidized bed agglomeration of soft materials, presented (oral) in GRK workshop, November 2013, Wernigerode, Germany.

## Curriculum Vitae

Name **Reihaneh Pashminehazar**

Date of birth 6 August 1986

Place of birth Tabriz/Iran

E-Mail r.pashmineh@gmail.com

### Education

---

09/2013-12/2018 PhD in Thermal Process Engineering,  
Otto von Guericke University, Magdeburg, Germany

03/2016-05/2017 Parental leave

09/2008-09/2010 M.Sc. in Chemical Engineering,  
Amirkabir University of Technology, Tehran, Iran

09/2004-09/2008 B.Sc. in Chemical Engineering,  
Amirkabir University of Technology, Tehran, Iran

### Work experience

---

2013-2017 Scientific Assistant,  
Otto von Guericke University, Magdeburg, Germany

2010-2013 Process Engineer,  
Persia Petro Gas (PPG), Petroleum Equipment Supplier, Tehran, Iran